國立臺灣大學電機資訊學院光電工程學研究所

碩士論文

Graduate Institute of Photonics and Optoelectronics

College of Electrical Engineering and Computer Science

National Taiwan University

Master's Thesis

以吖啶咔唑衍生物製作藍色熱活化延遲螢光放光有機發光二極體之研究

Researches on Blue Thermally Activated Delayed Fluorescence Organic Light-emitting Diodes with Acidan-Carbazole Derivatives

邱景皇

Chin-Huang Chiu

指導教授：李君浩 博士

Advisor: Jiun-Haw Lee, Ph.D.

中華民國 114 年 7 月

(July) 2025

doi:10.6342/NTU202503850

致謝

感謝我的指導教授李君浩教授這兩年來對我的指導與訓練，在除了課業上的事情以外老師也提供了我許多的幫助，在我的碩士生涯的路上，走得非常的順遂。感謝邱天隆教授，老師總會提供求學時的經驗，讓我也可以站在巨人的肩膀上，給了我很多的鼓勵與實驗上的建議。感謝我的父母無條件的支持我，在疲累時，也可以專心上學業上。

另外要特別感謝林伯彥博士和陳佳勳博士，謝謝林伯彥博士，如果沒有林伯彥博士在實驗上的指導，與研討會上 oral 的準備，好幾個晚上陪我修改與練習，給了我很好的經驗。謝謝陳佳勳博士，在碩一還非常菜鳥的我，特別幫我們補習，與機台遇上問題時，不管是什麼時間都熱心的幫助，在實驗生涯排除了很多的阻礙。謝謝林虹儀學姊、李哲宇學長、林坤榮學長以及各位學弟妹，因為有你們，在休息時都充滿歡笑聲，做實驗的日子不孤單。

doi:10.6342/NTU202503850

摘要

本篇論文中包含三個主題。第一個主題，我們介紹由化學所梁文傑教授團隊所合成的吖啶-咔唑-嘧啶的衍生物為天藍色熱活化延遲螢光（thermally activated delayed fluorescence, TADF）發光體的有機二極體。其中，以 10-(3,5-di(9H-carbazol-9-yl)-4-(pyrimidin-2-yl)phenyl)-9,9-dimethyl-9,10-dihydroacridine (4Ac35CzPy), 10-(2,5-di(9H-carbazol-9-yl)-4-(pyrimidin-2-yl)phenyl)-9,9-dimethyl-9,10-dihydroacridine (4Ac25CzPy) 作為發光體，摻雜於 9,9'-(2-(1-Phenyl-1H-benzo[d]imidazol-2-yl)-1,3-phenylene)bis(9H-carbazole) (*o*-2CbzBz) 形成發光層的有機二極體中，達到了最大電流效率為 50.4 cd/A;最大功率效率為 45.3 lm/W;以及最大外部量子效率（external quantum efficiency, EQE）為 21.2%的元件表現。

第二個主題，我們介紹由化學所梁文傑教授團隊所合成的以吖啶-咔唑的衍生物為發光層主體材料的有機二極體。其中，以透過在 10-(3,5-di(9H-carbazol-9-yl)-4-(1-phenyl-1H-benzo[d]imidazol-2-yl)phenyl)-9,9-dimethyl-9,10-dihydroacridine (4Ac26CzBz)摻雜天藍色的熱活化延遲螢光客體材料 2,3,5,6-tetrakis(3,6-di-*tert*-butyl-9*H*-carbazol-9-yl)benzonitrile (4TCzBN)，有機發光二極體達到最大電流效率為 59.84 cd/A，最大功率效率為 62.84 lm/W，最大外部量子效率為 35.78%，是目前我們已知此材料所有的以 4TCzBN 為客體材料有機發光二極體中最高紀錄。

doi:10.6342/NTU202503850

Abstract

There are three topics in this thesis. In the first part, acridine-carbazole-imidazole derivatives, 10-(3,5-di(9H-carbazol-9-yl)-4-(pyrimidin-2-yl)phenyl)-9,9-dimethyl-9,10-dihydroacridine (4Ac35CzPy) and 10-(2,5-di(9H-carbazol-9-yl)-4-(pyrimidin-2-yl)phenyl)-9,9-dimethyl-9,10-dihydroacridine (4Ac25CzPy), provided by Prof. Man-Kit Leung's group, Department of Chemistry in National Taiwan University, were used as blue thermally activated delayed fluorescence (TADF) dopants in the 9,9'-(2-(1-Phenyl-1H-benzo[d]imidazol-2-yl)-1,3-phenylene)bis(9H-carbazole) (*o*-2CbzBz) host as the emitting layer (EML) of the organic light-emitting diodes (OLEDs), which reached the maximum current efficiency, power efficiency, and external quantum efficiency (EQE) of 50.4 cd/A, 45.3 lm/W, and 19.7%, respectively.

In the second part of this thesis, 10-(3,5-di(9H-carbazol-9-yl)-4-(1-phenyl-1H-benzo[d]imidazol-2-yl) phenyl)-9,9-dimethyl-9,10-dihydroacridine (4Ac26CzBz), provided by Prof. Man-Kit Leung's group, Department of Chemistry in National Taiwan University, was utilized as host material doped with the sky-blue thermally activated delayed fluorescence (TADF) dopant, 2,3,5,6-tetrakis(3,6-di-*tert*-butyl-9*H*-carbazol-9-yl) benzonitrile (4TCzBN) as the EML of the OLED. By adjusting the device structure, maximum current efficiency, power efficiency, and EQE of 59.84 cd/A, 62.83 lm/W, and 35.78% were achieved, respectively, which are the highest efficiencies among all the 4TCzBN-based OLEDs, to our best knowledge.

doi:10.6342/NTU202503850

材料簡寫

doi:10.6342/NTU202503850

Molecular structures

(a)

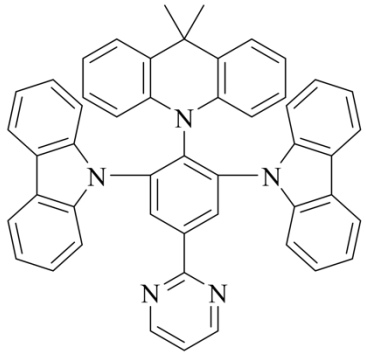

(b)

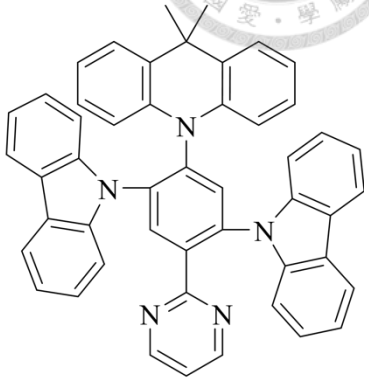

(c)

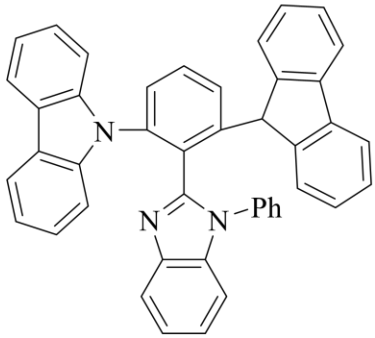

(d)

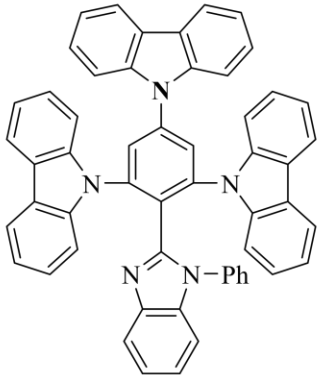

(e)

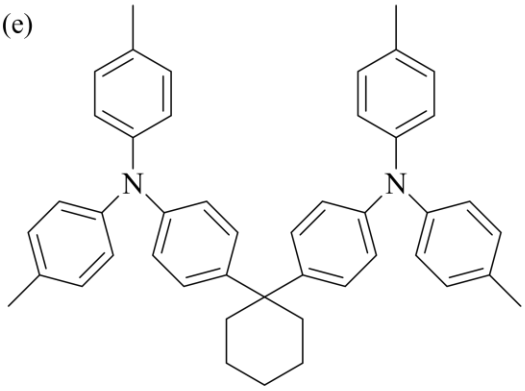

(f)

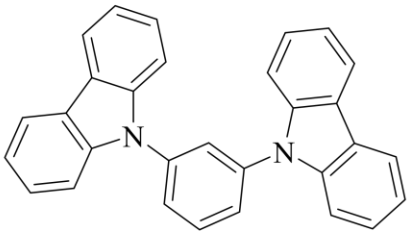

(g)

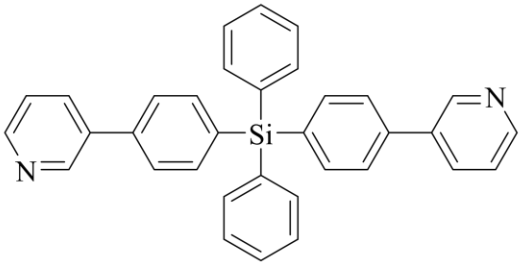

doi:10.6342/NTU202503850

(h)

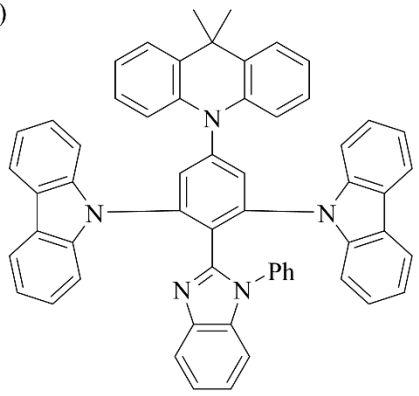

(i)

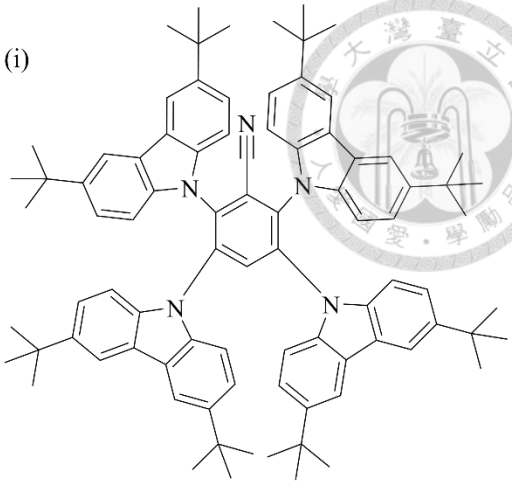

(j)

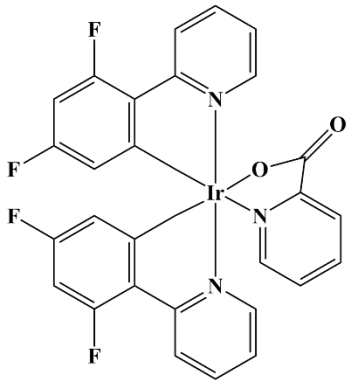

doi:10.6342/NTU202503850

Content

doi:10.6342/NTU202503850

doi:10.6342/NTU202503850

Figure content

doi:10.6342/NTU202503850

doi:10.6342/NTU202303850

doi:10.6342/NTU202503850

Table content

doi:10.6342/NTU202503850

doi:10.6342/NTU202503850

Chapter 1 Introduction

1.1 Overview

This thesis focuses on two main themes. First, we demonstrated sky-blue fluorescent organic light-emitting diodes (OLEDs) based on two thermally activated delayed fluorescence (TADF) emitter synthesized by Professor Man-kit Leung's research group at the Department of Chemistry, National Taiwan University. One of the carbazole-pyrimidine derivatives achieved a maximum external quantum efficiency (EQE) of 21.2%. Second, we introduced a novel acridine and carbazole moieties linked to a benzimidazole core as the host of blue TADF-OLED, which was also synthesized by Professor Man-kit Leung's research group. EQE of 35.8% was achieved in this device.

1.2 Introduction of TADF OLED

In a TADF material, the up conversion of triplet excitons to singlet excitons, or called reverse intersystem crossing (RISC) process, is possible through thermal energy, which can theoretically realize an internal quantum efficiency (IQE) of 100% [1–4]. In recent years, the efficiencies of TADF devices have improved significantly, with the EQE of green devices exceeding 30%, and those of blue and red devices approaching 41% and 20%, respectively [5–7]. TADF molecules usually comprise strong donors and acceptors, which are orthogonally connected through an aromatic ring [8]. This

doi:10.6342/NTU202503850

design enables the materials to possess a small singlet–triplet energy splitting (ΔE_{ST}), which facilitates RISC and enhances OLED efficiency [9,10].

1.3 Review of comprising acridan-pyrimidine TADF OLED

Acridine is an important electron donor moiety in designing TADF materials [11,12]. For instance, 9,9-dimethyl-9,10-dihydroacridine exhibits moderate electron-donating ability and a high triplet energy, making it a suitable candidate for TADF applications. On the other hand, pyrimidine is an effective electron acceptor that has demonstrated excellent performance in TADF systems. Emitters substituted at the 2, 4, 5, and 6 positions of pyrimidine have been explored [13,14]. Yasuda reported a series of D–A type pyrimidine-based TADF materials with electron donors connected at the 2-position, among which 9,9-dimethylacridan,2-phenyl pyrimidine (Ac-PM) was the bluest emitter in the series, showing a maximum EQE of 11.4% [15]. The introduction of bulky phenyl substituents and rigid spiro structures to enhance steric shielding increased the EQE of Ac-46DPPM to 15.5%, while that of spiro[2,7-dimethylacridan 9,90-fluorene] 2-phenyl pyrimidine (MFAc-PPM) increased to 20.4%, with their spectral peak of electroluminescence (EL) emission slightly red-shifted to 464 nm and 470 nm, respectively [16]. On the other hand, when an electron-withdrawing cyan group was introduced at the 5-position of the pyrimidine ring (Pm5), the EQE increased to 30.6%; however, its spectral peak significantly red-shifted to 541 nm [17]. Hence, maintaining blue emission while enhancing EQE remains a challenging research topic.

1.4 Review of comprising carbazole-based TADF OLED

In 2021, K. H. Choi et al. reported three carbazole-dibenzofuran derivatives, 2,8-

doi:10.6342/NTU202503850

di(9H-carbazol-9-yl)dibenzo[b,d]furan (28CzDBF), 9,9′-(dibenzo[b,d]furan-2,6-diyl)bis(9H-carbazole) (26CzDBF) and 4,6-di(9H-carbazol-9-yl)dibenzo[b,d]furan (46CzDBF), as host materials with high triplet energies, which all showed triplet energies above 2.95 eV. The molecular structures of these three materials are shown in the Fig. 1-1 [18], which also presents the HOMO and LUMO distributions of 26CzDBF, 46CzDBF, and 28CzDBF. The HOMO and LUMO distribution results were similar for these three compounds: the HOMO was mainly located on the carbazole units and partially extended onto the dibenzofuran core, which showed carbazole unit was an effective electron donor unit.

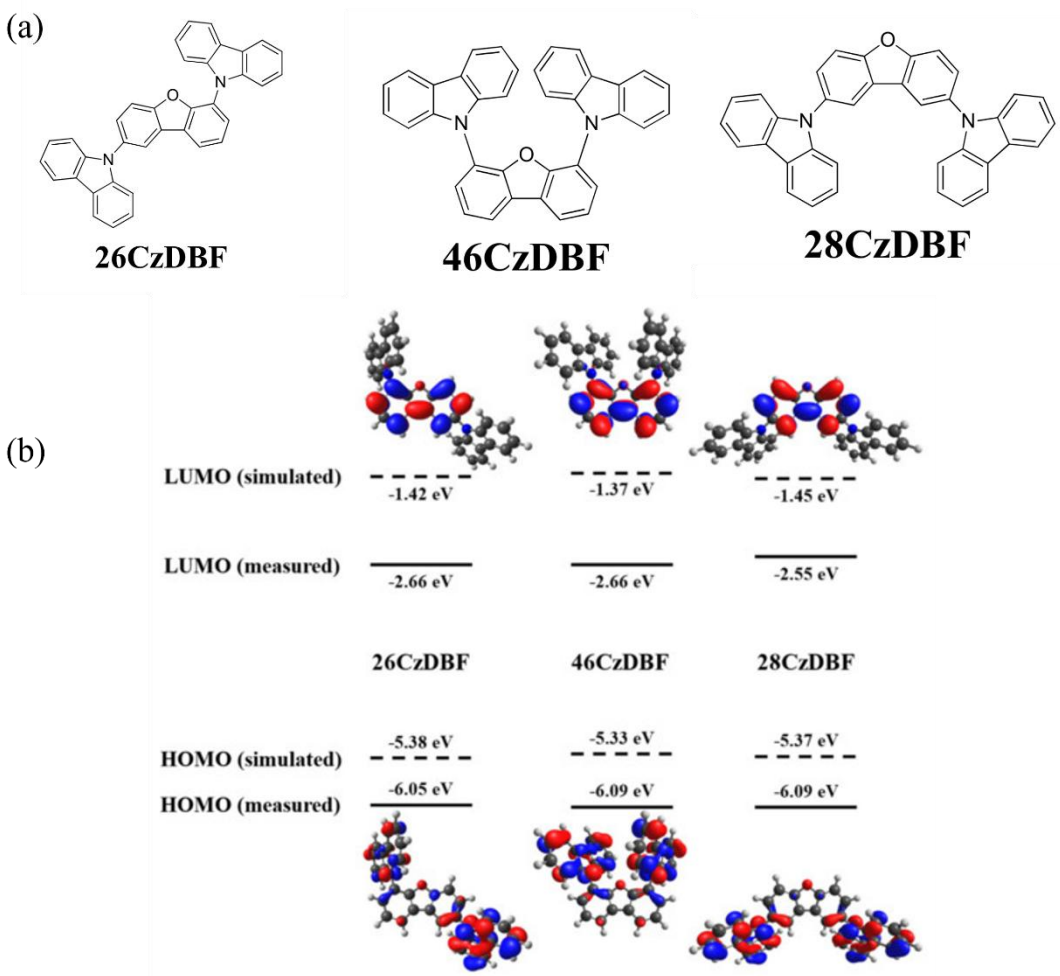

Fig. 1-1 (a) Molecular structures of 26CzDBF, 46CzDBF and 28CzDBF, (b) HOMO and LUMO calculated and experimental results of 26CzDBF, 46CzDBF, and 28CzDBF [18].

doi:10.6342/NTU202503850

1.5 Review of blue TADF OLED with 4TCzBN as dopant

In this section, we focus on reviewing blue TADF OLEDs employing 2,3,5,6-tetrakis(3,6-di-tert-butyl-9H-carbazol-9-yl)benzonitrile (4TCzBN) as the dopant in different host materials [19-27]. Table 1-1 summarizes the efficiency performances of green TADF OLEDs using 4TCzBN as the dopant material in recent years. To the best of our knowledge, the highest EQE record for blue TADF OLEDs based on 4TCzBN was achieved using TBA-BCz-BN as the emitter, 4TCzBN as the TADF sensitizer, and mCBP as the host, which was 30.8%. Fig. 1-2 (a) and (b) show the molecular structures of mCBP and TBA-BCz-BN, as well as the device energy diagram. TBA-BCz-BN exhibited an emission peak at 468 nm with a narrow FWHM of 22 nm.

Table 1-1 Review of blue TADF OLEDs with different host doped with 4TCzBN.

Dopant	Host	Concentration	EQE / P.E. (lm/W)	V_{on}	References
4TCzBN	mCBP	40 wt%	16.2%/ 24.4	3.30	19
	2,4-2CzBN	10%	21.5%/42.0	2.8	20
	mCPBC	--	13.7%/29.2	2.9	21
	PH204	40wt%	22%/--	5.4	22
	DACT-II	20%	2.1%/4.7	3.9	23
	P4CzCN-PA	40wt%	13.4%/13.7	5.3	24
	25tcc	30%	22.8%/28.2	--	25
	mCBP	25wt%	30.8%/31.3	3.3	26
	3phCN-ICz	20 wt%	22.04%/--	3.5	27

C.E.: current efficiency. P.E.: power efficiency

doi:10.6342/NTU202503850

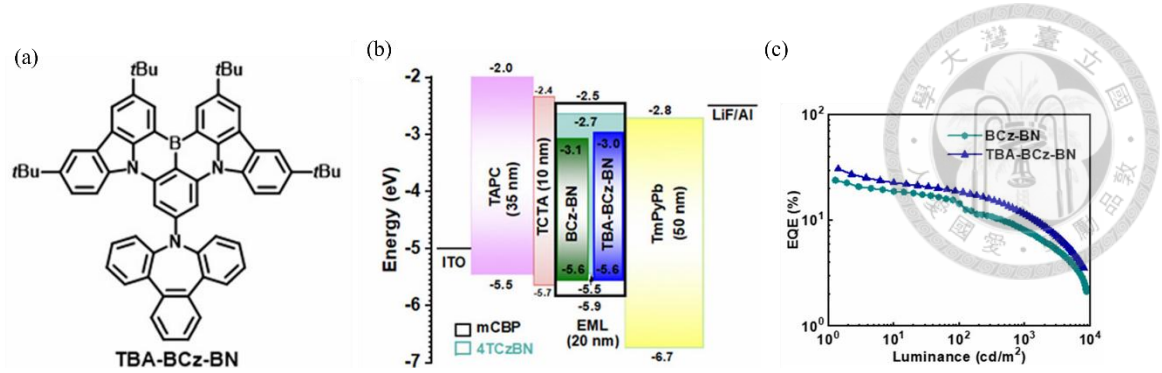

Fig. 1-2 (a) Molecular structure of TBA-BCz-BN, (b) device energy diagram, and (c) EQE versus luminance curve of optimized blue TADF OLED with TBA-BCz-BN as dopant [26].

1.6 Motivation

In chapter 3, two novel TADF emitters, namely 4Ac25CzPy and 4Ac35CzPy, were successfully synthesized by Professor Man-kit Leung's research group. Device optimization was performed which achieved maximum EQEs of 12.4% and 21.2%. In chapter 4, ambipolar host materials, namely 4Ac26CzBz, were designed and synthesized by Prof. Man-Kit Leung's group. With introduction of blue TADF dopant, 4TCzBN, maximum EQEs of 35.8% was achieved.

1.7 References

[1] H. Uoyama, K. Goushi, K. Shizu, H. Nomura, C. Adachi, Highly efficient organic light-emitting diodes from delayed fluorescence, *Nature* 492 (7428) (2012) 234238.

[2] Y. Im, M. Kim, Y. J. Cho, J.-A. Seo, K. S. Yook, J. Y. Lee, Molecular design strategy of organic thermally activated delayed fluorescence emitters, *Chem. Mater.* 29 (5) (2017) 19461963.

[3] Q. Zhang, J. Li, K. Shizu, S. Huang, S. Hirata, H. Miyazaki, C. Adachi, Design of efficient thermally activated delayed fluorescence materials for pure blue organic light emitting diodes, *J. Am. Chem. Soc.* 134 (36) (2012) 1470614709.

doi:10.6342/NTU202503850

[4] Z. Yang, Z. Mao, Z. Xie, Y. Zhang, S. Liu, J. Zhao, J. Xu, Z. Chi, M. P. Aldred, Recent advances in organic thermally activated delayed fluorescence materials, *Chem. Soc. Rev.* 46 (3) (2017) 9151016.

[5] D. Barman, Y. Tsuchiya, C. Adachi, Efficient TADF emission via novel acceptor engineering, *Nat. Commun.* 16 (2025) 5023.

[6] J. Wang, C. Jiang, C. Cao, X. Zhuang, B. Liang, Y. Wang, H. Bi, High-efficiency OLEDs using novel TADF hosts, *Org. Electron.* 141 (2025) 107238.

[7] N. Y. Kwon, C. W. Koh, S. H. Park, H. Kwak, H. Y. Kim, C. Y. Park, N. Peethani, J. Y. Park, S. Kim, K. Jin, C. S. Hong, M. J. Cho, S. Park, D. H. Choi, High-performance TADF materials with rigid cores, *Chem. Eng. J.* 506 (2025) 160139.

[8] M. Mamada, S. Yada, M. Hayakawa, R. Uchida, H. Katagiri, T. Hatakeyama, C. Adachi, π-conjugated blue TADF materials, *Commun. Chem.* 7 (2024) 212.

[9] Q. Zhang, B. Li, S. Huang, H. Nomura, H. Tanaka, C. Adachi, Efficient blue thermally activated delayed fluorescence emitters, *Nat. Photon.* 8 (4) (2014) 326332.

[10] S. Hirata, Y. Sakai, K. Masui, H. Tanaka, S. Y. Lee, H. Nomura, N. Nakamura, M. Yasumatsu, H. Nakanotani, Q. Zhang, K. Shizu, H. Miyazaki, C. Adachi, Highly efficient blue electroluminescence based on TADF, *Nat. Mater.* 14 (3) (2015) 330336.

[11] Q. Zhang, S. Sun, W. Liu, P. Leng, X. Lv, Y. Wang, H. Chen, S. Ye, S. Zhuang, L. Wang, Design of efficient deep-blue TADF materials, *J. Mater. Chem. C* 7 (31) (2019) 94879495.

[12] L. Yu, Z. Wu, G. Xie, W. Zeng, D. Ma, C. Yang, High-efficiency TADF emitters with large horizontal orientation, *Chem. Sci.* 9 (2018) 13851391.

[13] X. Liu, Y. Li, J. Li, X. Liu, Y. Zhang, L. Zhang, B. Chen, Multi-donor-acceptor TADF materials, *J. Mater. Chem. C* 7 (2019) 1266612673.

[14] T. Serevičius, R. Skaisgiris, I. Fiodorova, V. Steckis, J. Dodonova, D. Banevičius, K. Kazlauskas, S. Juršėnas, S. Tumkevičius, Exciplex-type TADF emitters, *Org. Electron.* 82 (2020) 105723.

[15] Y. Liu, X. Zhang, L. Yu, Z. Wu, G. Xie, W. Zeng, D. Ma, C. Yang, Pure TADF emission without phosphorescence, *Chem. Sci.* 8 (2017) 26582664.

doi:10.6342/NTU202503850

[16] K. Nakao, H. Sasabe, R. Komatsu, Y. Hayasaka, T. Ohsawa, J. Kido, Highly efficient green OLEDs with TADF emitters, *Adv. Opt. Mater.* 5 (6) (2017) 1600843.

[17] Pan, K.C., Li, S.W., Ho, Y.Y., Shiu, Y.J., Tsai, W.L., Jiao, M., Lee, M.T., Efficient and tunable thermally activated delayed fluorescence emitters having orientation-adjustable CN-substituted pyridine and pyrimidine acceptor units, *Adv. Funct. Mater.* 26 (42) (2016) 7560–7571.

[18] J. Liu, Y. Liu, X. Zhang, L. Yu, Z. Wu, G. Xie, W. Zeng, D. Ma, C. Yang, Rigid donor–acceptor molecular systems for efficient OLEDs, *Molecules* 26 (10) (2021) 2804.

[19] G. Meng, D. Zhang, J. Wei, Y. Zhang, T. Huang, Z. Liu, C. Yin, X. Hong, X. Wang, X. Zeng, D. Yang, D. Ma, G. Li, L. Duan, Aggregation-enhanced TADF OLEDs, *Chem. Sci.* 13 (2022) 56225630.

[20] X. Xiao, B. Lei, D. Wu, Z. Bin, Synergetic effect of dual TADF cores, *Chem. Commun.* 59 (2023) 65566559.

[21] J. Zhang, Y. Li, X. Liu, H. Wang, Z. Liu, D. Ma, C. Yang, Dual-emission TADF materials, *J. Mater. Chem. C* 10 (2022) 26662673.

[22] X. Wang, Y. Li, Z. Zhang, High PLQY and oriented TADF emitters, *ACS Appl. Mater. Interfaces* 11 (2019) 66636663.

[23] D. Zhang, M. Cai, Z. Bin, Y. Zhang, D. Zhang, L. Duan, Hybridized local and charge transfer state TADF, *Chem. Sci.* 7 (2016) 33553363.

[24] D. Zhang, M. Cai, Y. Zhang, D. Zhang, L. Duan, Rigid molecular design for high EQE, *Mater. Horiz.* 3 (2016) 145151.

[25] P. Wei, D. Zhang, L. Duan, TADF emitters with high color purity, *Adv. Funct. Mater.* 30 (2020) 1907083.

[26] W. Jiang, G. Zhang, G. Zhao, X. Wang, W. Tian, Y. Sun, Donor–acceptor interface tuning for TADF, *Dyes Pigm.* 210 (2023) 111037.

[27] Chen, C.H., Lin, K.R., Lin, C.F., Starykov, H., Bucinskas, A., Gudeika, D., Bezvikonnyi, O., Simokaitiene, J., Volyniuk, D., Grazulevicius, J.V., Lee, J.H., Chiu, T.L., Sensitivity of the hidden TADF to the linking topology of di-tert-butyl-carbazolyl and benzonitrile moieties in the molecules of emitters or hosts intended for efficient blue OLEDs, *J. Photochem. Photobiol. A* 440 (2023) 114686.
doi:10.6342/NTU202503850

Chapter 2 Experiment

This chapter describes the fabrication process and measurement methods of organic light-emitting diodes (OLEDs) and organic thin films. OLED measurements include current density-luminance-voltage (J-L-V) characteristics, external quantum efficiency (EQE), operating lifetime, transient electroluminescence (TrEL), time-resolved photoluminescence (TrPL), photoluminescence quantum yield (PLQY), absorption and PL spectroscopy, and photoelectron spectroscopy.

2.1 OLED fabrication process

We used a patterned indium tin oxide (ITO) glass substrate through photolithography process. Next, it was subjected to ultrasonic cleaning in acetone (ACE)

doi:10.6342/NTU202503850

and isopropanol (IPA) for ten minutes each. To lower the energy barrier between the ITO and the hole injection layer (HIL), we treated the ITO substrate with O_2 plasma in a vacuum chamber at a pressure of 30 mtorr for five minutes to enhance its work function. Following the O_2 plasma treatment, the ITO substrate was placed into an evaporation chamber where the organic layers and aluminum cathode were thermally deposited sequentially at pressures below 8×10^{-6} and 5×10^{-5} torr, respectively. We used another glass substrate for the encapsulation process which was carried out in a glove box with water and oxygen levels below 0.5 ppm. Figure 2-1 shows a schematic diagram of the resulting OLED device, which has a pixel size of 0.04 cm2.

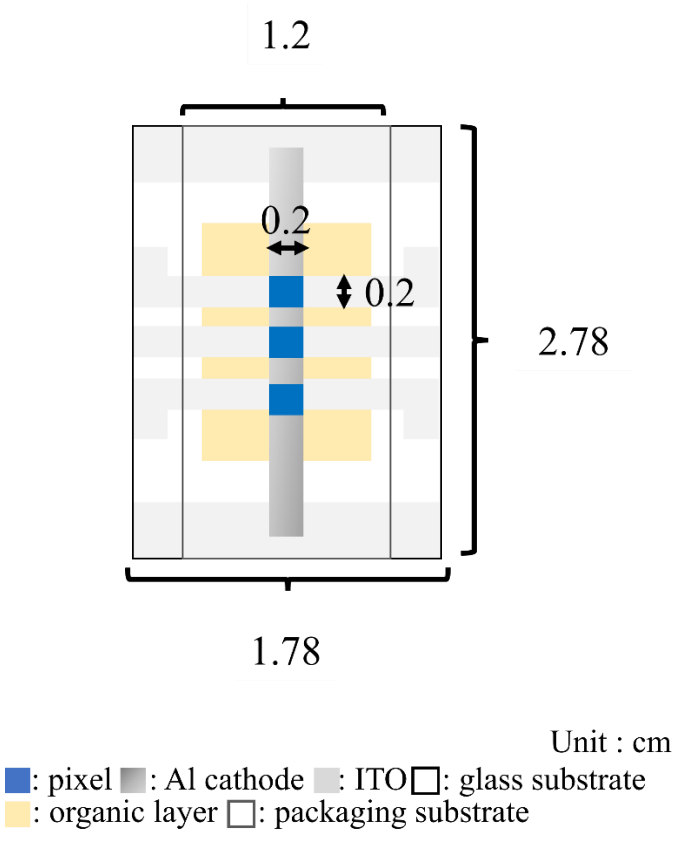

Fig. 2-1 Schematic diagram of OLED. (Unit: cm)

2.2 Measurement systems

2.2.1 J-V-L, EQE, and operation lifetime measurements

We used a Keithley source meter to supply voltages to the OLED and obtain the corresponding current densities. At the same time, the luminance and spectrum of the

doi:10.6342/NTU202303850

electroluminescence (EL) from the OLED were measured with a spectroradiometer, Minolta CS-1000. These results can be further used to calculate the current efficiency (cd/A) and power efficiency (lm/W). All instruments were connected to a computer-controlled by the Labview program.For EQE measurements, a constant current was supplied to the OLED via a Keithley 2400. The OLED was placed on a rotation holder, and the luminance and spectrum of the OLED were measured at different angles every 10° from 0° to 80° using the Minolta CS-1000. By integrating all the photons emitted from the OLED over the supplied electron-hole pairs to the device, EQE can be calculated. [1] Operation lifetime can be obtained by providing a constant current density and measuring the luminance and voltage over time with the Keithley 2400 and Minolta CS-1000. A schematic diagram of the system setup is shown in Figure 2-2.

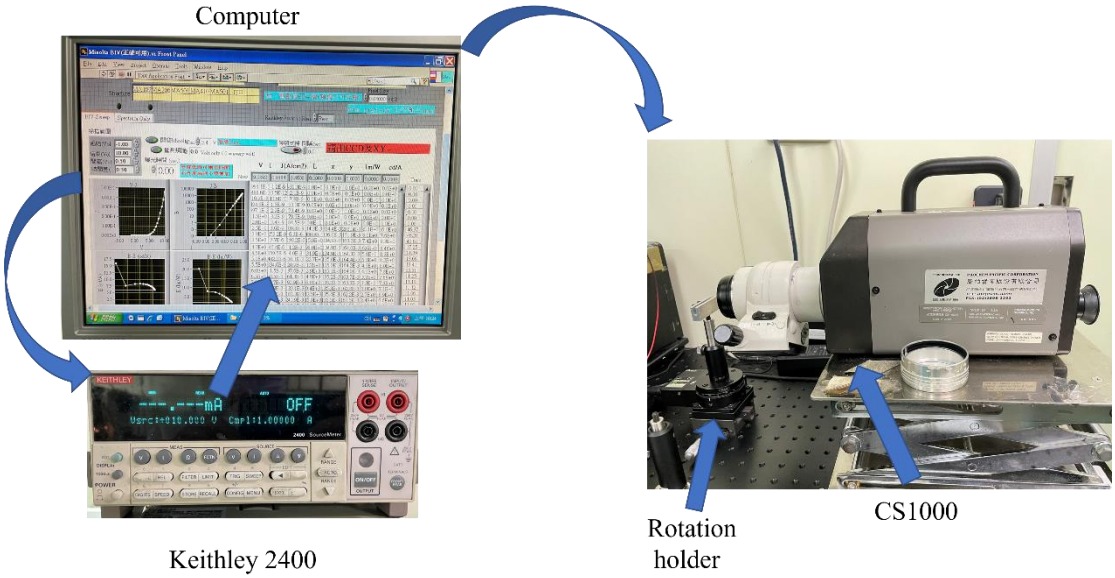

Fig. 2-2 Measurement system for OLED J-V-L, EQE, and operation lifetime performances.

2.2.2 TrEL measurement

For TrEL measurement, the time-dependent emission from the OLED was detected by a photomultiplier tube (Hamamatsu H6780-20) which was driven with a wave function generator (Agilent 33550B). The intensity data were then recorded by a

doi:10.6342/NTU202503850

computer using the TDS2004C OpenChoice program. The sensitivity of the PMT can be adjusted using the Keithley 2400 instrument. The current through the OLED can be obtained by measuring the voltage across the resistor (50Ω) connected in series with the OLED. The input electrical signal can also be detected by an oscilloscope. The setup of the TrEL system is shown in Figure 2-3.

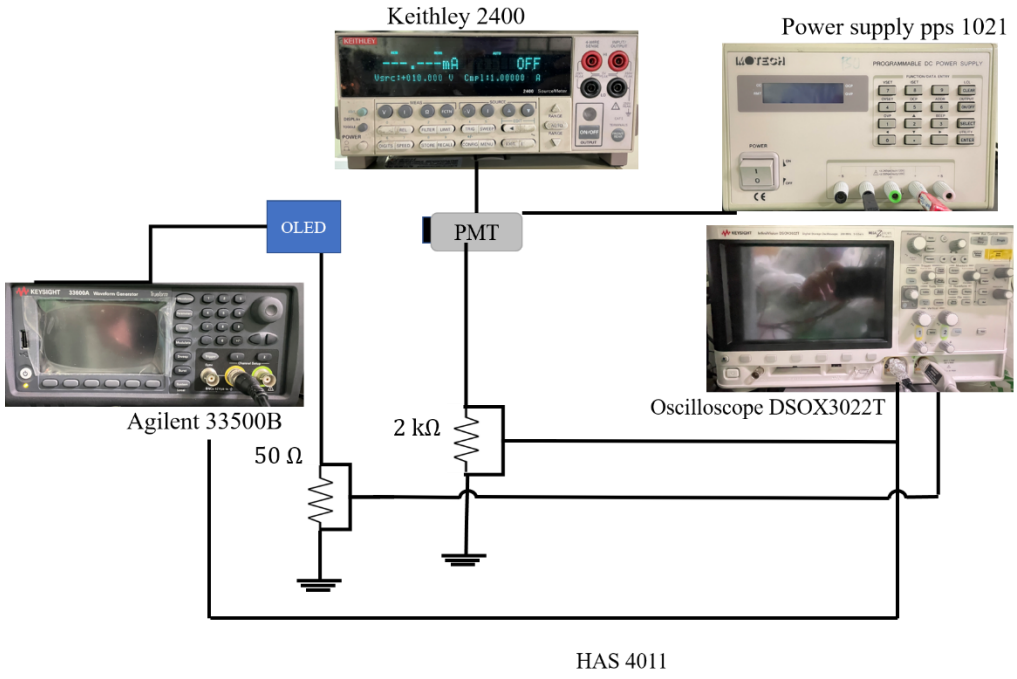

Fig. 2-3 TrEL measurement system.

2.2.3 TrPL and PLQY measurement

The decay curves of TrPL in Chapter 3, 4, and 5 were obtained using a picosecond pulsed diode laser with an emission wavelength of 375 nm as the excitation source, and a fluorescence spectrometer (Horiba iHR320) for optical signal detection with a time-resolution of 40 ps was used th detect optical signal with selected wavelength by PMT (Horiba DM302). The setup of the TrPL system is shown in Fig. 2-4. The PLQY in Chapter 4 was obtained using a similar TrPL system setup, but with an integrated sphere (Horiba Quanta-φ) instead of the sample holder, and a xenon lamp (Horiba FL-1039A, 450 W) as the excitation source, as shown in Fig. 2-4.

doi:10.6342/NTU202503850

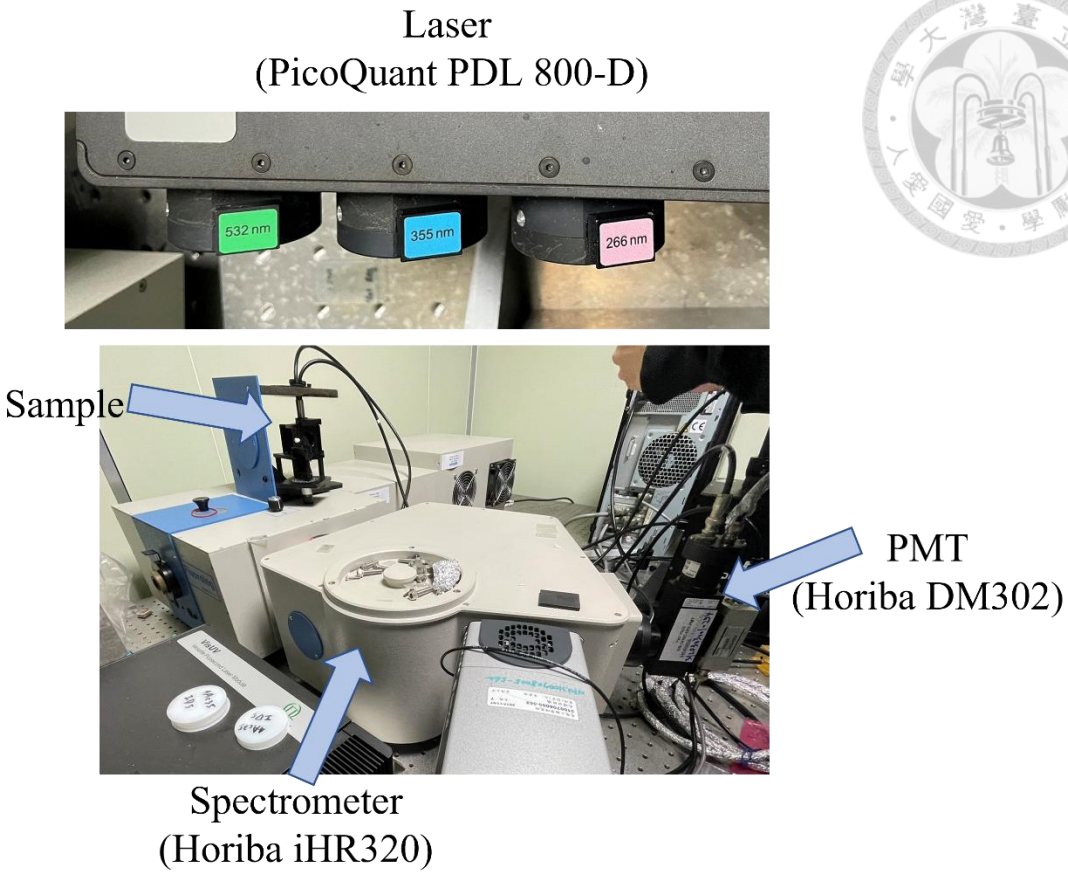

Fig. 2-4 TrPL measurement system.

2.2.4 Absorption and PL spectra

Absorption and PL spectroscopy were used to study the energy band gap of organic materials, energy transfer processes in host-dopant systems, and device degradation mechanisms. The UV-Vis spectrophotometer (Hitachi U-3010) and the fluorescence spectrophotometer (Hitachi F-4500) used in this study were supported by Prof. Man-Kit Leung's laboratory, as shown in Figures 2-5(a) and 2-5(b), respectively. Absorption spectra from 190 nm to 900 nm were acquired using the Hitachi U-3010. Using the Hitachi F-4500, we can obtain PL spectra by exciting the sample at a selected

doi:10.6342/NTU202503850

wavelength using a xenon lamp with a monochromator and collecting the signal using a PMT.

(a) (b)

Fig. 2-5(a) The UV-vis spectrophotometer (Hitachi U-3010) system, and (b) the PL spectrophotometer (Hitachi F-4500).

2.2.5 Photoelectron spectroscopy

The highest occupied molecular orbital (HOMO) of organic materials was obtained using photoelectron spectroscopy (AC2, Riken Keiki), which was conducted by Prof. Yu-Tai Tao's laboratory, as shown in Figure 2-6. UV photons of different energies were irradiated onto the organic film, and at threshold energy, the photoelectrons were detected, which allowed us to obtain the HOMO value.

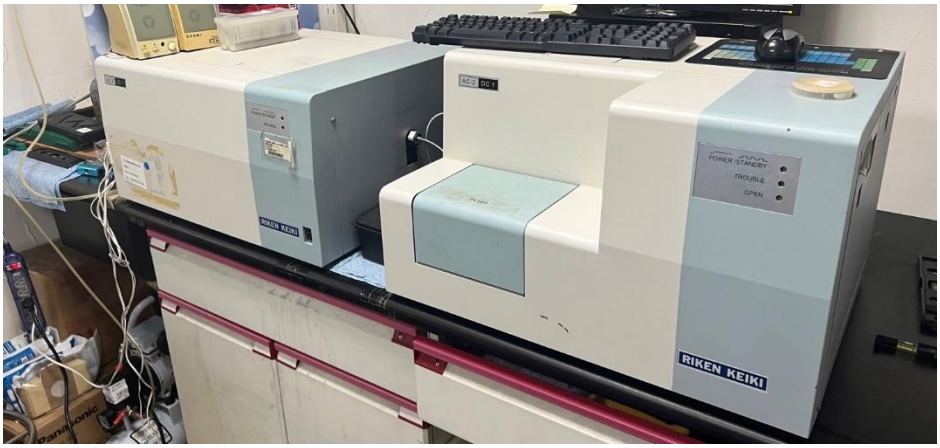

Fig. 2-1 AC2 measurement system.

doi:10.6342/NTU202503850

2.3 References

[1] 林伯彥, 白光有機電激發光元件外部量子效率及壽命之研究, 國立臺灣大學光電工程學研究所碩士論文 (2012).

doi:10.6342/NTU202503850

Chapter 3 High-efficiency blue TADF OLED with 4Ac25CzPY and 4Ac35CzPY as the emitters

3.1 Introduction

In this chapter, we demonstrated sky-blue organic light-emitting diodes (OLEDs) based on acridine-carbazole-pyrimidine materials as the thermally activated delayed fluorescence (TADF) emitters, which were synthesized by Prof. Man-kit Leung's group in the Department of Chemistry at National Taiwan University. The resulting compounds were 10-(3,5-di(9H-carbazol-9-yl)-4-(pyrimidin-2-yl) phenyl)-9,9-dimethyl-9,10-dihydroacridine (4Ac35CzPy) and 10-(2,5-di(9H-carbazol-9-yl)-4-(pyrimidin-2-yl) phenyl)-9,9-dimethyl-9,10-dihydroacridine (4Ac25CzPy) [1]. Transient PL (TrPL) results revealed delayed emission in 4Ac35CzPy and 4Ac25CzPy based thin films. By doping 4Ac35CzPy and 4Ac25CzPy emitters into 9,9'-(2-(1-phenyl-1H-benzo[d]imidazol-2-yl)-1,3-phenylene)bis(9H-carbazole) (*o*-2CbzBz) host, the OLEDs achieved maximum EQE of 21.2% and 12.4%, respectively [2].

doi:10.6342/NTU202503850

3.2 Photophysical properties of 4Ac25CzPy and 4Ac35CzPy

This section provides an overview of photophysical properties of 4Ac35CzPy and 4Ac25CzPy with molecular structures shown in Fig. 3-1.

(a) (b)

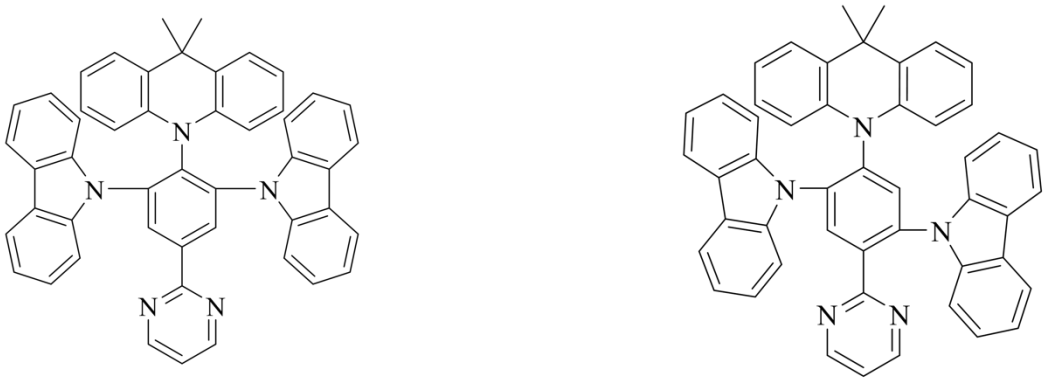

Fig. 3-1 Molecular structures of (a) 4Ac35CzPy and (b) 4Ac25CzPy.

Table 3-1 presented the photophysical properties of the two compounds, while Fig. 3-2 (a) and (b) showed absorption and photoluminescence (PL) spectra of two materials in solution and neat film, respectively. The PL spectra of 4Ac25CzPy and 4Ac35CzPy in solution revealed emission peak at 402 and 443 nm, respectively. Two emitters were incorporated into two host materials, 9,9'-(2-(1-phenyl-1H-benzo[d]imidazol-2-yl)-1,3-phenylene)bis(9H-carbazole) (*o*-2CbzBz) and 9,9',9''-(2-(1-phenyl-1H-benzo[d]imidazol-2-yl)benzene-1,3,5-triyl)tris(9H-carbazole) (*o*-3CbzBz) with 12% dopant concentration for OLED application. Hence, we also included absorption and PL spectra of *o*-2CbzBz and *o*-3CbzBz in Fig. 3-2 (b). PL spectra of the host materials showed good overlap with the absorption spectra of 4Ac35CzPy and 4Ac25CzPy, indicating efficient energy transfer from the host to the dopants. Fig. 3-3 showed the measurement results of photoelectron spectroscopy with Riken AC2 for the two compounds to determine their highest occupied molecular orbital (HOMO) level. The

optical band gap was estimated from the onset wavelength of the absorption spectrum shown in

Fig. 3-2 and calculated used the following equation.

$$E_g\ (eV) = 1240 / \lambda_{onset}^{Abs}\ (nm) \quad (3\text{-}1)$$

where E_g and λ_{onset}^{Abs} represented the optical bandgap and onset wavelength of the absorption spectrum. Therefore, the lowest occupied molecular orbital (LUMO) was obtained from the optical band gap and HOMO level, which was summarized in Table 3-1. Photophysical properties of 4Ac25CzPy and 4Ac35CzPy-doped film shown a smaller knr,T suppresses triplet loss pathways, allowing excitons in the T1state to persist longer. When krISC is not particularly large, the triplet population becomes effectively stored, leading to an extended τd elongated TrPL decay tails, and an increase in the delayed emission contribution was shown in Fig. 3-4 TrPL measurement of 4Ac25CzPy and 4Ac35CzPy in neat film and doped film (12% in *o*-2CbzBz) with (a) 40 ns and (b) 400 μs window.and the performance was summarized in Table 3-1.

Table 3-1 Photophysical properties of four compounds.

Compound	λ_{max} [a] (nm)	λ_{onset}^{Abs} [a] (nm)	E_g [a, b] (eV)	λ_{PL} [a] (nm)	E_S [c] (eV)	E_T [d] (eV)	ΔE_{ST} (eV)	HOMO [e] (eV)	LUMO [e] (eV)
4Ac25CzPy	230,284,334/290,336	402/436	2.73/2.84	508/493	3.28	2.96	0.15	5.51/5.67	2.78/2.83
4Ac35CzPy	232,285,335/290,336,406	443/460	2.62/2.69	480/508	2.93	2.72	0.14	5.47/5.57	2.85/2.88
o-2CbzBz	284,319,335/291,325,337	324/369	3.63/3.50	428/398	3.61	3.10	0.39	5.76/5.7	2.26/2.31
o-3CbzBz	290,322,335/	378/390	3.57/3.36	419/410	3.49	3.10	0.25	5.77/5.80	2.20/2.66

doi:10.6342/NTU202503850

289,325,337

[a]Measured in 1x10^{-5} M 2-methyl THF solution/ 60-nm thickness in the film state.; [b] E_g =1240.8/ λ_{onset} of absorption (eV) ; [c]S_1 =1240.8/λ (cross point wavelength of absorption and fluorescence spectra) (eV), [d]T_1 =1240.8/ λ_{onset} of LTPH (eV) ; [e] Obtained with CV 1x10^{-5} M 2-methyl THF solution and film measured from AC2 and 60-nm thin-film optical gap, $E_{LUMO} = E_{HOMO} - E_g$; [f]Measured in 1x10^{-5} M 2-methyl THF solution, neat film and 12 % emitter doped in *o*-2CbzBz..

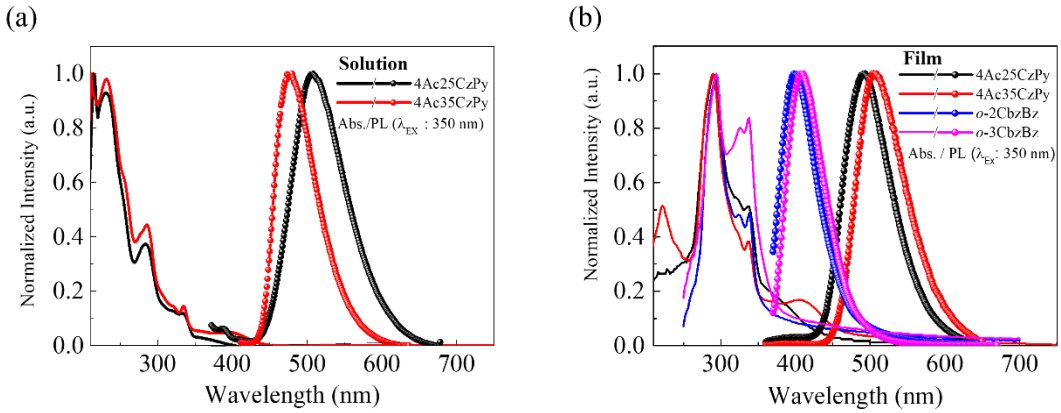

Fig. 3-2 Absorption and PL spectra of (a) 4Ac25CzPy and 4Ac35CzPy in 1 x 10^{-5} M 2-methyl THF solution, and (b) four compounds in neat film.

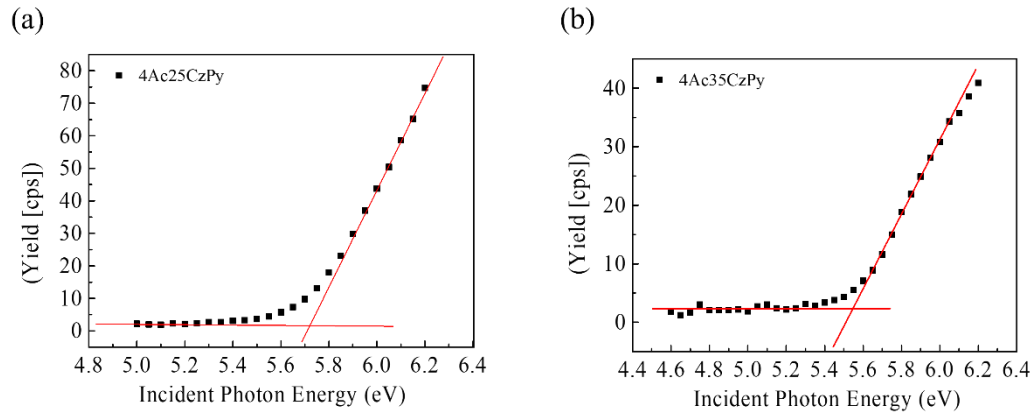

Fig. 3-3 AC2 measurement of (a) 4Ac35CzPy and (b) 4Ac25CzPy.

doi:10.6342/NTU202503850

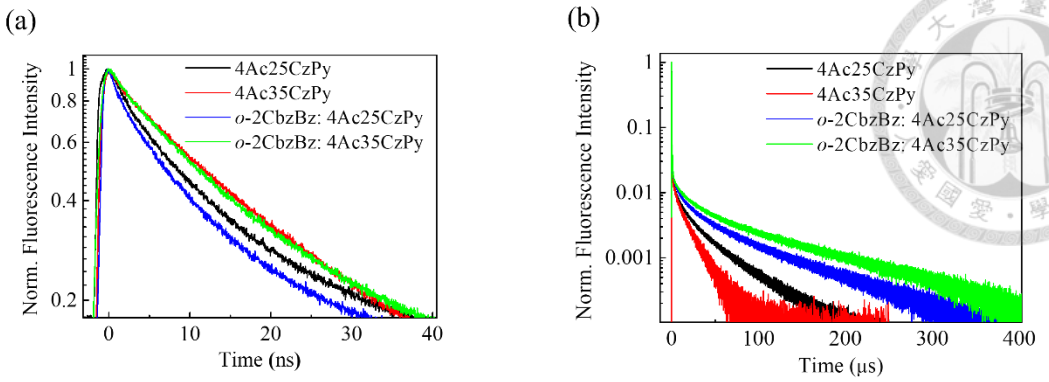

Fig. 3-4 TrPL measurement of 4Ac25CzPy and 4Ac35CzPy in neat film and doped film (12% in *o*-2CbzBz) with (a) 40 ns and (b) 400 μs window.

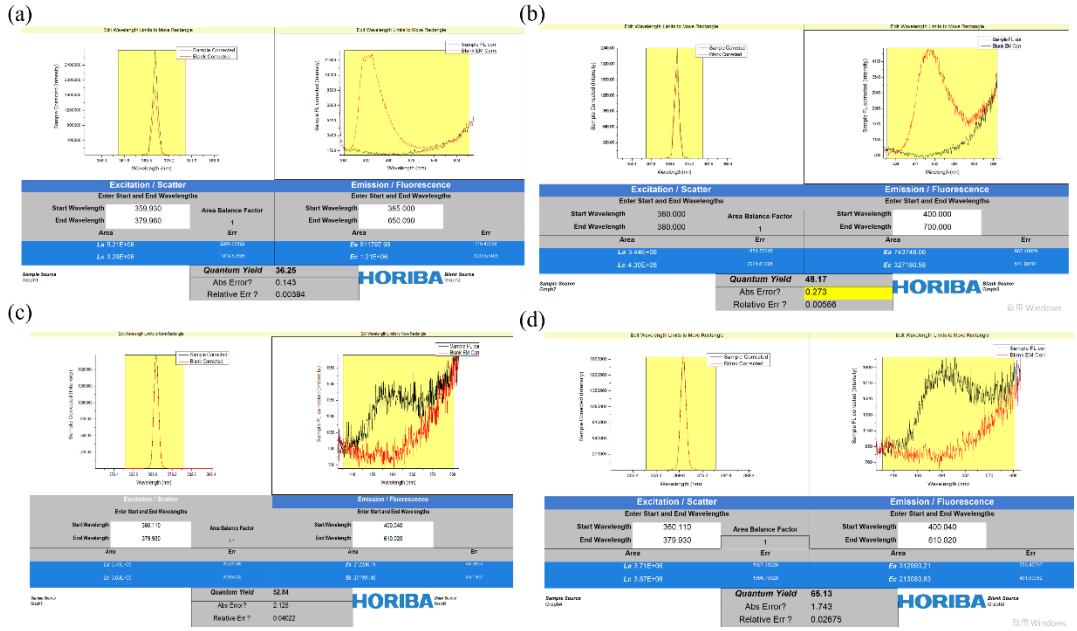

Fig. 3-5 PLQY of thin films: (a) 4Ac25CzPy neat film, (b) 4Ac35CzPy neat film, (c) 12% 4Ac25CzPy doped in *o*-2CbzBz, and (d) 12% 4Ac35CzPy doped in *o*-2CbzBz.

Table 3-2 Photophysical results of 4Ac25CzPy and 4Ac35CzPy-doped film.

	$\Phi_{total}/\Phi_{prompt}/\Phi_{delay}$[a] [%]	τ_p[b] [ns]	τ_d[b] [μs]	$k_{r,s}$[c] [x 10^7 s^{-1}]	$k_{nr,T}$[c] [x 10^3 s^{-1}]	k_{ISC}[d] [x 10^7 s^{-1}]	k_{rISC}[d] [x 10^4 s^{-1}]
4Ac25CzPy	52.8/11.4/41.4	8.2	60.0	1.4	9.4	10.9	6.8
4Ac35CzPy	65.1/11.7/53.4	11.8	73.2	1.0	4.8	7.4	7.0

[a] Photoluminescence quantum yield of overall, prompt and delayed fluorescence. [b] Exciton lifetime of prompt and delayed fluorescence obtained from TrPL. [c] Rate constant of radiative decay from S_1 to S_0 ($k_{r,s}$) and nonradiative decay of T_1 to S_0 ($k_{nr,T}$). [d] Rate constant of intersystem crossing (ISC) and reverse intersystem crossing (rISC).

doi:10.6342/NTU202503850

3.3 Device performances of 4Ac25CzPy and 4Ac35CzPy as OLED emitter

In our OLEDs, we employed 4,4'-Cyclohexylidenebis[N, N-bis(4-methylphenyl)benzenamine] (TAPC), N,N'-dicarbazolyl-3,5-benzene (mCP), and Diphenylbis(4-(pyridin-3-yl)phenyl)silane (DPPS) as the hole transporting layer (HTL), electron blocking layer (EBL), and electron transporting layer (ETL), respectively. The device architecture was chosen with a focus on energy level alignment and exciton stabilization. Specifically, *o*-2CbzBz was adopted as a bipolar host material. Its absorption spectrum exhibited strong overlap with the emission of o-2CbzBz and the absorption bands of both 4Ac25CzBz and 4Ac35CzBz, ensuring efficient host-to-guest energy transfer. In addition, the HOMO and LUMO energy levels of *o*-2CbzBz (–5.8 eV and –2.3 eV, respectively) were well matched to confine excitons within the emission layer (EML), thereby supporting radiative recombination. Consequently, this host–guest configuration not only enhances device performance but also serves as an effective platform for probing triplet-related processes in TADF systems. The molecular structures of TAPC, mCP, and DPPS, along with the device energy diagram, were shown in Fig. 3-6 and Fig. 3-7. The optimized TADF OLED device structure with

doi:10.6342/NTU202503850

acridine carbazole emitters was presented in Table 3-3, while their performances were summarized in Table 3-4.

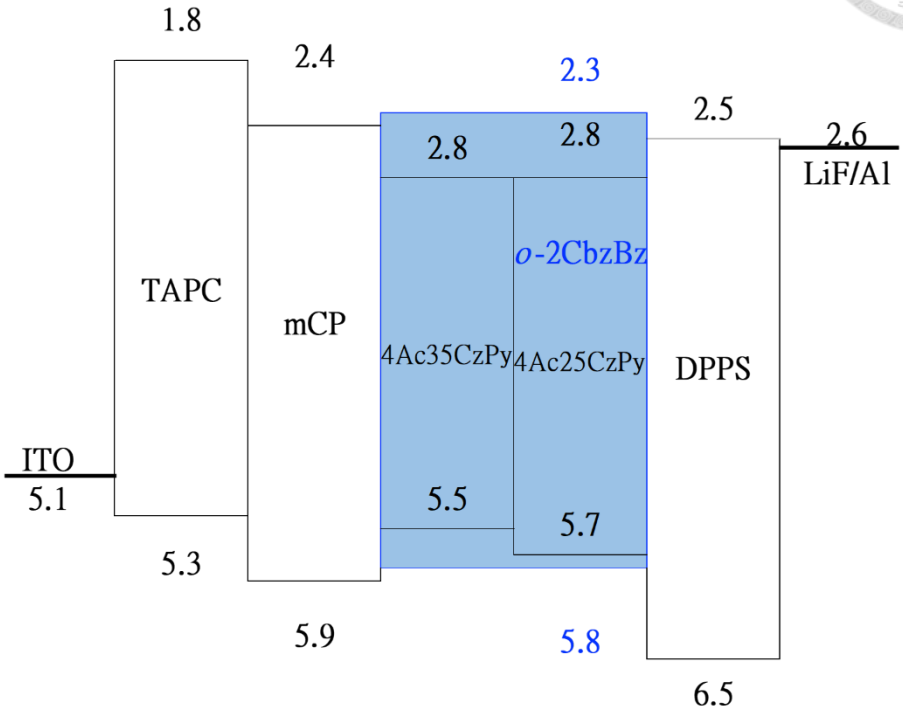

Fig. 3-6 Energy diagram of OLEDs with *o*-2CbzBz as host and 4Ac35CzPy and 4Ac25CzPy as the emitters.

doi:10.6342/NTU202503850

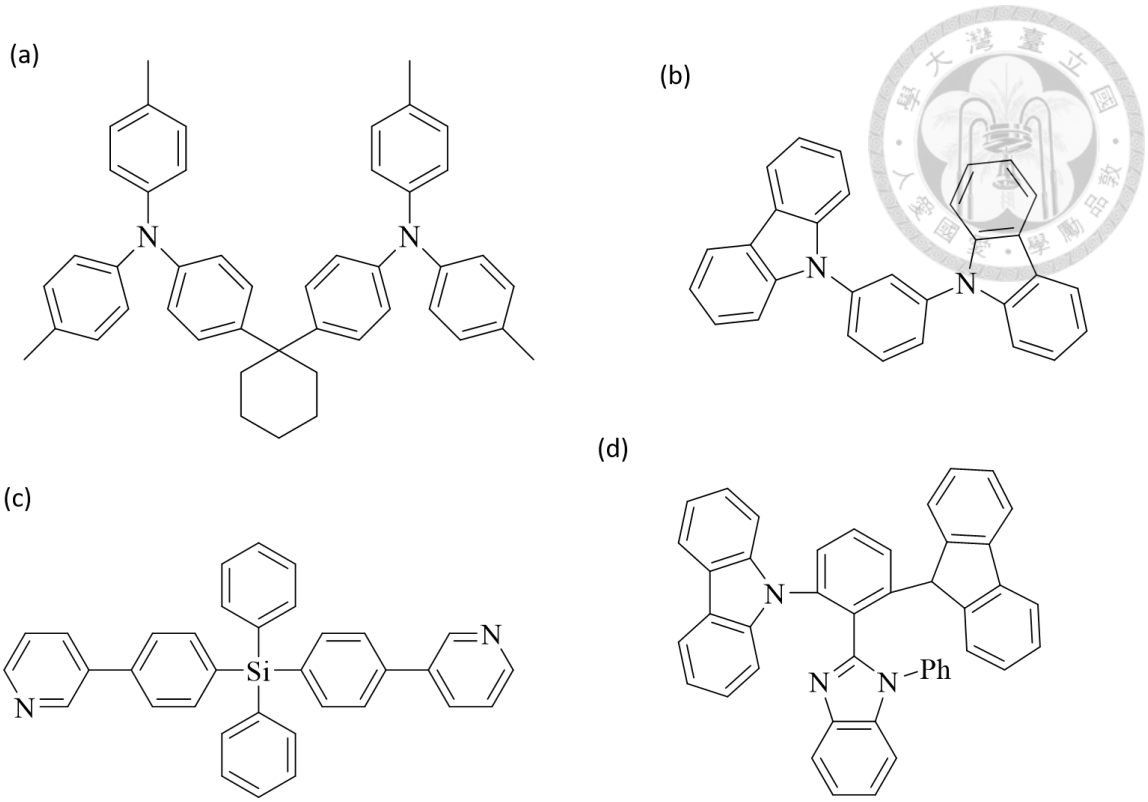

Fig. 3-7 Molecular structures of (a) TAPC, (b) mCP, (c) DPPS, and (d) *o*-2CbzBz.

Table 3-3 Optimized device structure of TADF OLED with 4Ac25CzPy and 4Ac35CzPy emitters.

Device	HTL	EBL	EML (30 nm)	ETL	EIL/cathode
	TAPC	mCP	*o*-2CbzBz: 12% dopant	DPPS	LiF/Al
3-1	50	10	4Ac25CzPy	45	0.8/120
3-2			4Ac35CzPy		

unit: nm

Table 3-4 OLEDs performances of devices 3-1 and 3-2.

Device	**Voltage[a] (V)**	**Max. Max. Luminance (cd/m^2)**	**CE[b] (cd/A)**	**PE[b] (lm/W)**	**EQE[b] (%)**	**CIE[c] (x,y)**
3-1 (4Ac25CzPy)	6.7/3.3	2635	31.5/27.6/16.6	28.3/20.7/8.7	12.4/10.9/6.6	(0.166, 0.328)
3-2 (4Ac35CzPy)	7.8/3.3	2724	53.4/42.7/20.3	48.0/31.2/10.5	21.2/17.1/11.9	(0.185, 0.401)

[a]at J = 10 mA/cm^2/L= 1 cd/m^2; [b]CE/PE/EQE measured at maximum/100 cd/m^2/1000 cd/m^2; [c]measured at maximum current

doi:10.6342/NTU202503850

efficiency.

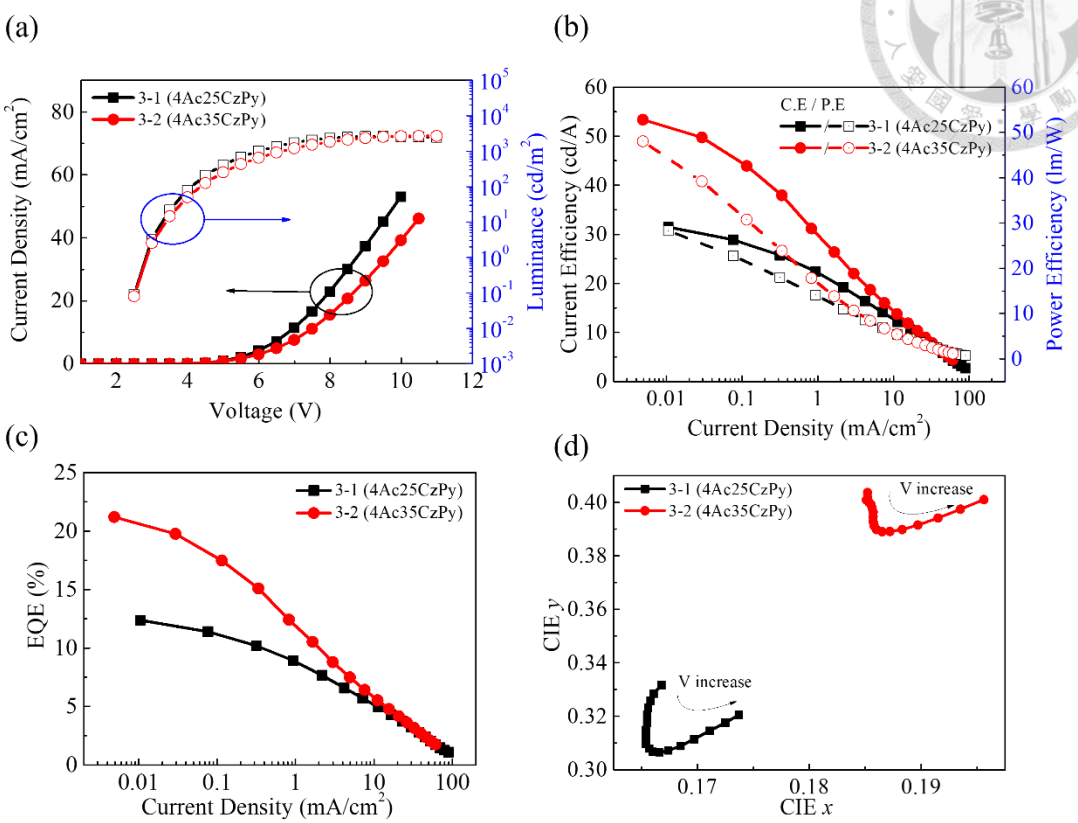

Fig. 3-8 (a) J-L-V curves, (b) current efficiency and power efficiency versus J, (c) EQE versus J, and (d) CIE coordinates at different voltages.

Fig. 3-8 (a) presented the J-L-V characteristics of the devices. Fig. 3-8 (b) and (c) showed the current efficiency, power efficiency, and EQE under different current densities. For 4Ac25CzPy and 4Ac35CzPy, the maximum current efficiencies were 31.5 cd/A and 53.4 cd/A, the maximum power efficiencies were 28.3 lm/W and 48.0 lm/W, and the maximum EQEs were 12.4% and 21.2%, respectively. Fig. 3-8 (d) illustrated the CIE coordinates as a function of driving voltage. Among the two OLEDs, device 3-1 exhibited a lower CIE-y value, indicating that 4Ac25CzPy had a more bluish

doi:10.6342/NTU202503850

emission compared to 4Ac35CzPy in photophysical properties. The 4Ac35CzPy achieved the highest EQE value (21.2%) compared to 4Ac25CzPy, which was attributed to its higher PLQY doped in *o*-2CbzBz as listed in Table 3-2 Photophysical results of 4Ac25CzPy and 4Ac35CzPy-doped film. Fig. 3-9 showed the electroluminescence (EL) spectra of OLEDs with 3-1 and 3-2 as the EML, featuring spectral peaks at 484 nm and 490 nm, respectively, which were consistent with their PL spectra. Fig. 3-10 showed the TrEL results, where both devices exhibited long-delayed emission attributed to their TADF characteristics.

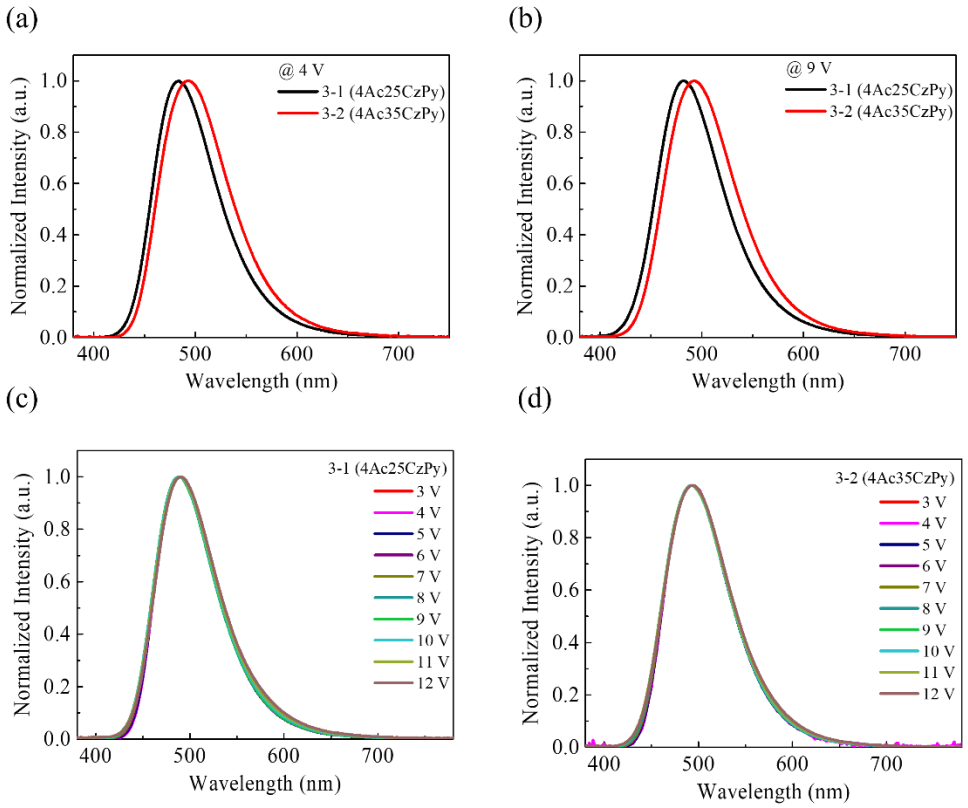

Fig. 3-9 EL spectra of devices (a) 3-1 and 3-2 with 4 V, (b) 3-1 and 3-2 with 9 V, (c) 3-1, and (d) 3-2 with different voltages.

doi:10.6342/NTU202503850

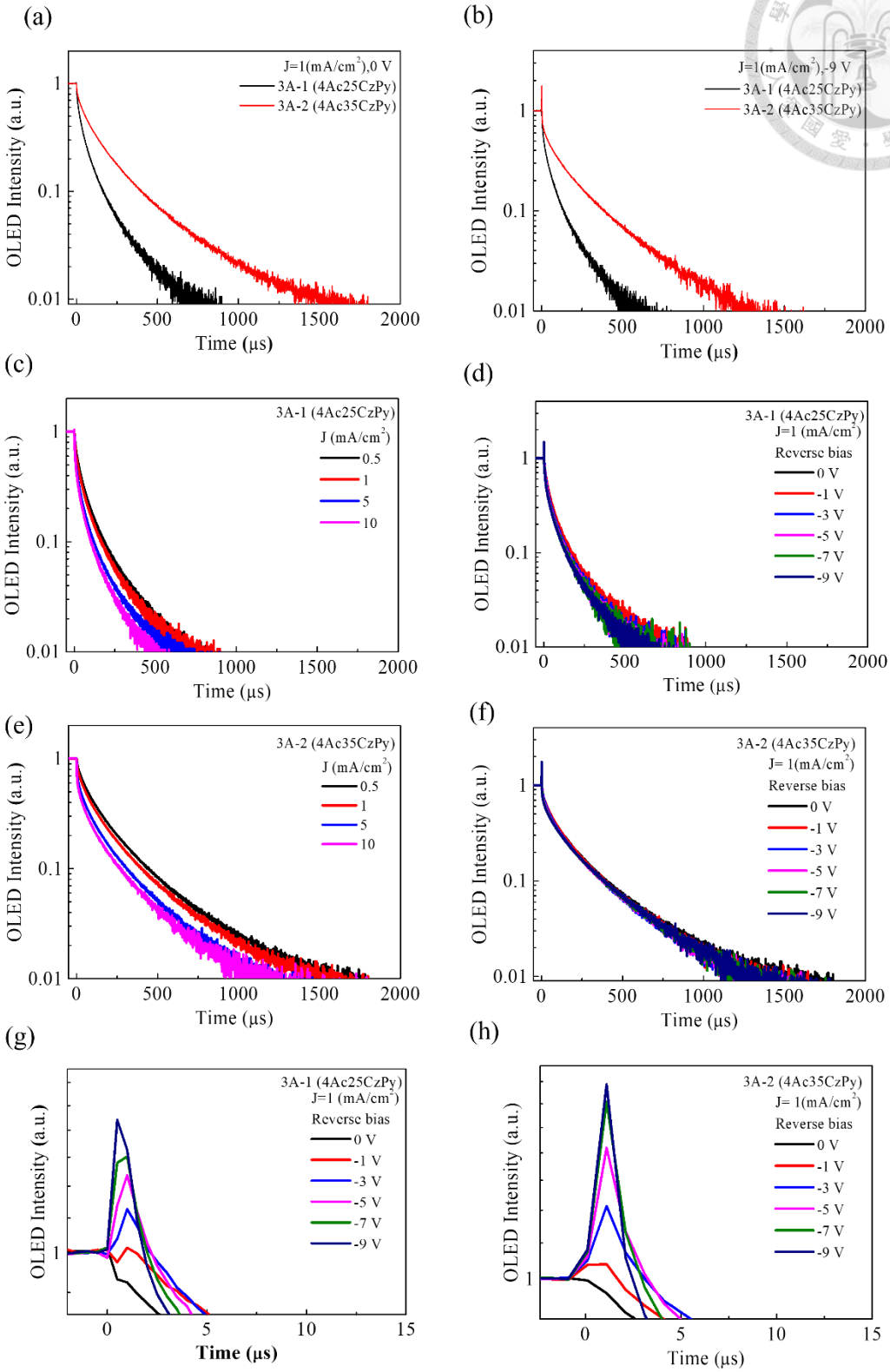

Fig. 3-10 TrEL of devices (a) 3-1 and 3-2 with J = 1 mA/cm^2, (b) 3-1 and 3-2 with J = 1 mA/cm^2, and switched to -9 V after t > 0, (c) 3-1 with different current densities, (d)

doi:10.6342/NTU202503850

3-1 with different reverse bias after t > 0, (e) 3-2 with different current densities, (f) 3-2 with different reverse bias after t > 0, (g) shorter time scale (15 μs) of 3-1 with different reverse bias after t > 0, and (h) shorter time scale (15 μs) of 3-2 with different reverse bias after t > 0.

3.4 Optimization procedure of TADF OLED with 4Ac35CzPy as the emitter

In sections 3-4, we demonstrated the optimization process with 4Ac35CzPy as the emitters by selecting the host materials, varying dopant concentrations, and changing ETL and HTL thicknesses for achieving highest maximum EQE.

3.4.1 Selection of host materials

To achieve higher EQE, we first selected the host materials between *o*-2CbzBz and *o*-3CbzBz for 4Ac35CzPy emitter. The energy diagram of the OLEDs was shown in Fig. 3-11, with two hosts, i.e. *o*-2CbzBz and *o*-3CbzBz. Table 3-5 presented the

doi:10.6342/NTU202503850

device structures, and their performances were summarized in Table 3-6.

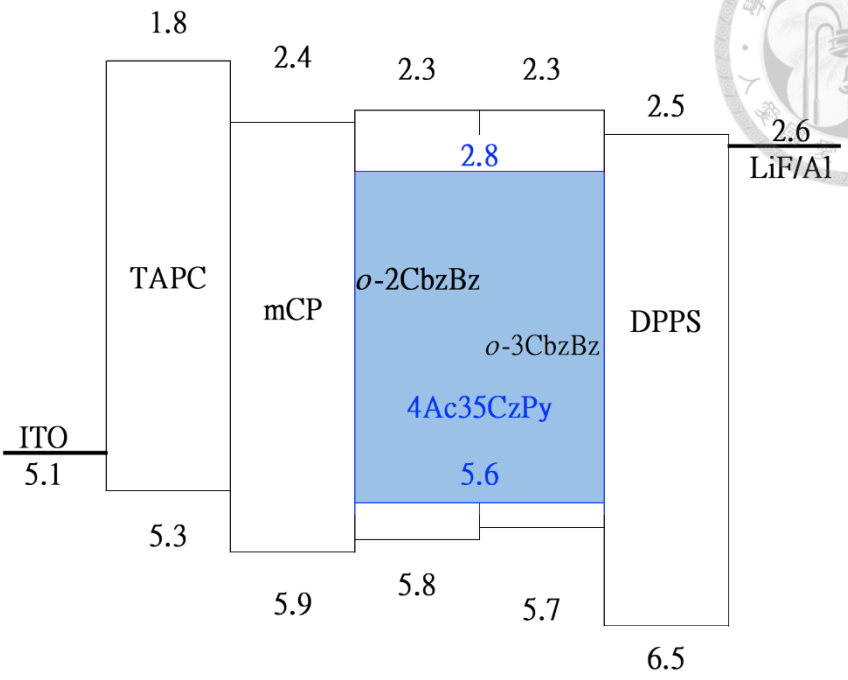

Fig. 3-11 Energy diagram of OLEDs with 4Ac35CzPy-doped in *o*-2CbzBz and *o*-3CbzBz as the EML.

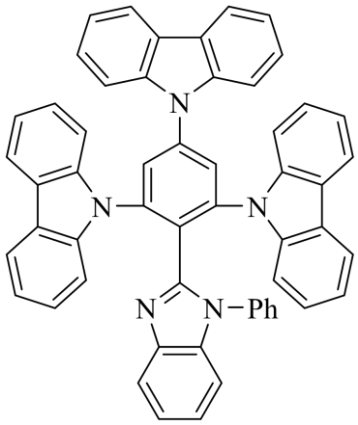

Fig. 3-12 Molecular structure of *o*-3CbzBz.

Table 3-5 Device structures of OLEDs with *o*-2CbzBz and *o*-3CbzBz.

Device	HTL	EBL	EML	ETL	EIL/cathode
	TAPC	mCP	Host: 12% 4Ac35CzPy	DPPS	LiF/Al
3-2	50	10	*o*-2CbzBz	55	0.8/120

doi:10.6342/NTU202503850

3-3		*o*-3CbzBz

unit: nm

Table 3-6 OLED performances of devices (a) 3-2 and (b) 3-3.

Device	Voltage[a] (V)	Max. Luminance (cd/m^2)	CE[b] (cd/A)	PE[b] (lm/W)	EQE[b] (%)	CIE[c] (x,y)
3-2 (*o*-2CbzBz)	7.8/3.3	2724	53.4/42.7/20.3	48.0/31.2/10.5	21.2/17.1/11.9	(0.185, 0.401)
3-3 (*o*-3CbzBz)	6.3/3.1	3938	36.3/33.7/16.8	28.5/25.5/8.9	13.4/11.9/6.3	(0.194, 0.425)

[a]at J = 10 mA/cm^2/L= 1 cd/m^2; [b]CE/PE/EQE measured at maximum/100 cd/m^2/1000 cd/m^2; [c]measured at maximum current efficiency.

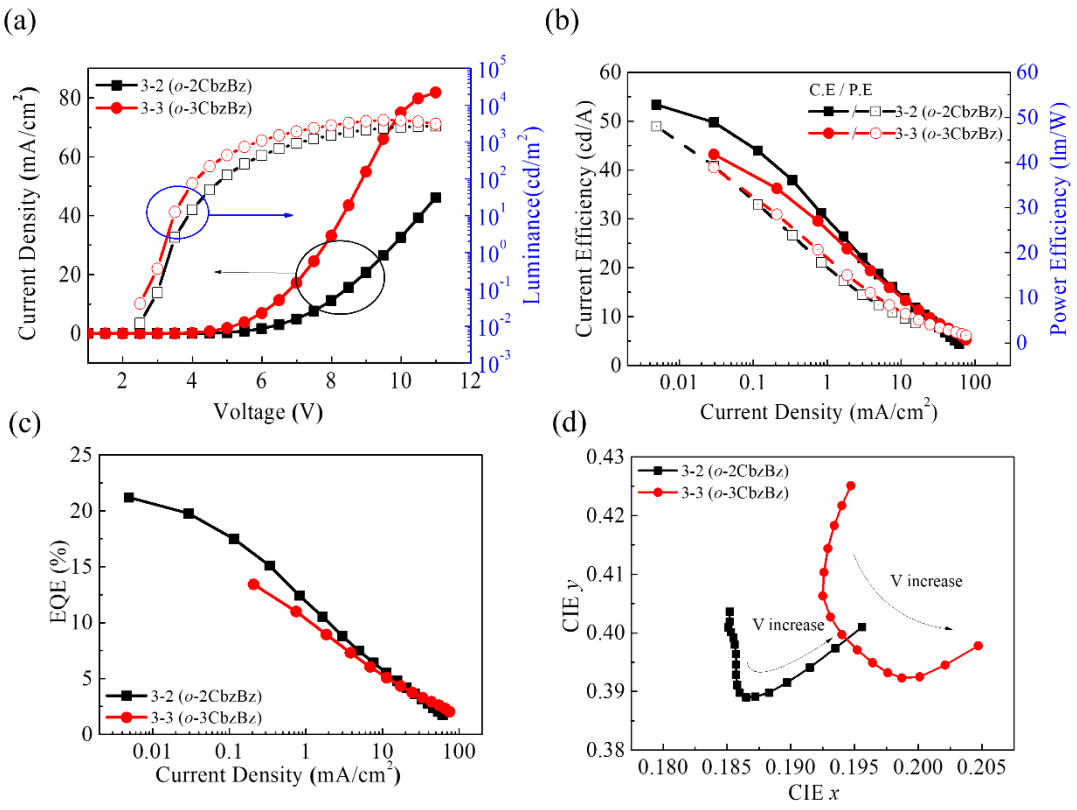

Fig. 3-13 (a) J-L-V curves, (b) current efficiency and power efficiency versus J, (c) EQE versus J, and (d) CIE coordinates at different voltages.

doi:10.6342/NTU202503850

Table 3-5 presented the OLED performances with *o*-2CbzBz and *o*-3CbzBz as hosts doped with 4Ac35CzPy as the EML. Fig. 3-13 (a) showed the J-V curves. Under the same driving voltage, device 3-3 exhibited higher current density and luminance than device 3-2. Current efficiency, power efficiency, and EQE under different current densities were plotted in Fig. 3-13 (b), (c), and (d), respectively. Devices 3-2 and 3-3 exhibited maximum current efficiency, maximum power efficiency, and maximum EQE of 53.4 cd/A and 36.2 cd/A, 48.0 lm/W and 28.5 lm/W, and 21.2% and 13.4%, respectively. Fig. 3-13 (d) showed CIE coordinates, where device 3-2 exhibited a lower CIE-y value. Fig. 3-14 presented the EL spectra of devices 3-2 and 3-3, where both exhibited 4Ac35CzPy emission, indicating successful energy transfer from host to dopant. Fig. 3-15 showed the TrEL measurement of devices 3-2 and 3-3, where delayed emission was observed from both OLEDs.

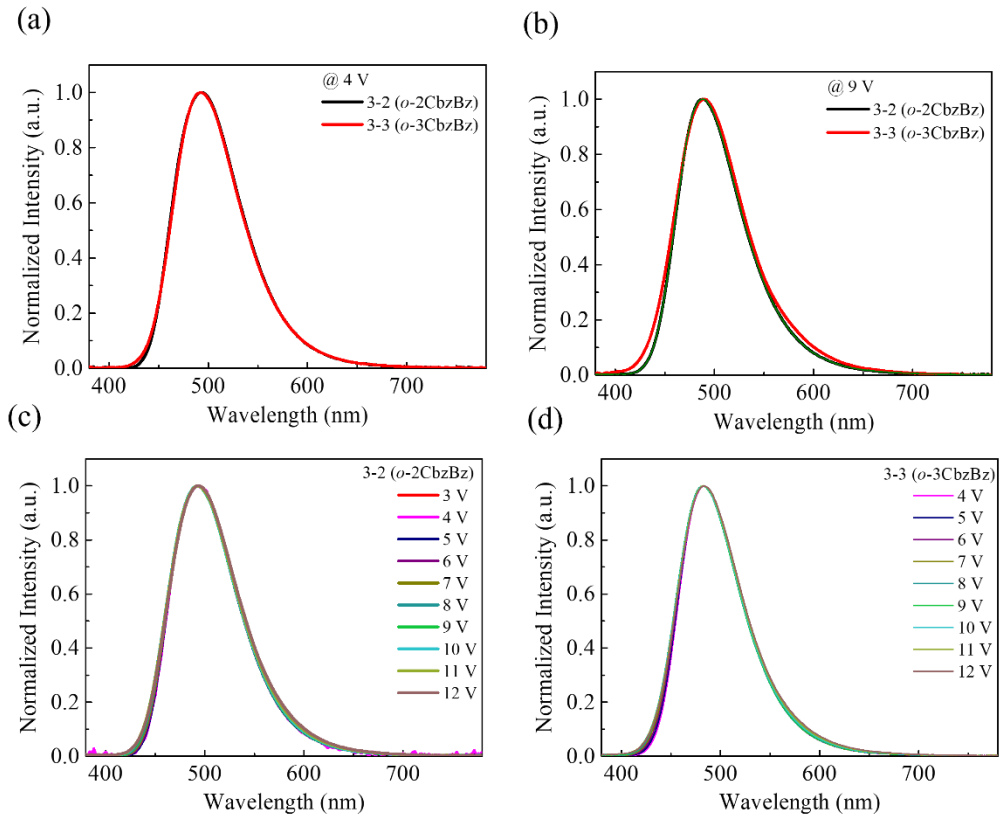

Fig. 3-14 EL spectra of devices (a) 3-2 and 3-3 with 4 V, (b) 3-2 and 3-3 with 9 V, (c)

doi:10.6342/NTU202503850

3-2, and (d) 3-3 with different voltages.

doi:10.6342/NTU202503850

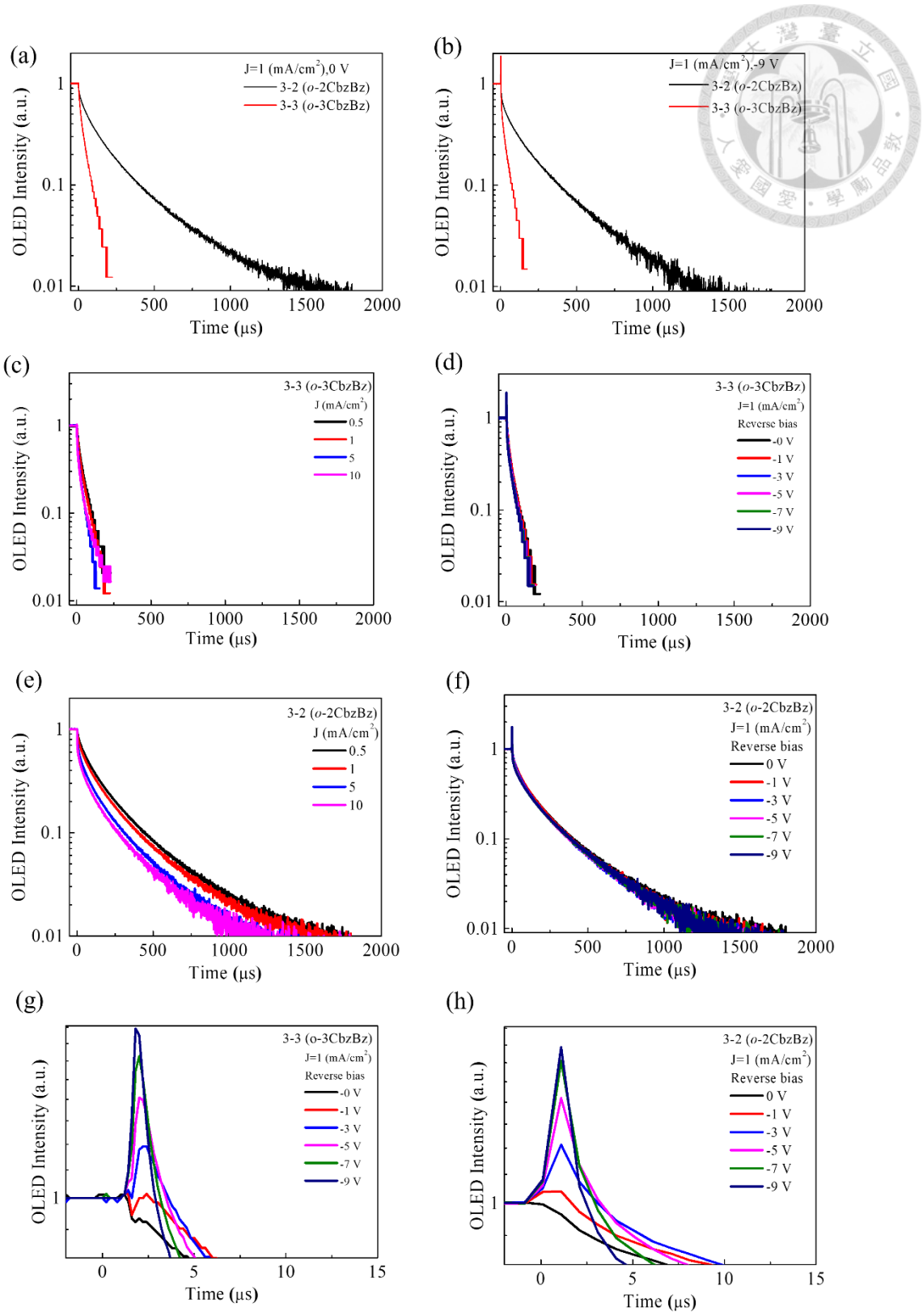

Fig. 3-15 TrEL of devices (a) 3-2 and 3-3 with J = 1 mA/cm^2, (b) 3-2 and 3-3 with J = 1 mA/cm^2, and switched to -9 V after t > 0, (c) 3-2 with different current densities, (d) 3-2 with different reverse bias after t > 0, (e) 3-3 with different current densities, (f) 3-

doi:10.6342/NTU202503850

3 with different reverse bias after t > 0, (g) shorter time scale (15 μs) of 3-3 with different reverse bias after t > 0, and (h) shorter time scale (15 μs) of 3-2 with different reverse bias after t > 0.

3.4.2 Optimization of dopant concentration

After selecting *o*-2CbzBz as the host of the OLEDs, then we changed the 4Ac35CzPy concentration in *o*-2CbzBz from 9%, 12%, to 15% for optimizing the maximum EQE. Table 3-7 showed the device structures and Fig. 3-16 showed the energy diagram of the OLED.

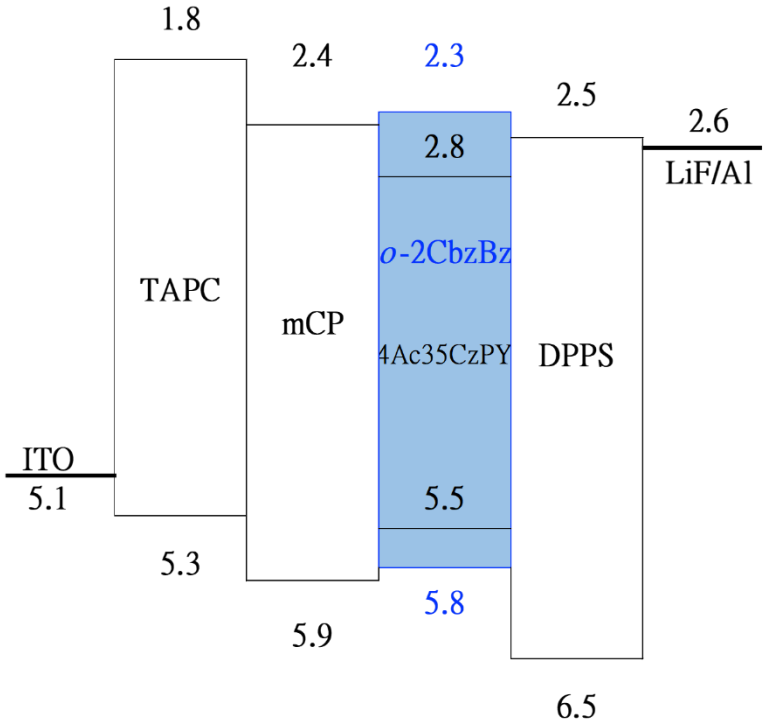

Fig. 3-16 (a) Energy diagram of OLEDs with 4Ac35CzPy doped into *o*-2CbzBz.

Table 3-7 Device structures of OLEDs with different concentrations of 4Ac35CzPy doped into *o*-2CbzBz.

Device	HTL	EBL	EML	ETL	EIL/cathode

doi:10.6342/NTU202503850

	TAPC	*m*CP	*o*-2CbzBz: X% 4Ac35CzPy	DPPS	LiF/Al
3-4			9%		
3-2	50	10	12%	55	0.8/120
3-5			15%		

unit: nm

Table 3-8 OLED performances of devices 3-4, 3-2, and 3-5.

Device	**Voltage[a] (V)**	**Max. Luminance (cd/m^2)**	**CE[b] (cd/A)**	**PE[b] (lm/W)**	**EQE[b] (%)**	**CIE[c] (x,y)**
3-4 (9%)	6.8//3.3	3215	50.4/39.7/18.5	45.3/27.9/9.3	19.7/15.5/7.5	(0.178, 0.382)
3-2 (12%)	7.8/3.3	2724	53.4/42.7/20.3	48.0/31.2/10.5	21.2/17.1/11.9	(0.185, 0.401)
3-5 (15%)	6.5/3.2	3200	51.9/41.3/20.1	46.7/30.6/10.8	19.0/15.3/7.2	(0.181, 0.397)

[a]at J = 10 mA/cm^2/L= 1 cd/m^2; [b]CE/PE/EQE measured at maximum/100 cd/m^2/1000 cd/m^2; [c]measured at maximum current efficiency.

doi:10.6342/NTU202503850

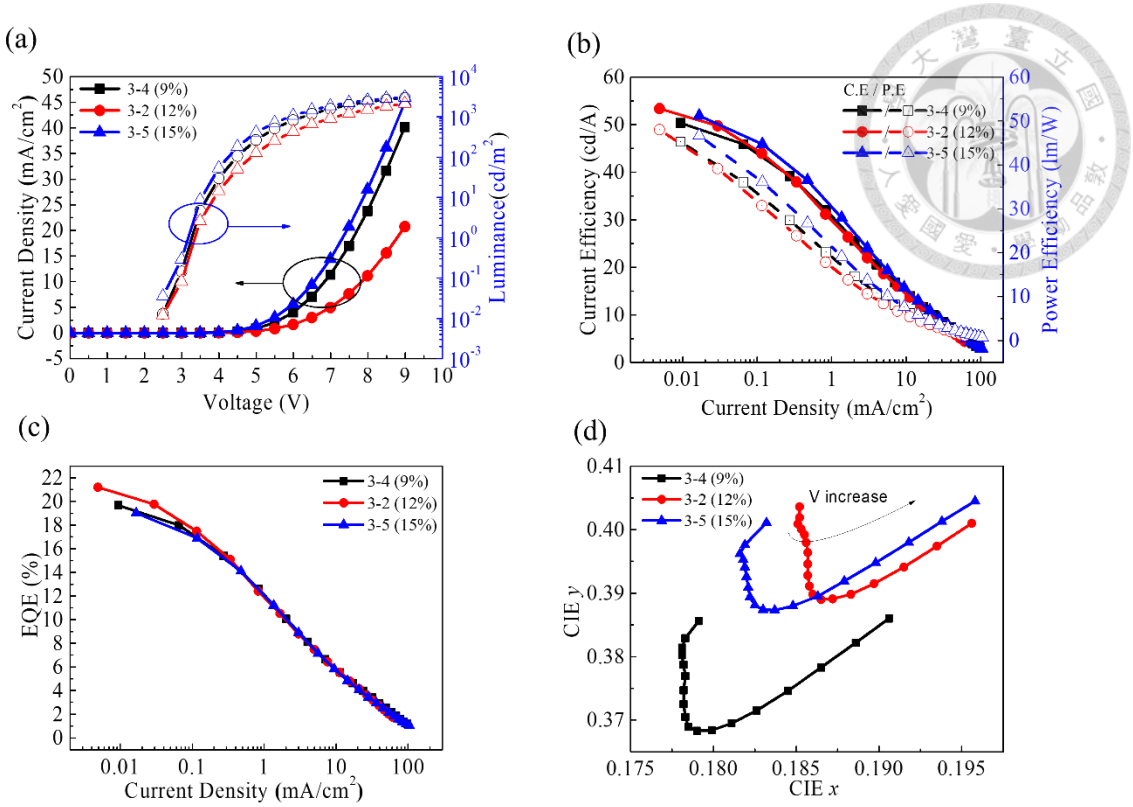

Fig. 3-17 (a) J-L-V curves, (b) current efficiency and power efficiency versus J, (c) EQE versus J, and (d) CIE coordinates at different voltages.

Fig. 3-17 and Table 3-8 summarize the OLED performances with different 4Ac35CzPy concentrations. Fig. 3-17 (a) showed the J-V and L-V characteristics. As the dopant concentration decreased from 15% (device 3-6) the driving voltage at J = 10 mA/cm^2 was 6.8 V, indicating that 4Ac35CzPy improved carrier injection and transport. The OLED doped with 12% 4Ac35CzPy (device 3-2) exhibited the highest current efficiency, power efficiency, and EQE of 53.4 cd/A, 48.0 lm/W, and 21.2%, respectively Fig. 3-17 (b), (c), and (d). Fig. 3-19 showed the TrEL decay curves of devices 3-4, 3-2, and 3-5 in a 1600 μs window, which exhibited long-delayed emission attributed to their TADF characteristics.

doi:10.6342/NTU202503850

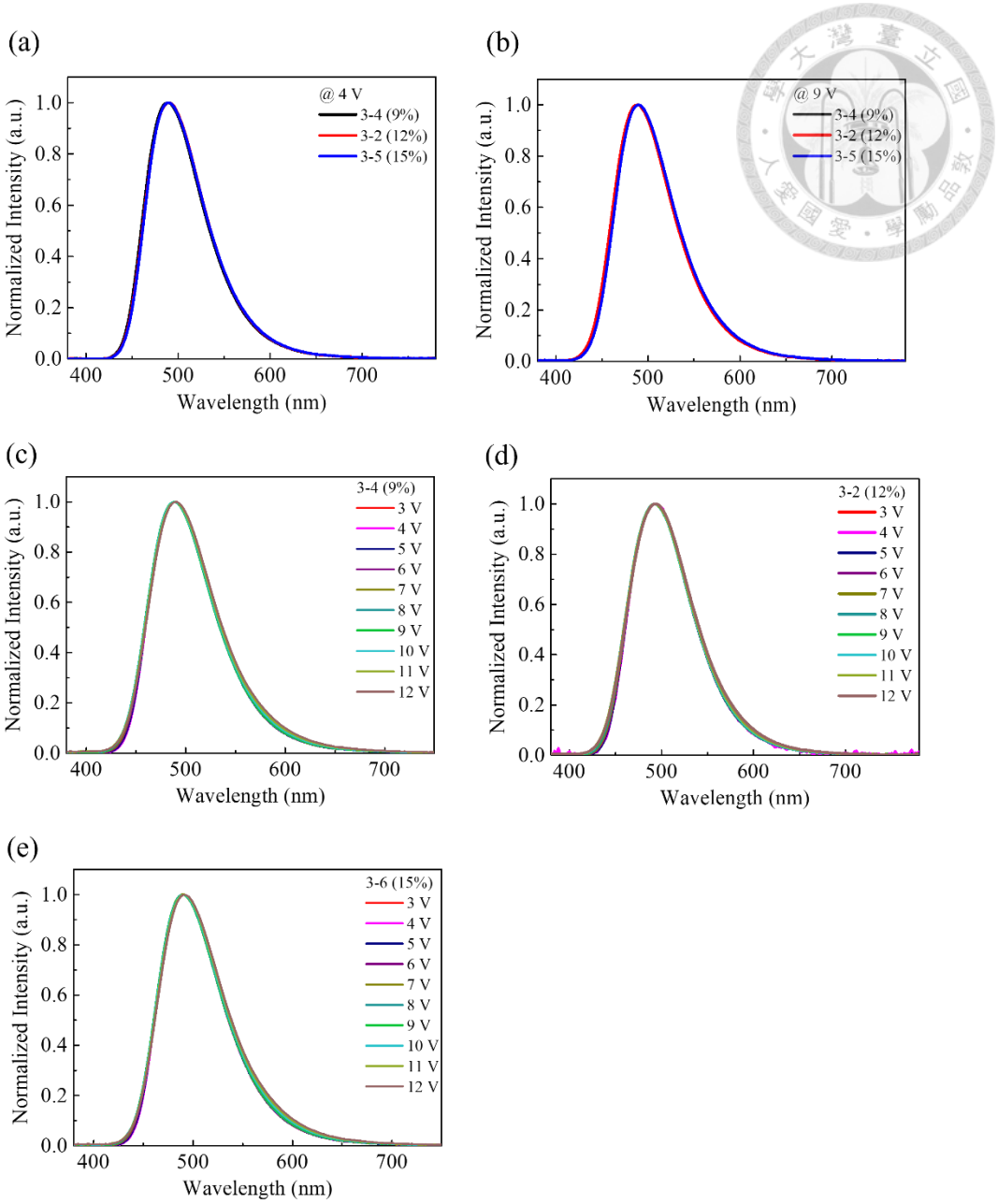

Fig. 3-18 EL spectra of devices (a) 3-4, 3-2 and 3-5 at 4 V, (b) 3-4, 3-2 and 3-5 at 9 V, (c) 3-4, (d) 3-2 and (e) 3-5 with different voltages.

doi:10.6342/NTU202503850

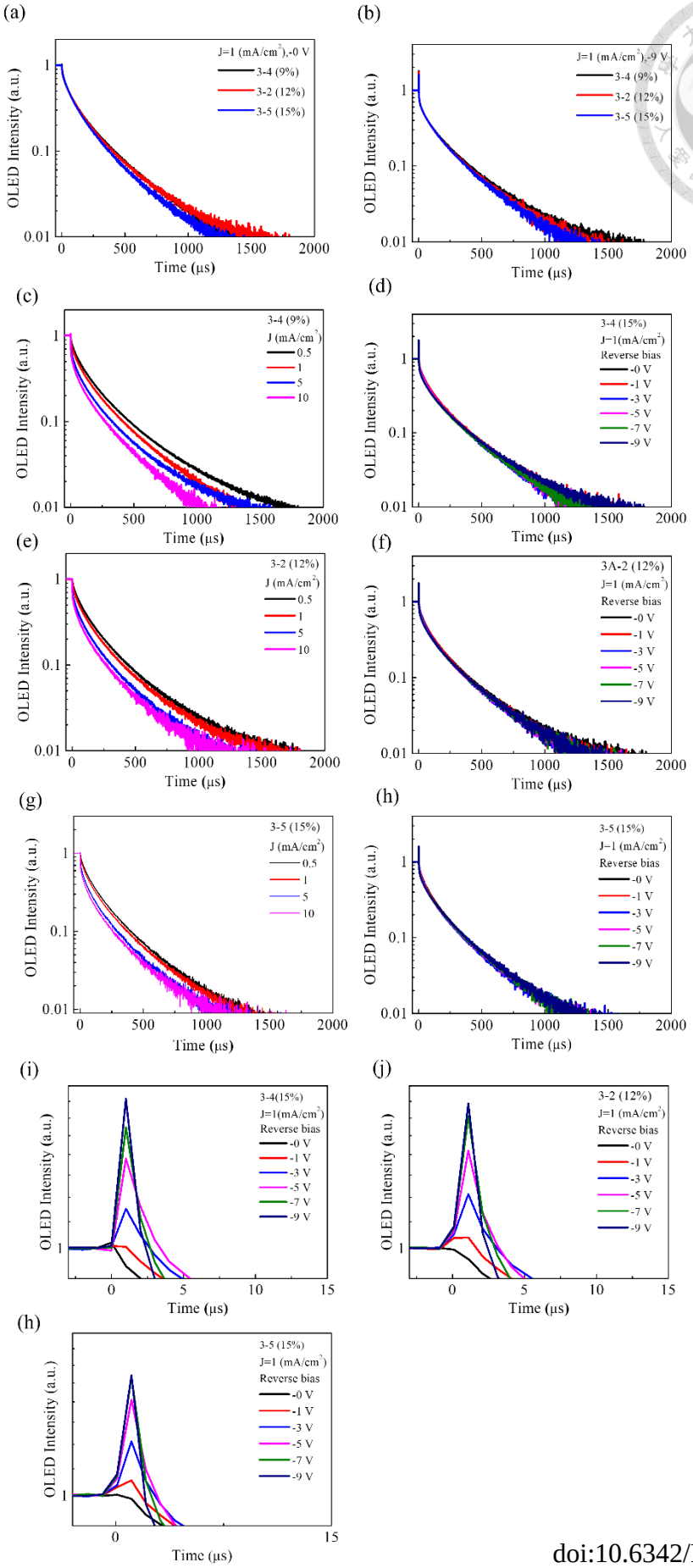

doi:10.6342/NTU202503850

Fig. 3-19 TrEL of devices (a) 3-4, 3-2 and 3-5 with J = 1 mA/cm^2, (b) 3-4, 3-2 and 3-5 with J = 1 mA/cm^2, and switched to -9 V after t > 0 (c) 3-4 with different current densities, (d) 3-4 with different reverse bias after t > 0, (e) 3-2 with different current densities, (f) 3-2 with different reverse bias after t > 0, (g) 3-5 with different current densities, (h) 3-5 with different reverse bias after t > 0, (i) shorter time scale (15 μs) of 3-5with different reverse bias after t > 0, (j) shorter time scale (15 μs) of 3-2 with different reverse bias after t > 0, and (k) shorter time scale (15 μs) of 3-4 with different reverse bias after t > 0.

3.4.3 Optimization of ETL thickness

Then we fixed the different dopant concentrations in this part and adjusted the thickness of the ETL from 50, 55, 60, to 65 nm for obtaining the highest maximum EQE.

Table 3-9 Device structures of OLEDs with different ETL thickness.

Device	HTL	EBL	EML	ETL	EIL/cathode
	TAPC	mCP	*o*-2CbzBz: 12% 4Ac35CzPy	DPPS	LiF/Al
3-6	50	10	30	50	0.8/120
3-2				55	
3-7				60	
3-8				65	

unit: nm

Table 3-10 OLED performances of devices 3-6, 3-2, 3-7, and 3-8.

doi:10.6342/NTU202503850

Device	Voltage[a] (V)	Max. Luminance (cd/m^2)	CE[b] (cd/A)	PE[b] (lm/W)	EQE[b] (%)	CIE[c] (x,y)
3-6 (50 nm)	6.6/3.3	3190	45.5/36.8/16.7	41.8/25.4/7.6	15.5/12.3/5.6	(0.173,0.367)
3-2 (55 nm)	7.8/3.3	2724	53.4/42.7/20.3	48.0/31.2/10.5	21.2/17.1/11.9	(0.185, 0.401)
3-7 (60 nm)	6.9/3.3	3293	50.4/39.3/18.1	45.2/27.0/8.9	18.9/14.8/6.9	(0.182,0.395)
3-8 (65 nm)	7.4/3.2	3036	48.5/36.9/18.5	43.6/24.1/8.7	17.8/13.6/6.9	(0.186,0.412)

[a]at J = 10 mA/cm^2/L= 1 cd/m^2; [b]CE/PE/EQE measured at maximum/100 cd/m^2/1000 cd/m^2; [c]measured at maximum current efficiency.

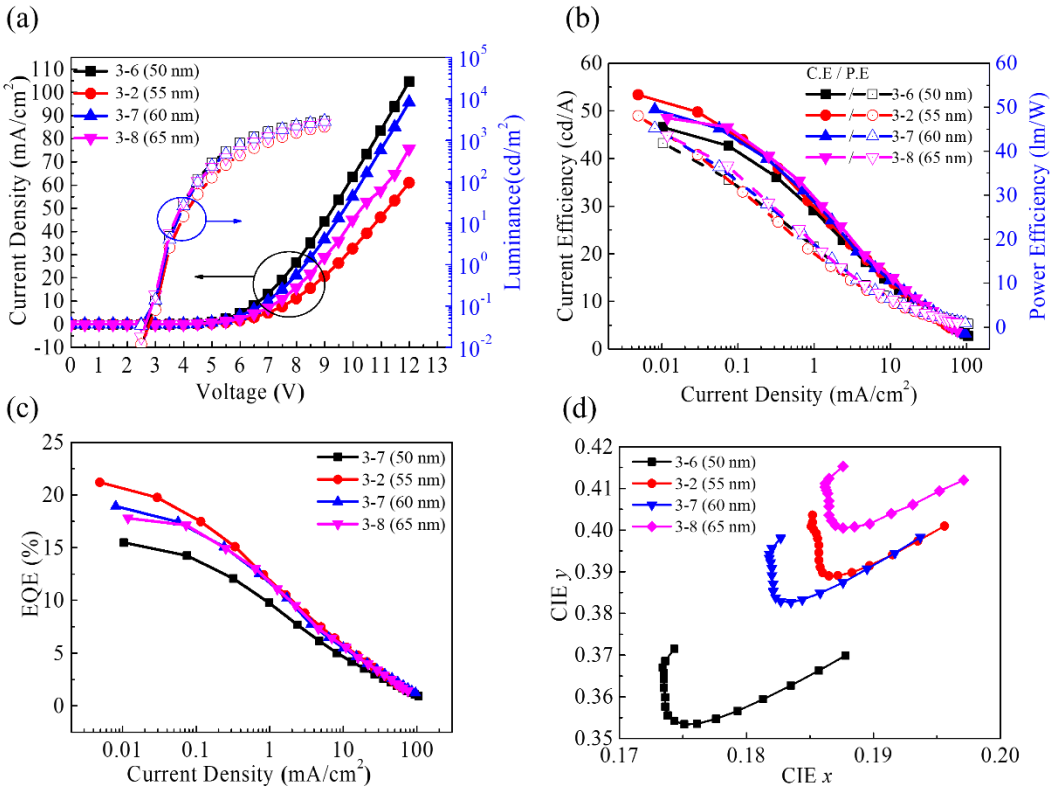

Fig. 3-20 (a) J-L-V curves, (b) current efficiency and power efficiency versus J, (c) EQE versus J, and (d) CIE coordinates at different voltages.

doi:10.6342/NTU202503850

Fig. 3-20 showed the device performances of OLEDs with different ETL thicknesses. Fig. 3-21 (a) showed J-L-V curves. Device 3-6 exhibited the highest current density because of the thinnest ETL. Fig. 3-20 (b), (c), and (d) were current efficiency, power efficiency, and EQE under different current density respectively. Device 3-2 showed the maximum current efficiency, maximum power efficiency, and maximum EQE of 53.4 cd/A, 48.0 lm/W, and 21.2%. Fig. 3-21 showed the EL spectra of devices 3-6, 3-2, 3-7, and 3-8. Fig. 3-22 showed the decay curves of TrEL in 1600 μs window which 4Ac35CzPy exhibited long-delayed emission attributed to their TADF characteristics.

doi:10.6342/NTU202503850

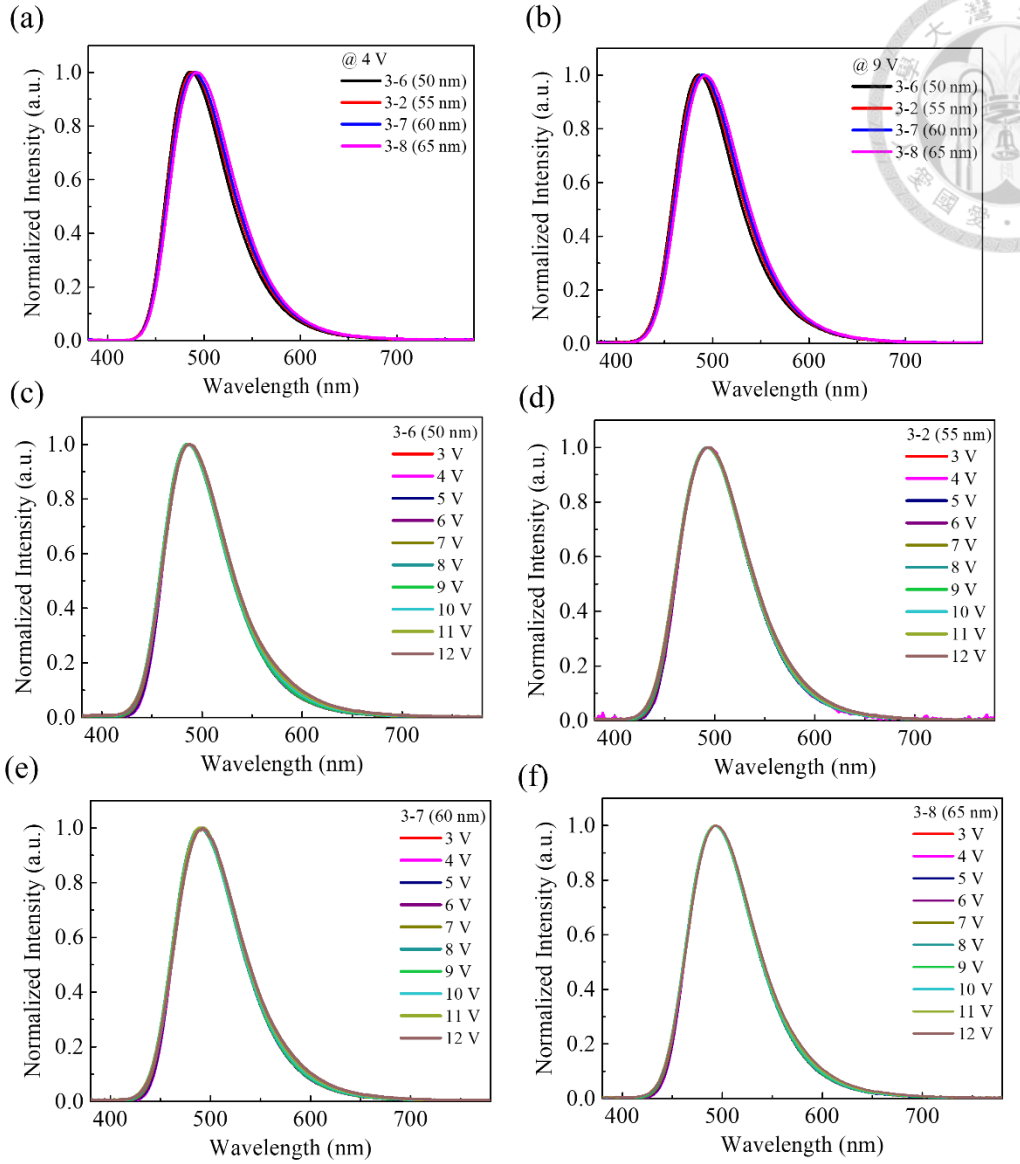

Fig. 3-21 EL spectra of devices (a) 3-6, 3-2, 3-7 and 3-8 with 4 V, (b) 3-6, 3-2, 3-7 and 3-8 with 9 V, (c) 3-6, (d) 3-7, (e) 3-2 and (f) 3-8 with different voltages.

doi:10.6342/NTU202503850

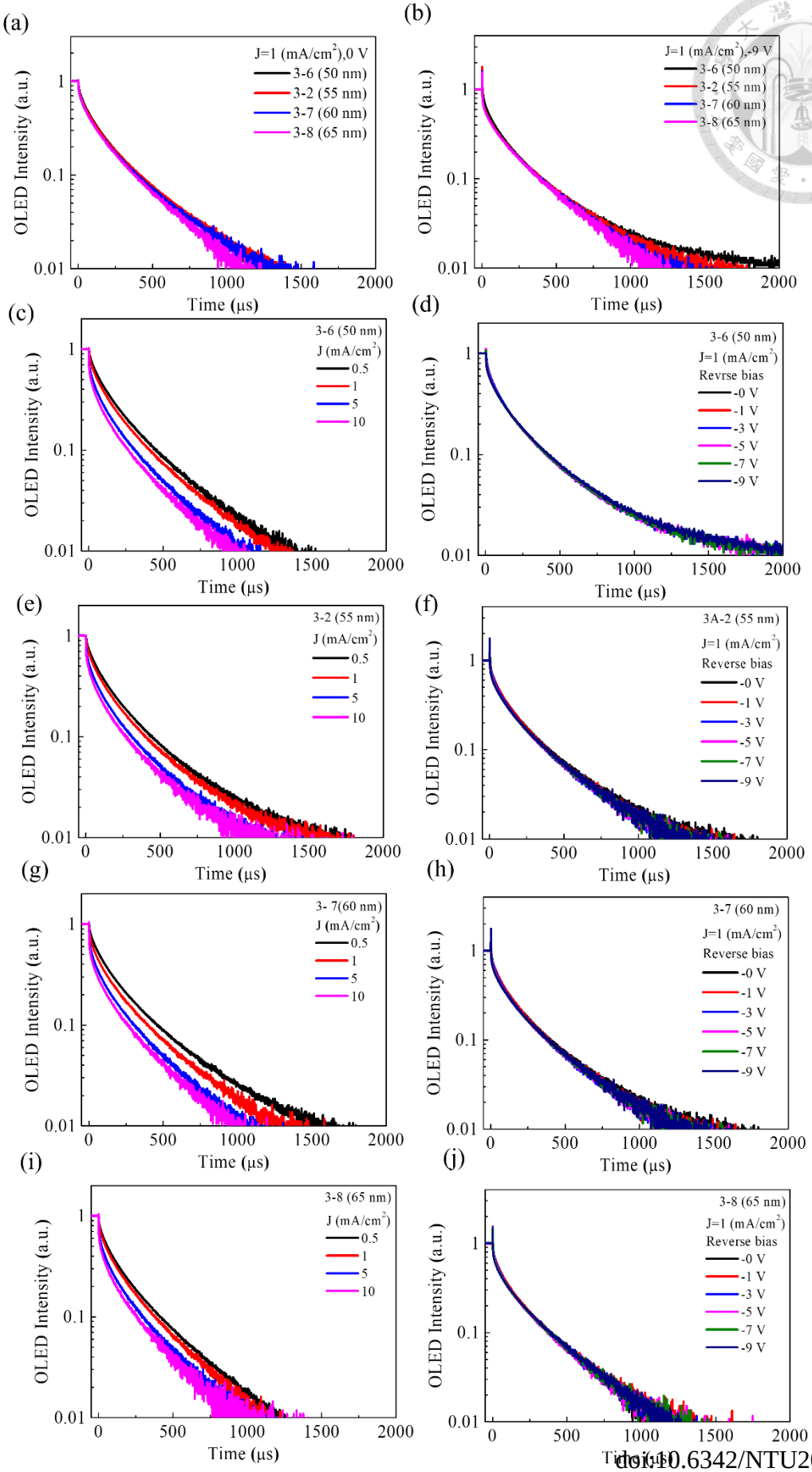

doi:10.6342/NTU202503850

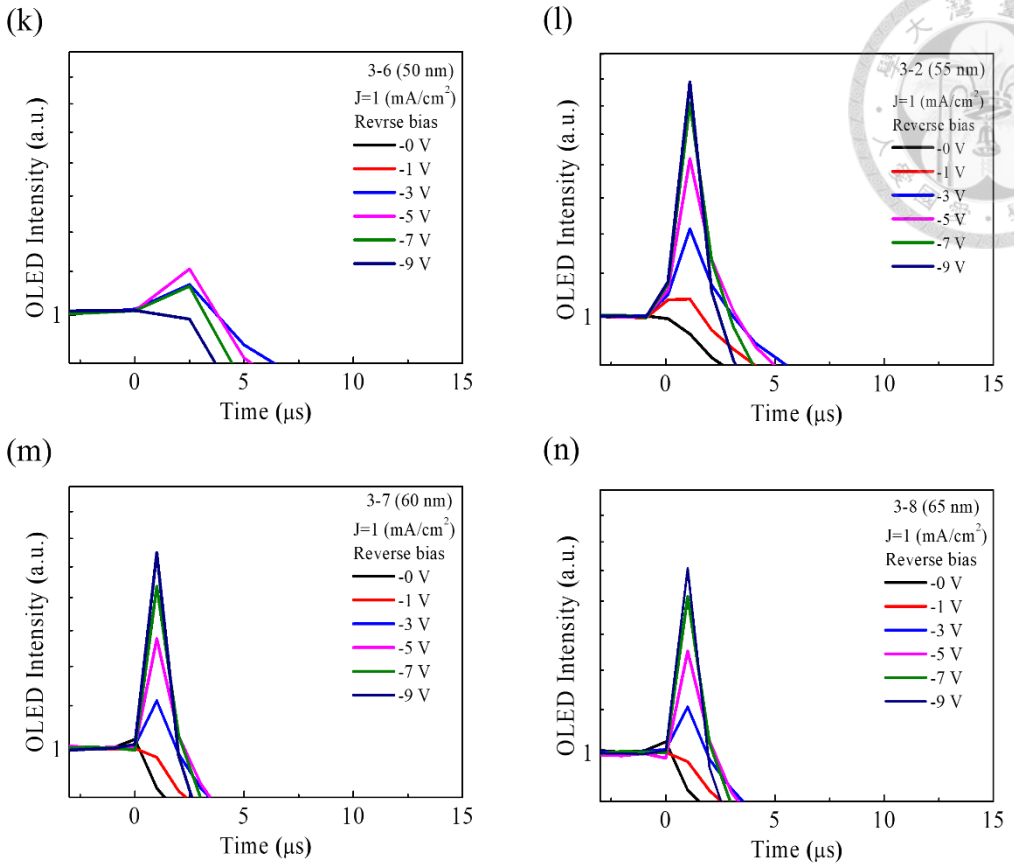

Fig. 3-22 TrEL of devices (a) 3-6, 3-2, 3-7 and 3-8 with J = 1 mA/cm^2, (b) 3-6, 3-2. 3-7 and 3-8 with J = 1 mA/cm^2, and switched to -9 V after t > 0, (c) 3-6 with different current densities, (d) 3-6 with different reverse bias after t > 0, (e) 3-2 with different current densities, (f) 3-2 with different reverse bias after t > 0, (g) 3-7 with different current densities, (h) 3-7 with different reverse bias after t > 0, (i) 3-8 with different current densities, (j) 3-8 with different reverse bias after t > 0, (k) shorter time scale (15 μs) of 3-6 with different reverse bias after t > 0, (l) shorter time scale (15 μs) of 3-2 with different reverse bias after t > 0, (m) shorter time scale (15 μs) of 3-7 with different reverse bias after t > 0, and (n) shorter time scale (15 μs) of 3-8 with different reverse bias after t > 0.

doi:10.6342/NTU202503850

3.4.4 Optimization of EML thickness

Here, we fixed dopant concentration at 12%, thickness of the ETL at 55 nm, and tuned the thickness of EML from 25, 30, to 35 nm. The detailed device structures were shown in Table 3-11.

Table 3-11 Device structures of OLEDs with adjusting the thickness of EML.

Device	HTL	EBL	EML	ETL	EIL/cathode
	TAPC	mCP	*o*-2CbzBz: 12% 4Ac35CzPy	DPPS	LiF/Al
3-9	50	10	25	55	0.8/120
3-2			30		
3-10			35		

unit: nm

Table 3-12 OLED performances of devices 3-9, 3-2, and 3-10.

Device	**Voltage[a] (V)**	**Max. Luminance (cd/m^2)**	**CE[b] (cd/A)**	**PE[b] (lm/W)**	**EQE[b] (%)**	**CIE[c] (x,y)**
3-9 (25 nm)	6.4/3.2	2271	48.9/39.3/16.9	44.1/25.5/7.7	17.4/14.0/6.1	(0.179,0.386)
3-2 (30 nm)	7.8/3.3	2724	53.4/42.7/20.3	48.0/31.2/10.5	21.2/17.1/11.9	(0.185, 0.401)
3-10 (35 nm)	6.9/3.2	3532	50.4/41.3/20.4	45.2/29.1/10.2	19.6/16.2/8.0	(0.179,0.391)

[a]at J = 10 mA/cm^2/L= 1 cd/m^2; [b]CE/PE/EQE measured at maximum/100 cd/m^2/1000 cd/m^2; [c]measured at maximum current efficiency.

doi:10.6342/NTU202503850

Table 3-13 OLED performances of devices 3-9, 3-2, and 3-10.

Device	Voltage[a] (V)	Max. Luminance (cd/m²)	CE[b] (cd/A)	PE[b] (lm/W)	EQE[b] (%)	CIE[c] (x,y)
3-9 (25 nm)	6.4/3.2	2271	48.9/39.3/16.9	44.1/25.5/7.7	17.4/14.0/6.1	(0.179,0.386)
3-2 (30 nm)	7.8/3.3	2724	53.4/42.7/20.3	48.0/31.2/10.5	21.2/17.1/11.9	(0.185, 0.401)
3-10 (35 nm)	6.9/3.2	3532	50.4/41.3/20.4	45.2/29.1/10.2	19.6/16.2/8.0	(0.179,0.391)

[a]at J = 10 mA/cm²/L= 1 cd/m²; [b]CE/PE/EQE measured at maximum/100 cd/m²/1000 cd/m²; [c]measured at maximum current efficiency.

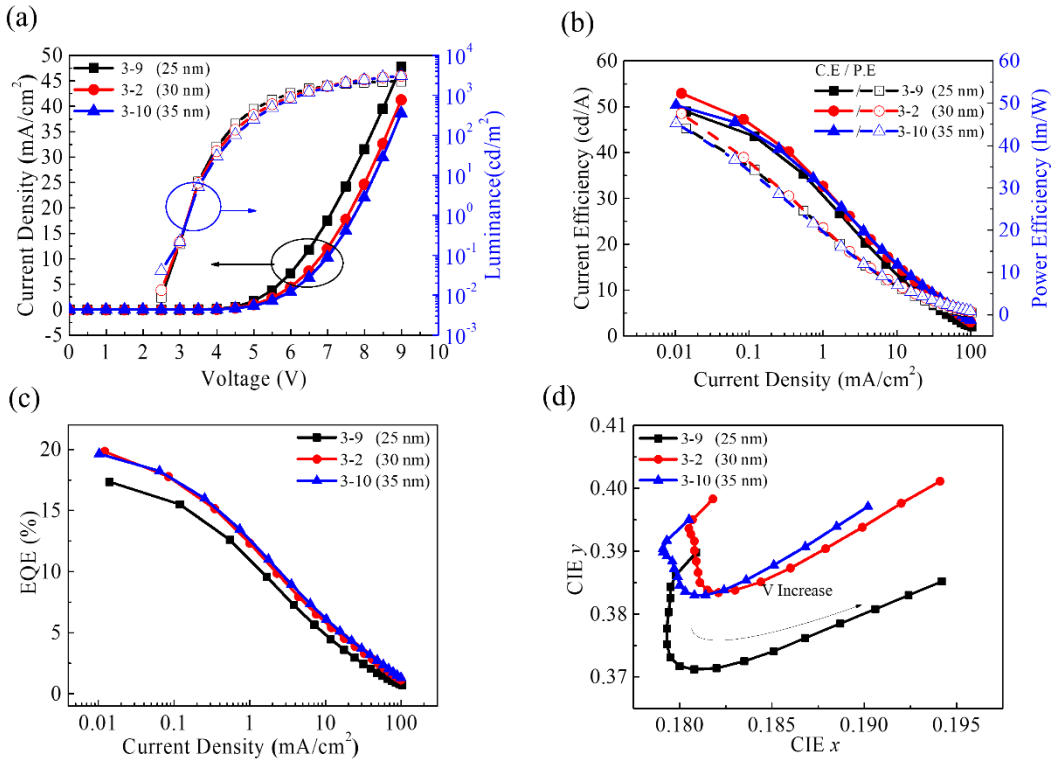

Fig. 3-23 (a) J-L-V curves, (b) current efficiency and power efficiency versus J, (c) EQE versus J, and (d) CIE coordinates at different voltages.

Table 3-12 was device performances. Fig. 3-23 (a) was J-L-V curves, and the current density would be lower as the EML is thicker. Fig. 3-23 (b), (c), and (d) were

doi:10.6342/NTU202503850

current efficiency, power efficiency, and EQE under different current density. Device 3-2 showed the maximum current efficiency, maximum power efficiency, and maximum EQE of 53.4 cd/A, 48.0 lm/W, and 21.2%. Figure (d) shows the CIE coordinates. It can be observed that y-value of the CIE coordinates in devices 3-9 was lower because the EML were relatively thinner. Fig. 3-24 showed the EL spectra of devices 3-9, 3-2, and 3-10, resulting from 4Ac35CzPy emission. Fig. 3-25 showed the decay curves of TrEL which exhibited long-delayed emission attributed to their TADF characteristics.

doi:10.6342/NTU202503850

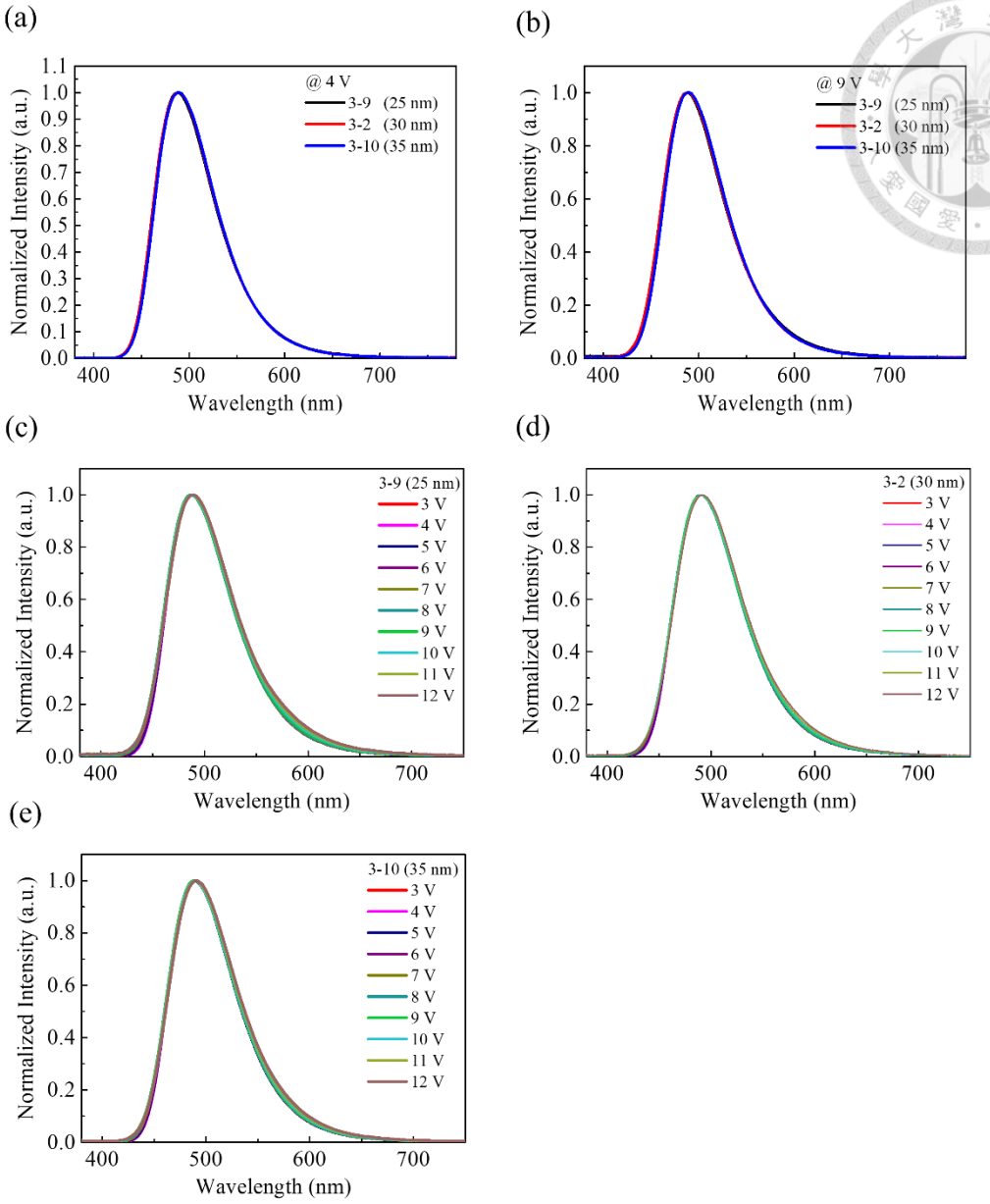

Fig. 3-24 EL spectra of devices (a) 3-9, 3-2, and 3-10 with 4 V, (b) 3-9, 3-2, and 3-10 with 9 V, (c) 3-9, (d) 3-2, and (e) 3-10 with different voltages.

doi:10.6342/NTU202503850

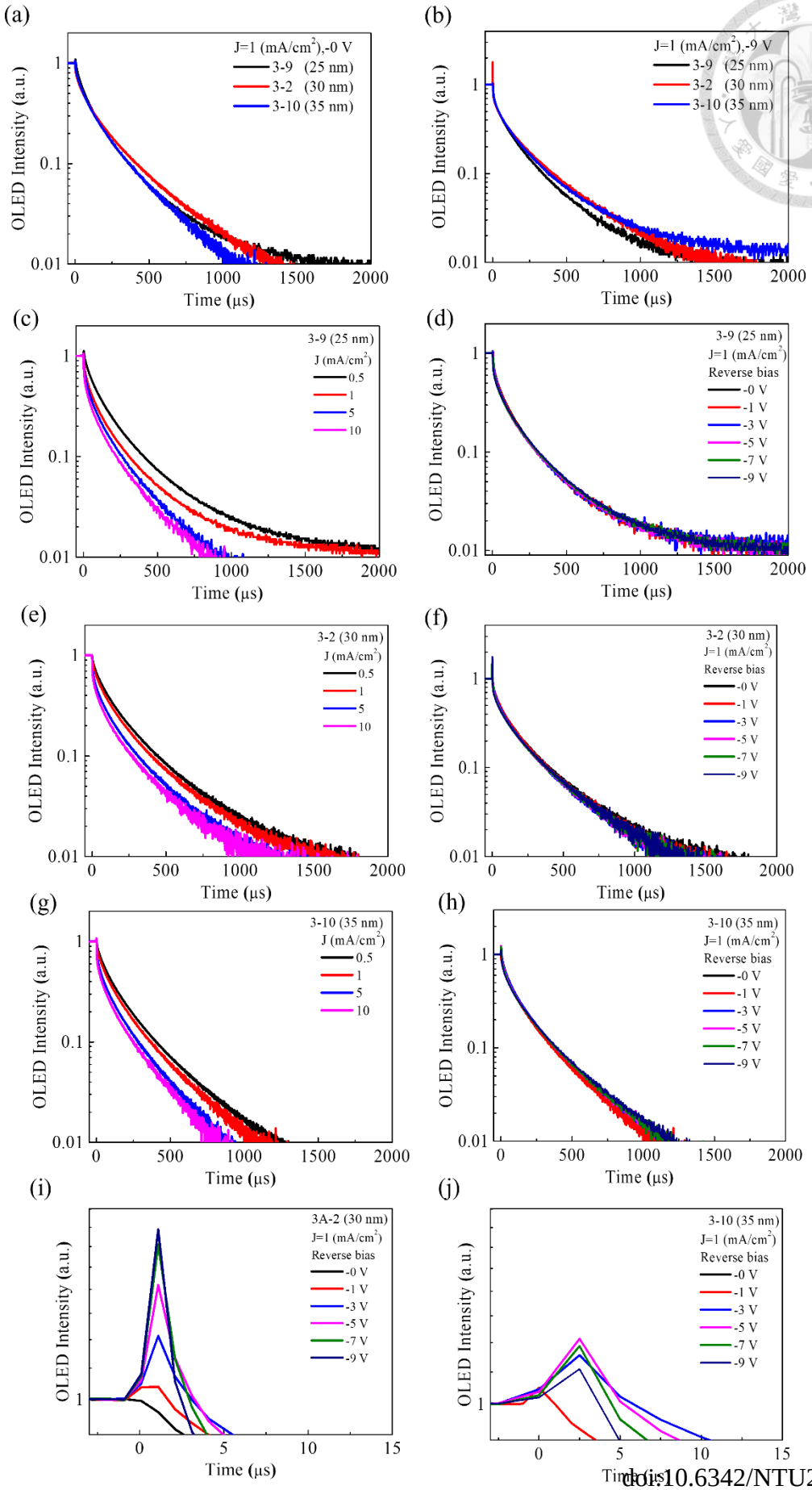

doi:10.6342/NTU202503850

Fig. 3-25 TrEL of (a) 3-9, 3-2, and 3-10 with J = 1 mA/cm^2, (b) 3-9, 3-2, and 3-10 with J = 1 mA/cm^2, and switched to -9 V after t > 0, (c) 3-9 with different current densities, (d) 3-9 with different reverse bias after t > 0, (e) 3-2 with different current densities, (f) 3-2 with different reverse bias after t > 0, (g) 3-10 with different current densities, (h) 3-10 with different reverse bias after t > 0, (i) shorter time scale (15 μs) of 3-2 with different reverse bias after t > 0, and (j) shorter time scale (15 μs) of 3-10 with different reverse bias after t > 0.

3.5 Optimization procedure of TADF OLED with 4Ac25CzPy as the emitter

In this section, we discuss the OLED performances with 4Ac25CzPy as the emitters doped with two hosts, i.e. *o*-2CbzBz and *o*-3CbzBz. The device structures and performances were presented in Table 3-14 and

vvTable 3-15, respectively. To achieve higher EQE, we doped a blue dopant, 4Ac25CzPy, into *o*-2CbzBz and *o*-3CbzBz hosts as the EML. The energy diagram of OLEDs shown in Fig. 3-26. Table 3-14 showed device structures and performance were summarized in

vvTable 3-15.

doi:10.6342/NTU202503850

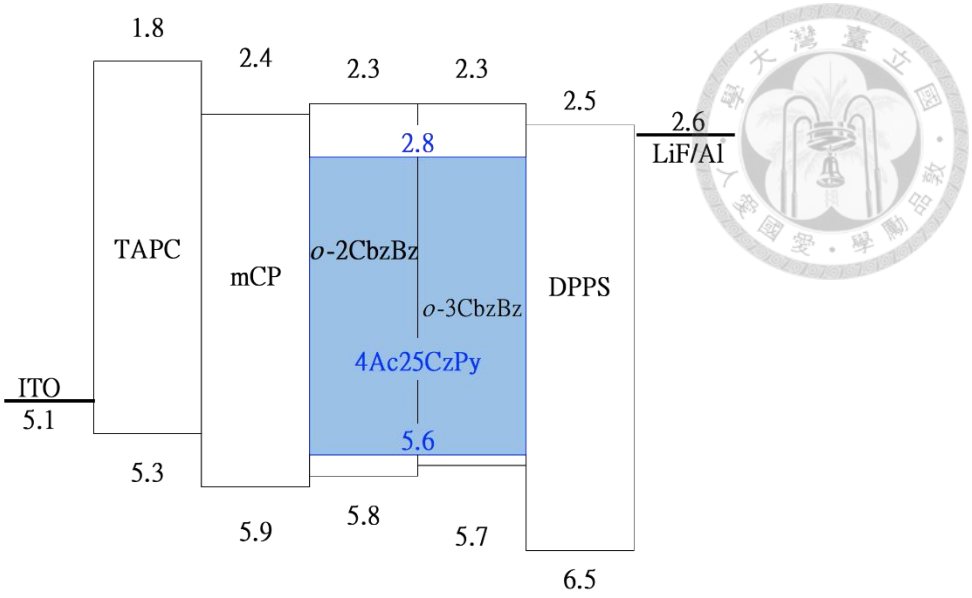

Fig. 3-26 Energy diagram of OLEDs with 4Ac25CzPy-doped in *o*-2CbzBz and *o*-3CbzBz as the EML.

Table 3-14 Device structures of OLEDs with *o*-2CbzBz and *o*-3CbzBz.

Device	HTL	EBL	EML	ETL	EIL/cathode
	TAPC	*m*CP	Host: 12% 4Ac25CzPy (30 nm)	DPPS	LiF/Al
3-1	50	10	*o*-2CbzBz	55	0.8/120
3-11			*o*-3CbzBz		

unit: nm

vvTable 3-15 OLED performances of devices (a) 3-1 and (b) 3-11

Device	**Voltage[a] (V)**	**Max. Luminance (cd/m^2)**	**CE[b] (cd/A)**	**PE[b] (lm/W)**	**EQE[b] (%)**	**CIE[c] (x,y)**
3-1 (*o*-2CbzBz)	6.8/3.3	2635	31.5/27.6/16.6	28.3/20.7/8.7	12.4/10.9/6.6	(0.156, 0.396)
3-11 (*o*-3CbzBz)	6.0/3.2	2548	21.5/20.8/12.1	16.9/15.9/.6.5	9.0/8.9/5.3	(0.156, 0.396)

[a]at J = 10 mA/cm^2/L= 1 cd/m^2; [b]CE/PE/EQE measured at maximum/100 cd/m^2/1000 cd/m^2; [c]measured at maximum current

doi:10.6342/NTU202503850

efficiency.

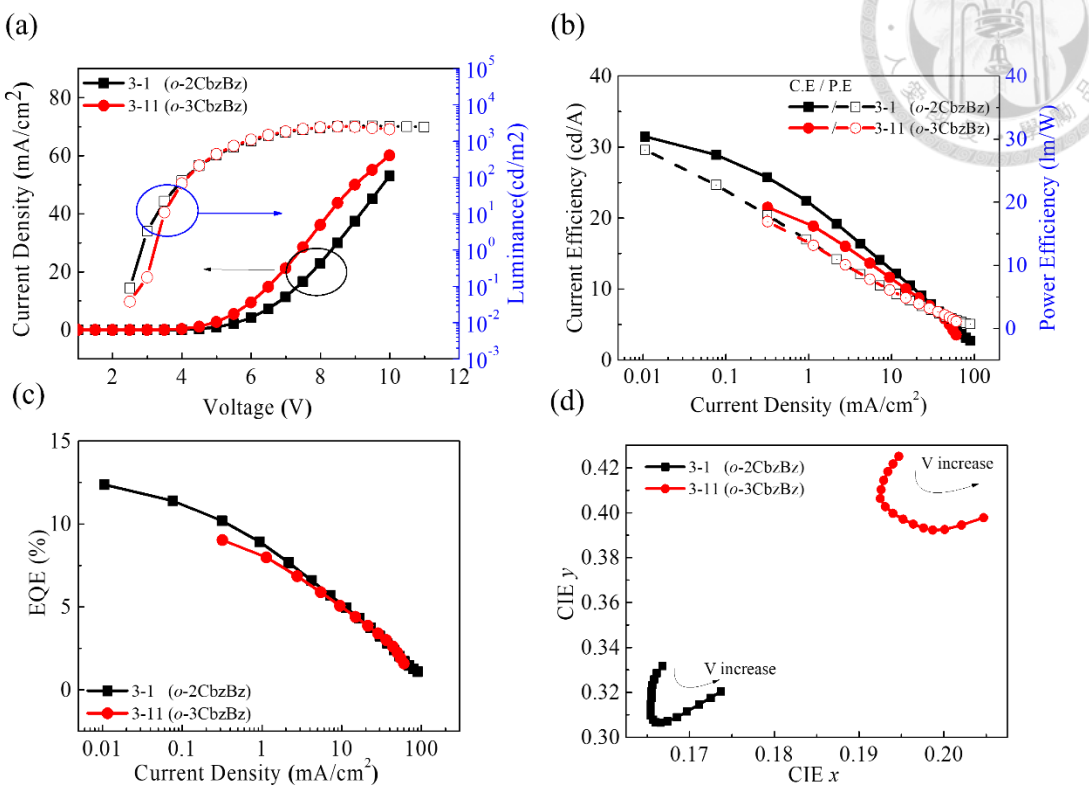

Fig. 3-27 (a) J-L-V curves, (b) current efficiency and power efficiency versus J, (c) EQE versus J, and (d) CIE coordinates at different voltages.

Fig. 3-27 showed OLED performances with *o*-2CbzBz and *o*-3Cbzbz doped 4Ac25CzPy as the EML. In Fig. 3-27 (a), devices 3-1 showed the J-L-V curve. Under the same driving voltage device 3-11 exhibited higher current density than device 3-1. Fig. 3-27 (b), (c), and (d) were current efficiency, power efficiency, and EQE under different current densities. Devices 3-1 and 3-11 showed the maximum current efficiency, maximum power efficiency, maximum EQE of 31.5 cd/A and 21.5 cd/A, 28.3 lm/W and 16.9 lm/W, and 12.4% and 9.0%, respectively. Fig. 3-28 was the EL spectra of devices 3-1 and 3-11. Both showed 4Ac25CzPy emission, which indicated that energy transferred successfully from host to dopant. Fig. 3-29 was the TrEL

doi:10.6342/NTU202503850

measurement of devices 3-1 and 3-11. Delayed emission was observed from both OLEDs.

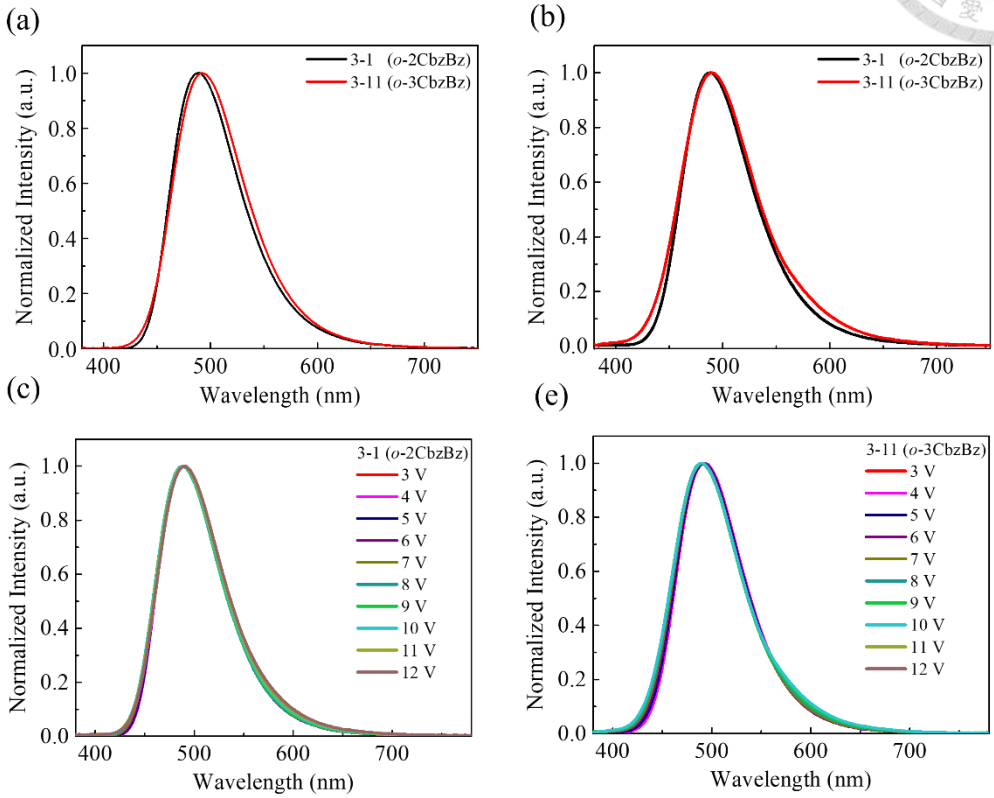

Fig. 3-28 EL spectra of devices (a) 3-1 and 3-11 with 4 V, (b) 3-1 and 3-11 with 9 V, (c) 3-1, and (d) 3-11 with different voltages.

doi:10.6342/NTU202503850

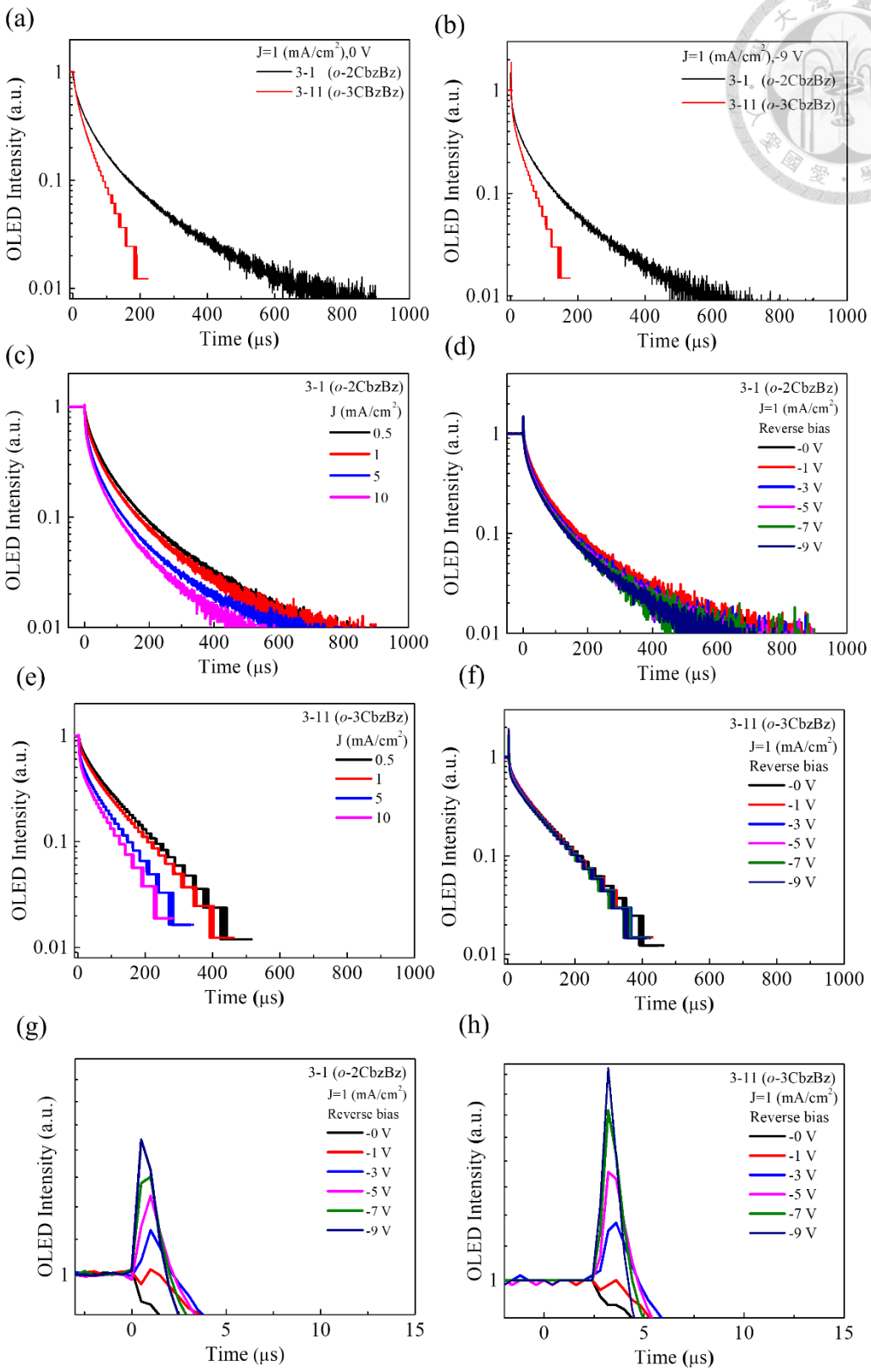

Fig. 3-29 TrEL of (a) 3-1 and 3-11 with J = 1 mA/cm^2, (b) 3-1 and 3-11 with J = 1 mA/cm^2, and switched to -9 V after t > 0, (c) 3-1 with different current densities, (d) 3-

doi:10.6342/NTU202503850

1 with different reverse bias after t > 0, (e) 3-11 with different current densities, (f) 3-11 with different reverse bias after t > 0, (g) shorter time scale (15 μs) of 3-1 with different reverse bias after t > 0, and (h) shorter time scale (15 μs) of 3-11 with different reverse bias after t > 0.

3.6 References

[1] Li, Y.Z., Liang, H.C., Chen, C.H., Chiu, C.H., Lin, B.Y., Tan, J.A., Lee, J.H., Chiu, T.L., Leung, M.K., Thermally activated delayed fluorescence materials for efficient OLEDs, *J. Mater. Chem. C* 11 (2023) 14395–14403.

[2] Chen, C.H., Ding, W.C., Lin, B.Y., Huang, J.J., Leung, M.K., Lee, J.H., Chiu, T.L., High-efficiency blue OLEDs based on TADF emitters, *Adv. Optical Mater.* 9 (2021) 2100857.

Chapter 4 High-efficiency blue TADF OLED with 4Ac26CzBz as the host

doi:10.6342/NTU202503850

material

4.1 Introduction

In this chapter, we demonstrated blue organic light-emitting diodes (OLEDs) based on an acridine-carbazole-benzimidazole material, serving as a bipolar host. This material was synthesized by Prof. Man-kit Leung's group in the Department of Chemistry at National Taiwan University. The resulting compound was 10-(3,5-di(9H-carbazol-9-yl)-4-(1-phenyl-1H-benzo[d]imidazol-2-yl)phenyl)-9,9-dimethyl-9,10-dihydroacridine (4Ac26CzBz) [1]. By doping a thermally activated delayed fluorescence (TADF) emitter, 2,3,5,6-tetrakis(3,6-di-tert-butyl-9H-carbazol-9-yl)benzonitrile (4TCzBN) [2], into the 4Ac26CzBz host, the OLEDs achieved a maximum external quantum efficiency (EQE) of 35.8% and a low lit-on voltage at luminance of 1 cd/m^2 was 2.9 V. These outstanding performances were attributed to the bipolar carrier transport characteristics, well-aligned highest occupied molecular orbital (HOMO) and lowest unoccupied molecular orbital (LUMO) energy levels for carrier injection, relatively high photoluminescence quantum yield (PLQY), and a high degree of horizontal orientation of the emission dipoles.

4.2 Photophysical properties of 4Ac26CzBz derivative

This section provides an overview of photophysical properties of 4Ac26CzBz

doi:10.6342/NTU202503850

with molecular structure shown in Fig. 4-1

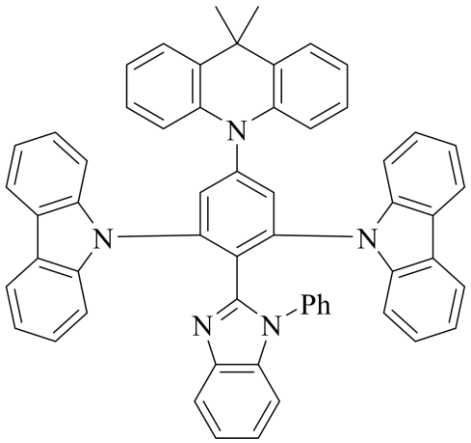

Fig. 4-1 Molecular structure of 4Ac26CzBz.

Table 4-1 summarized the photophysical properties of the compound, while Fig. 4-2 (a) and (b) presented the absorption and photoluminescence (PL) spectra of the material in solution and in neat film, respectively. The PL spectra of the solution revealed an emission peak at 467 nm. Fig. 4-3 displayed the photoelectron spectroscopy results obtained using a Riken AC2 photoelectron spectrometer to determine the HOMO energy level. The optical band gap was estimated from the onset wavelength of the absorption spectra in Fig. 4-2, and calculated using the following equation.

$$E_g\ (eV) = 1240 / \lambda_{onset}^{Abs}\ (nm) \quad (1)$$

where E_g and λ_{onset}^{Abs} represented the onset wavelength of the absorption spectra.

doi:10.6342/NTU202503850

Therefore, the LUMO was obtained from the optical band gap and HOMO level, which was summarized in Table 4-1. About transient photoluminescence (TrPL) and PLQY measurement, this host material was further compared with 9,9'-(2-(1-phenyl-1H-benzo[d]imidazol-2-yl)-1,3-phenylene)bis(9H-carbazole) (*o*-2CbzBz) which has been recognized as a suitable candidate for OLED applications. Photophysical measurements of 4Ac26CzBz and o-2CbzBz-doped film shown a larger knr,T leads to rapid dissipation of T1 excitons. Consequently, τd is shortened, the contribution of delayed emission decreases, and the TrPL decay tail becomes less pronounced, as revealed by the TrPL results shown in Fig. 3-4 TrPL measurement of 4Ac25CzPy and 4Ac35CzPy in neat film and doped film (12% in *o*-2CbzBz) with (a) 40 ns and (b) 400 μs window.and the performance was summarized in Table 4-2. The charge transport characteristics of 4Ac26CzBz were investigated through current density-voltage (J-V) measurements as shown in Fig. 4-7 (a). Electron and hole mobilities (μ_e and μ_h) were extracted using the trap-free Mott-Gurney law and trap-corrected Poole-Frenkel model in Fig. 4-7 (b) [3,4]. At electric fields of 0.7 and 2.5 MV/cm, 4Ac26CzBz exhibited μ_h = 4.11 × 10^{-5} cm^2/Vs and μ_e = 6.3 × 10^{-6} cm^2/Vs, respectively. In an OLED, EQE can be obtained as,

$$EQE = \gamma \times \eta_{PL} \times EUE \times \eta_{out} \quad (2)$$

where γ was the carrier recombination efficiency, which was supposed to be 100% in ideal case. η_{PL} was PLQY which was 98.6% for 4Ac26CzBz. *EUE* was the exciton utilization efficiency which was assumed to be 100%. The last one factor to influence

doi:10.6342/NTU202503850

EQE was η_{out}, which meant light outcoupling efficiency.

The transition dipole orientation of 4Ac26CzBz was investigated using grazing-incidence wide-angle X-ray scattering (GIWAXS). As shown in Fig. 4-8(a), the two-dimensional (2D) GIWAXS pattern exhibited distinct anisotropy, indicating preferential molecular orientation in the neat film. A pronounced π-π stacking feature appears in the out-of-plane (qz) direction with a d-spacing of 9.6 Å, suggesting well-ordered molecular packing. To quantitatively analyze the molecular orientation, we calculated the order parameter of GIWAXS (S_{GIWAXS}) by integrating the scattering intensity at various azimuthal angles (χ), following established methodology. The orientation parameters were determined using Eqs. 3 and 4, providing a quantitative measure of the molecular alignment. This analysis confirmed the anisotropic nature of the 4Ac26CzBz thin film, which was critical for understanding its optoelectronic properties.

$$S_{Giwaxs}=\frac{1}{2}(3<cos^2\chi>-1) \quad (3)$$

$$<cos^2\chi>=\frac{\int_0^{90} I(\chi)(cos^2\chi)(\sin\chi)\,d\chi}{\int_0^{90} I(\chi)(\sin\chi)\,d\chi} \quad (4)$$

doi:10.6342/NTU202503850

Table 4-1 Photophysical properties of 4Ac26CzBz and 4TCzBN.

Compound	λ_{max} [a] (nm)	λ_{onset} Abs [a] (nm)	E_g [a, b] (eV)	λ_{PL} [a] (nm)	E_S [c] (eV)	E_T [d] (eV)	ΔE_{ST} (eV)	HOMO [e] (eV)	LUMO [e] (eV)
4Ac26CzBz	258,287,333/296,335	392/403	2.81/3.07	467/440	3.34	2.86	0.35	-5.53/-5.42	-2.72/-2.35
4TCzBN	250,294,338/ -	433/ -	2.73/ -	456/ -	2.86	2.62	0.24	-5.48/ -	-2.74/ -

[a]Measured in $1x10^{-5}$ M 2-methyl THF solution/ 60-nm thickness in the film state.; [b] E_g =1240.8/ λ_{onset} of absorption (eV) ; [c]S_1 =1240.8/λ (cross point wavelength of absorption and fluorescence spectra) (eV), [d]T_1 =1240.8/ λ_{onset} of LTPH (eV) ; [e] Obtained with CV $1x10^{-5}$ M 2-methyl THF solution and film measured from AC2 and 60-nm thin-film optical gap, $E_{LUMO} = E_{HOMO} - E_g$; [f]Measured in $1x10^{-5}$ M 2-methyl THF solution, neat film and 12 % emitter doped in *o*-2CbzBz..

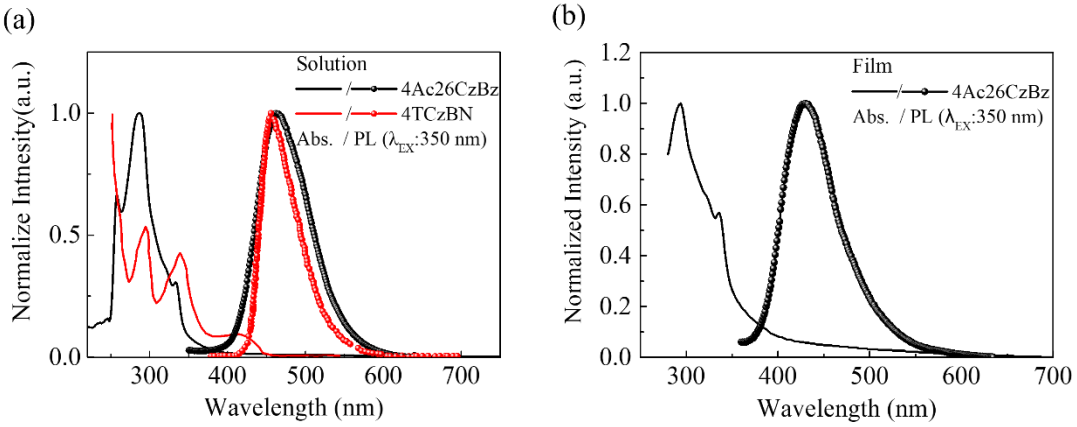

Fig. 4-2 (a) Absorption and PL spectra of 4Ac26CzBz in 1 * 10^{-5} M 2-methyl THF solution and 4TCzBN in toluene solution., and (b) absorption and PL spectra of 4Ac26CzBz in neat film.

doi:10.6342/NTU202503850

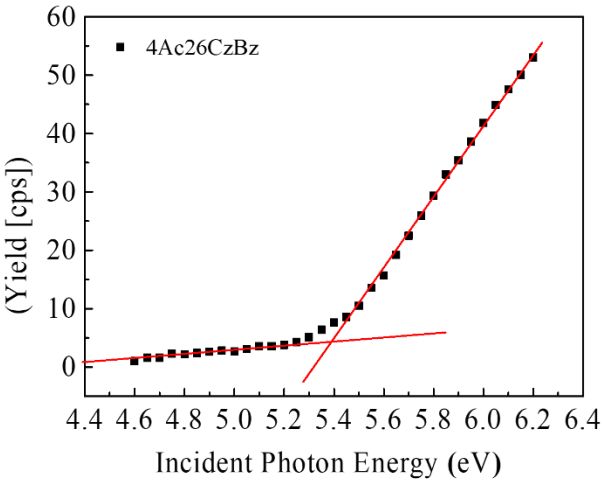

Fig. 4-3 AC2 measurements of 4Ac26CzBz.

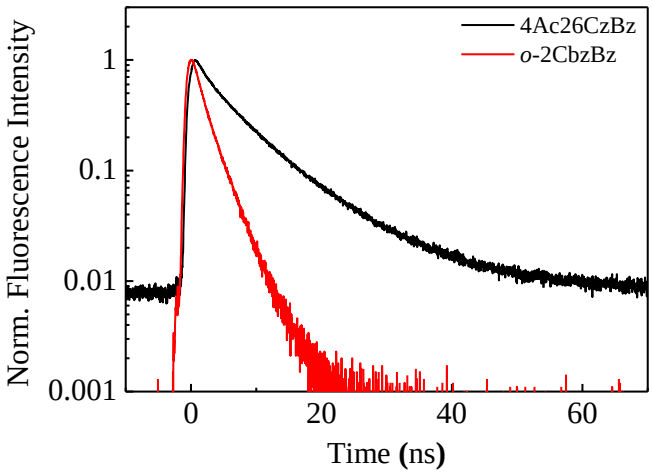

Fig. 4-4 TrPL measurement of 4Ac26CzBz and *o*-2CbzBz in 70 ns window.

doi:10.6342/NTU202503850

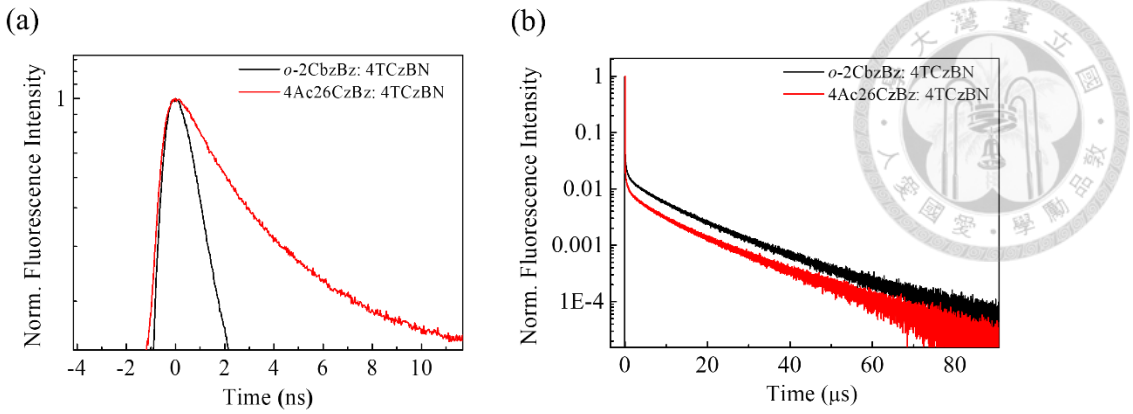

Fig. 4-5 TrPL measurement of 4TCzBN doped in *o*-2CbzBz and 4Ac26CzBz (40% in *o*-2CbzBz and 4Ac26CzBz) with (a) 12 ns and (b) 100 μs window.

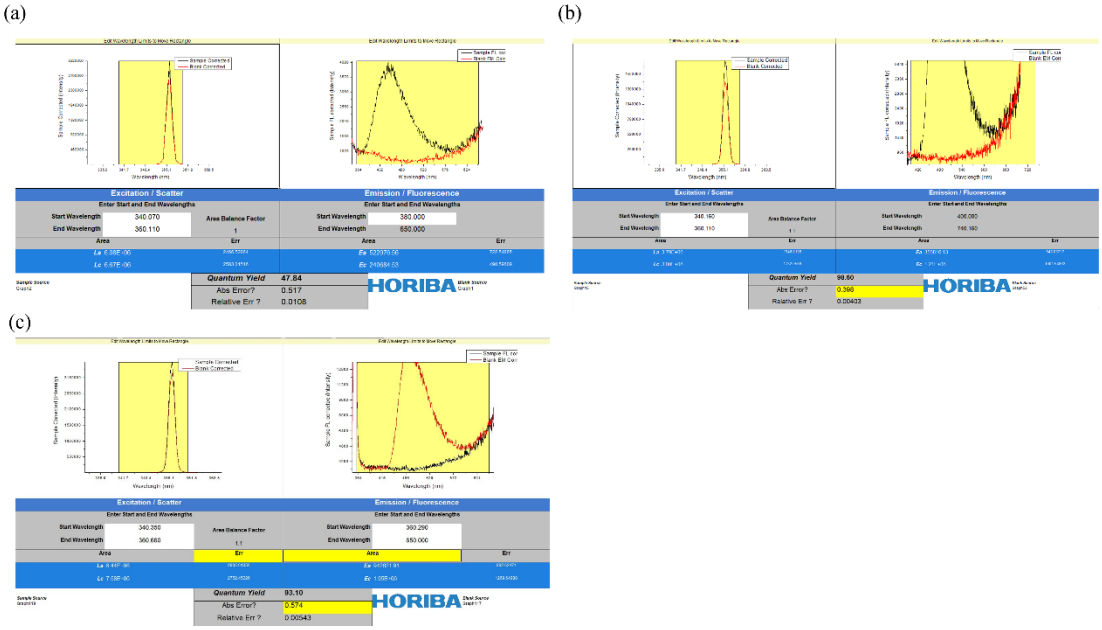

Fig. 4-6 PLQY of thin film (a) 4Ac26CzBz neat film, (b) 40% 4TCzBN doped in 4Ac26CzBz, and (c) 40 % 4TCzBN doped in *o*-2CbzBz.

Table 4-2 Photophysical measurements of 4Ac26CzBz and *o*-2CbzBz-doped film.

compound	$\Phi_{total}/\Phi_{prompt}/\Phi_{delay}$[a] [%]	τ_p[d] [ns]	τ_d[b] [μs]	$k_{r,s}$[c] [* 10^7 s^{-1}]	$k_{nr,T}$[c] [* 10^3 s^{-1}]	k_{ISC}[d] [* 10^7 s^{-1}]	k_{rISC}[d] [* 10^4 s^{-1}]
4Ac26CzBz	98.6/34.9/63.6	2.5	11.7	2.2	74.9	5.9	3.0
o-2CbzBz	93.1/26.3/66.2	1.2	11.7	1.4	78.7	2.6	2.4

[a] Photoluminescence quantum yield of overall, prompt and delayed fluorescence. [b] Exciton lifetime of prompt and delayed fluorescence obtained from TrPL. [c] Rate constant of radiative decay from S_1 to S_0 ($k_{r,s}$) and nonradiative decay of T_1 to S_0 ($k_{nr,T}$). [d] Rate constant of intersystem crossing (ISC) and reverse intersystem crossing (rISC).

doi:10.6342/NTU202503850

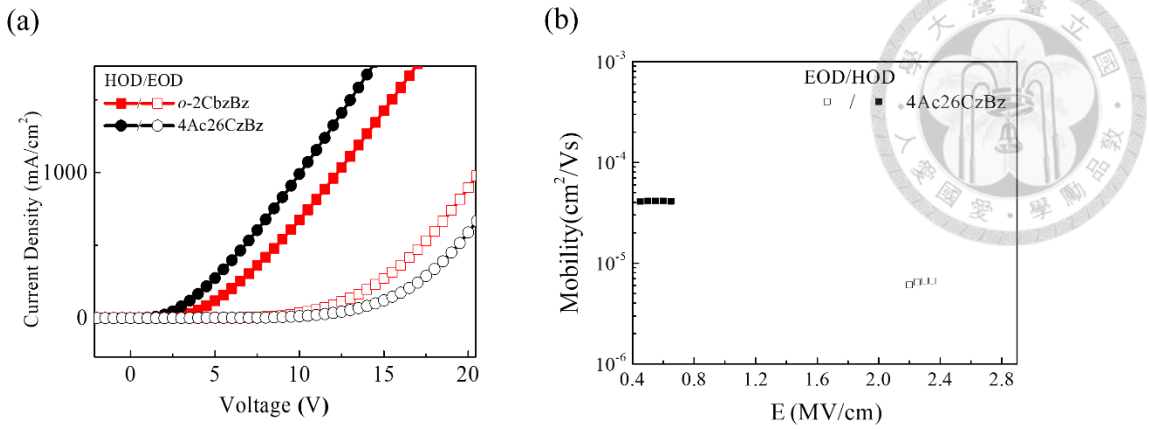

Fig. 4-7 (a) J−V for EOD and HOD of 4Ac26CzBz and *o*-2CbzBz, and (b) hole and electron mobilities as a function of the electric field of 4Ac26CzBz.

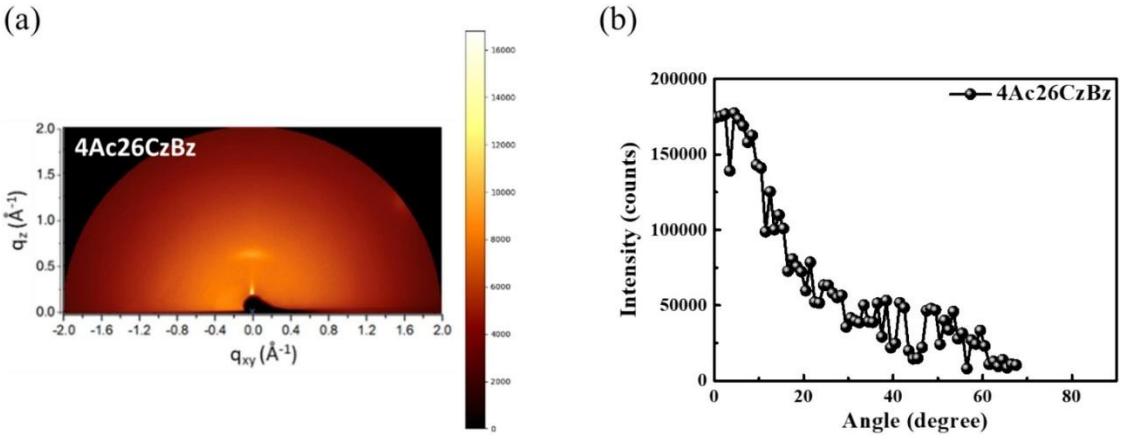

Fig. 4-8 (a) Two-dimensional GIWAXS scattering patterns of the neat film of 4Ac26CzBz (100 nm) and (b) GIWAXS signal at different azimuthal angles.

4.3 High-efficiency blue TADF-OLEDs

In our OLEDs, we employed 4,4'-Cyclohexylidenebis[N, N-bis(4-methylphenyl)benzenamine] (TAPC), N,N'-dicarbazolyl-3,5-benzene (mCP), and Diphenylbis(4-(pyridin-3-yl)phenyl)silane (DPPS) as the hole transporting layer (HTL), electron blocking layer (EBL), and electron transporting layer (ETL), respectively. The molecular structures of TAPC, mCP, and DPPS, along with the device energy diagram, were shown in Fig. 4-9 and

doi:10.6342/NTU202503850

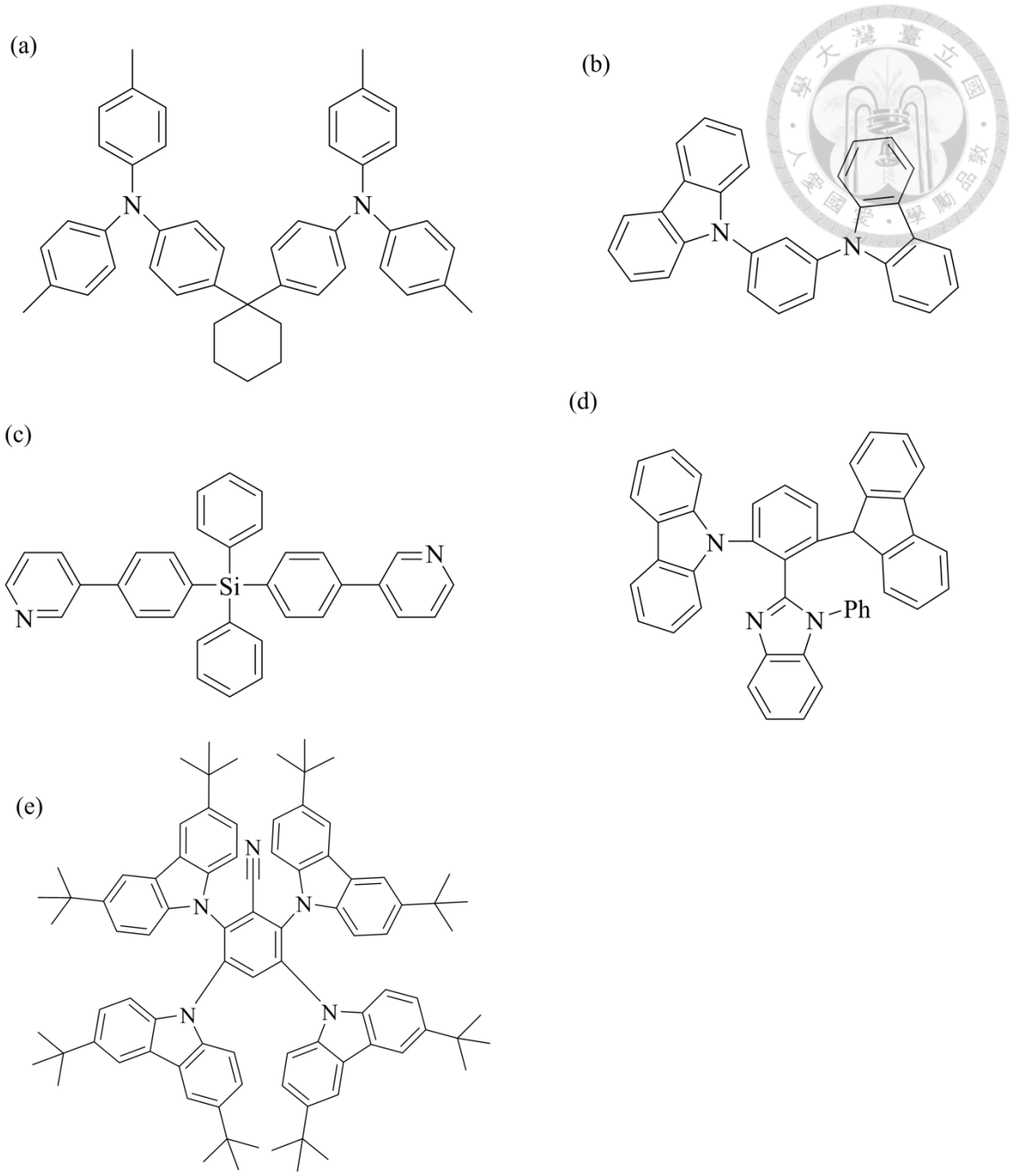

Fig. 4-10. The energy diagram of the OLEDs was shown in Fig. 4-9, with two hosts, i.e. *o*-2CbzBz and 4Ac26CbzBz, doped with 4TCzBN emitter. Table 4-3 presented the device structures, and their performances were summarized in Table 4-4.

doi:10.6342/NTU202503850

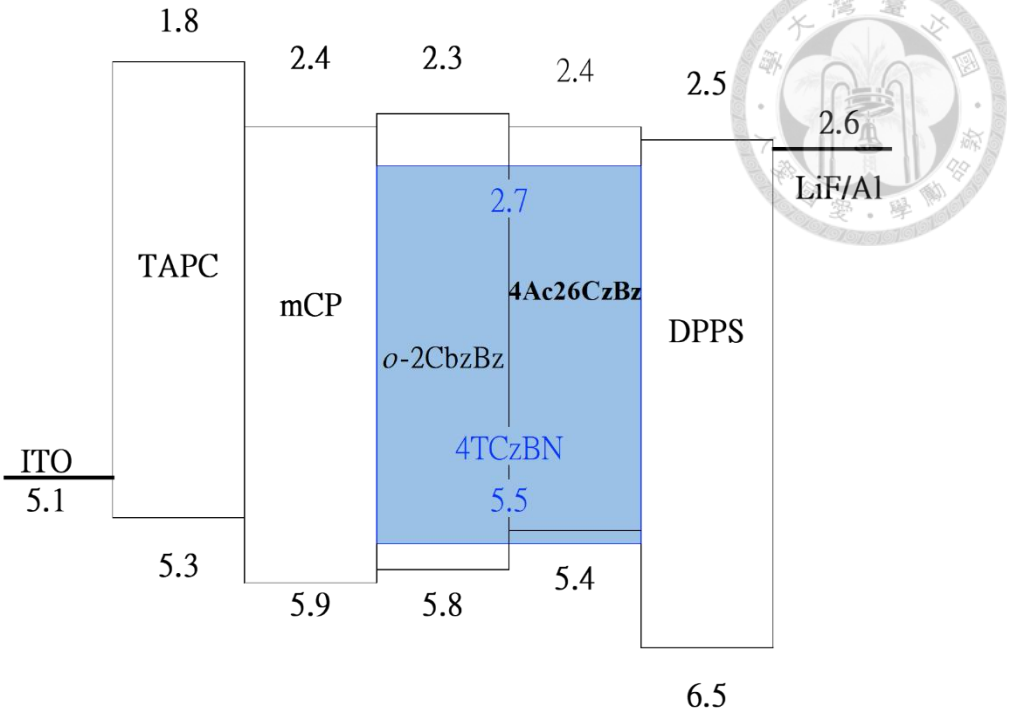

Fig. 4-9 Energy diagram of OLEDs with 4TCzBN-doped in *o*-2CbzBz and 4Ac26CzBz as the EML.

doi:10.6342/NTU202503850

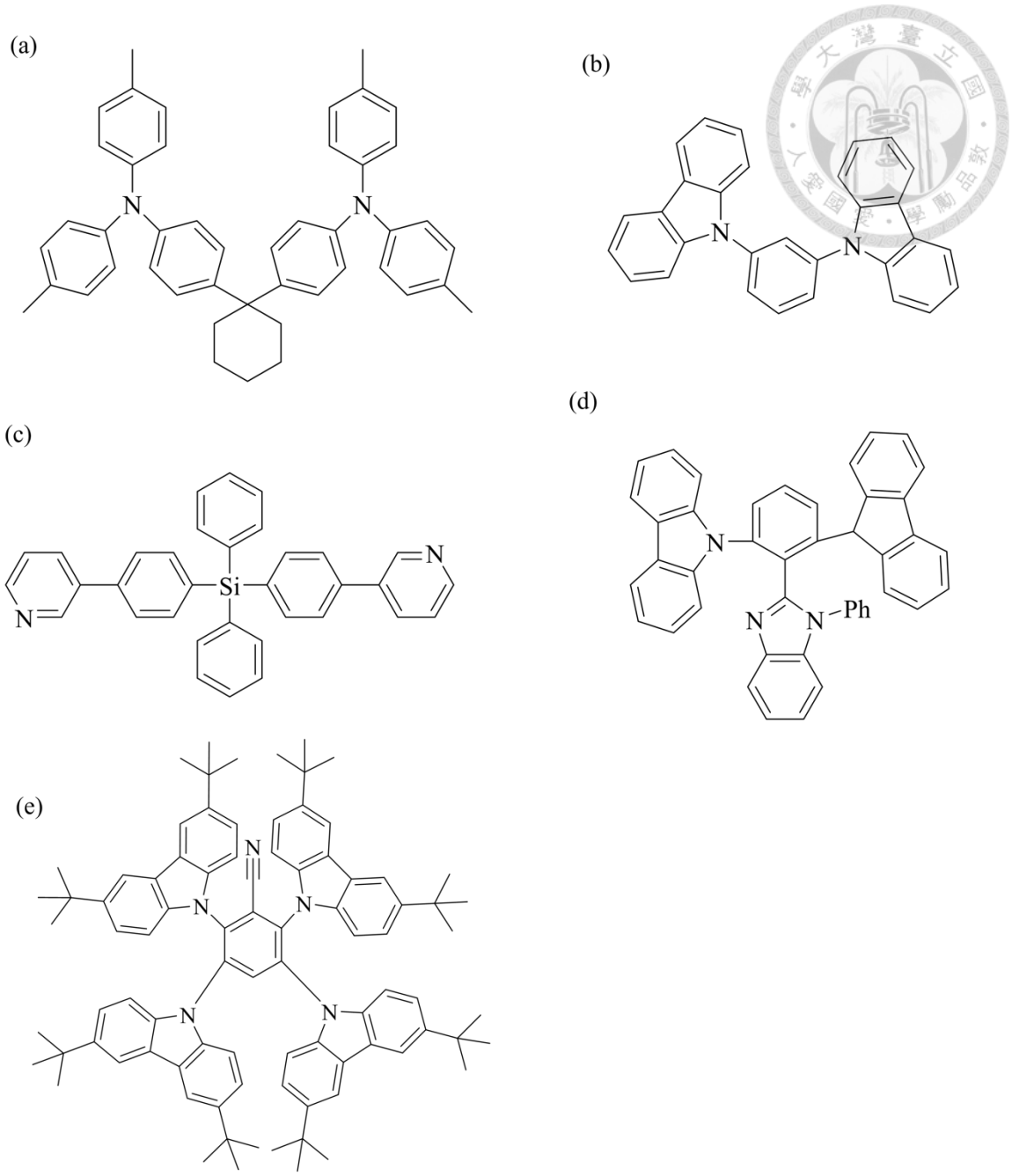

Fig. 4-10 Molecular structures of (a) TAPC, (b) mCP, (c) DPPS, (d) *o*-2CbzBz, and (e) 4TCzBN.

Table 4-3 Optimized device structure of TADF OLED with *o*-2CbzBz and 4Ac26CzBz hosts.

Device	HTL	EBL	EML	ETL	EIL/cathode
	TAPC	mCP	40% 4TCzBN	DPPS	LiF/Al

doi:10.6342/NTU202503850

			(30 nm)		
4-1 4-2	50	10	4Ac26CzBz *o*-2CbzBz	55	0.8/120

unit: nm

Table 4-4 OLED performances of devices 4-1 and 4-2.

Device	**Voltage[a] (V)**	**Max. Luminance (cd/m²)**	**CE[b] (cd/A)**	**PE[b] (lm/W)**	**EQE[b] (%)**	**CIE[c] (x,y)**
4-1 (***o***-2CbzBz)	6.4/3.0	7255	59.4/46.8/40.5	55.0/41.8/26.0	32.5/31.2/27.0	(0.144, 0.233)
4-2 (4Ac26Czbz)	6.4/2.9	4756	59.8/56.8/47.2	62.8/47.6/27.1	35.8/34.4/28.6	(0.143, 0.249)

[a]at J = 10 mA/cm²/L= 1 cd/m²; [b]CE/PE/EQE measured at maximum/100 cd/m²/1000 cd/m²; [c]measured at maximum current efficiency.

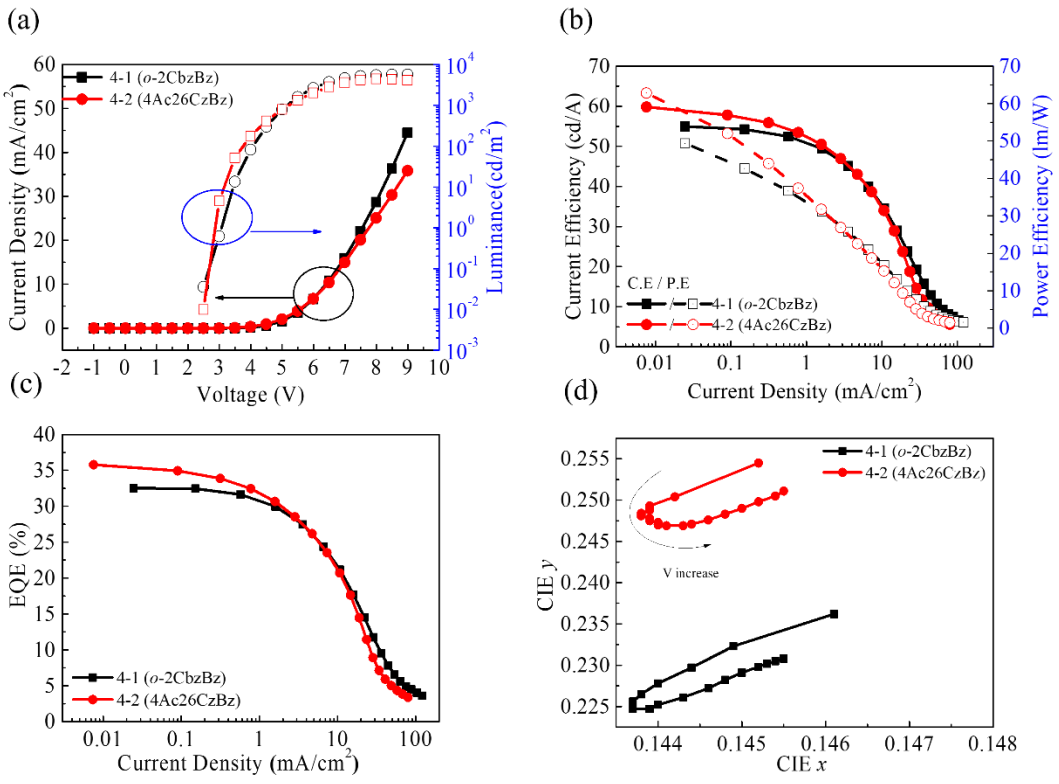

Fig. 4-11 (a) J-L-V curves, (b) current efficiency and power efficiency versus J, (c) EQE

doi:10.6342/NTU202503850

versus J, and (d) CIE coordinates at different voltages.

Fig. 4 10 (a) presented the J-L-V characteristics of the devices. Fig. 4 10 (b) and (c) showed the current efficiency, power efficiency, and EQE under different current densities. For OLEDs with *o*-2CbzBz and 4Ac26CzBz as EML hosts, the maximum current efficiencies were 59.4 cd/A and 59.8 cd/A, the maximum power efficiencies were 55.0 lm/W and 62.8 lm/W, and the maximum EQEs were 32.5% and 35.8%, respectively. Fig. 4 10 (d) illustrated the CIE coordinates as a function of driving voltage. Among the two OLEDs, device 4-1 exhibited a lower CIE-y value. The OLED with 4Ac26CzBz host achieved the higher EQE value (35.8%) compared to *o*-2CbzBz one, which was attributed to its higher PLQY for 4TCzBN doped in 4Ac26CzBz as listed in Table 4 2. Fig. 4 12 showed the TrEL results, where both devices exhibited long-delayed emission attributed to their TADF characteristics.

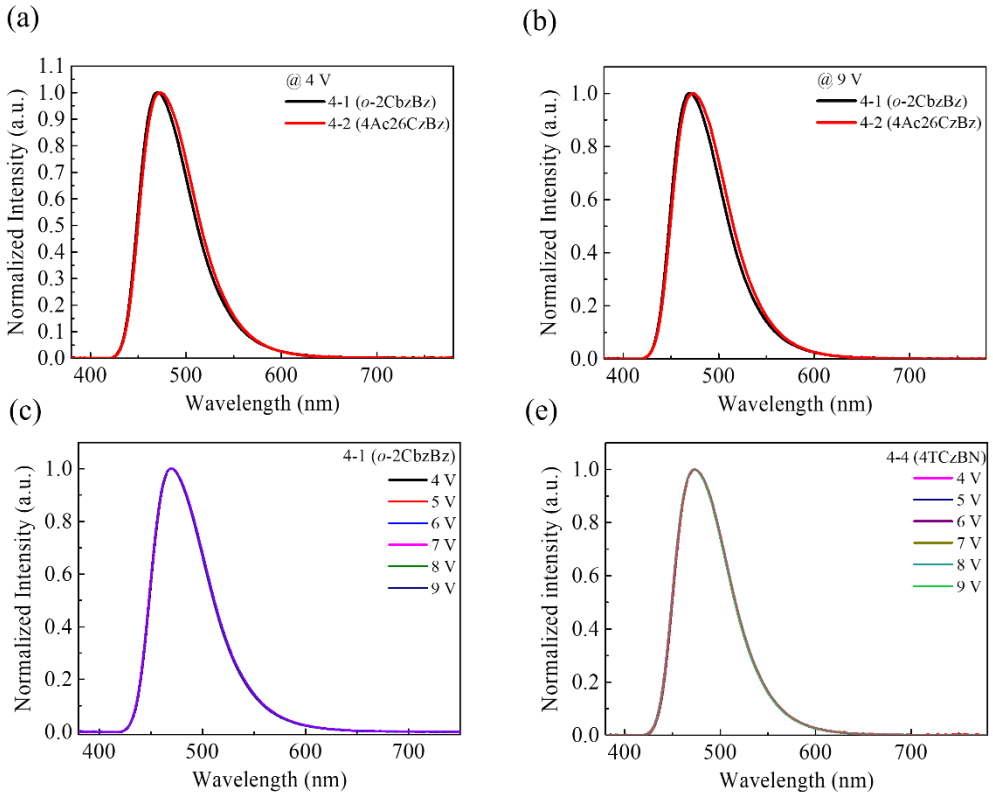

Fig. 4-12 EL spectra of devices (a) 4-1, and 4-2 with 4 V (b) 4-1, and 4-2 with 9 V (c) 4-1, and (d) 4-2 with different voltages.

doi:10.6342/NTU202503850

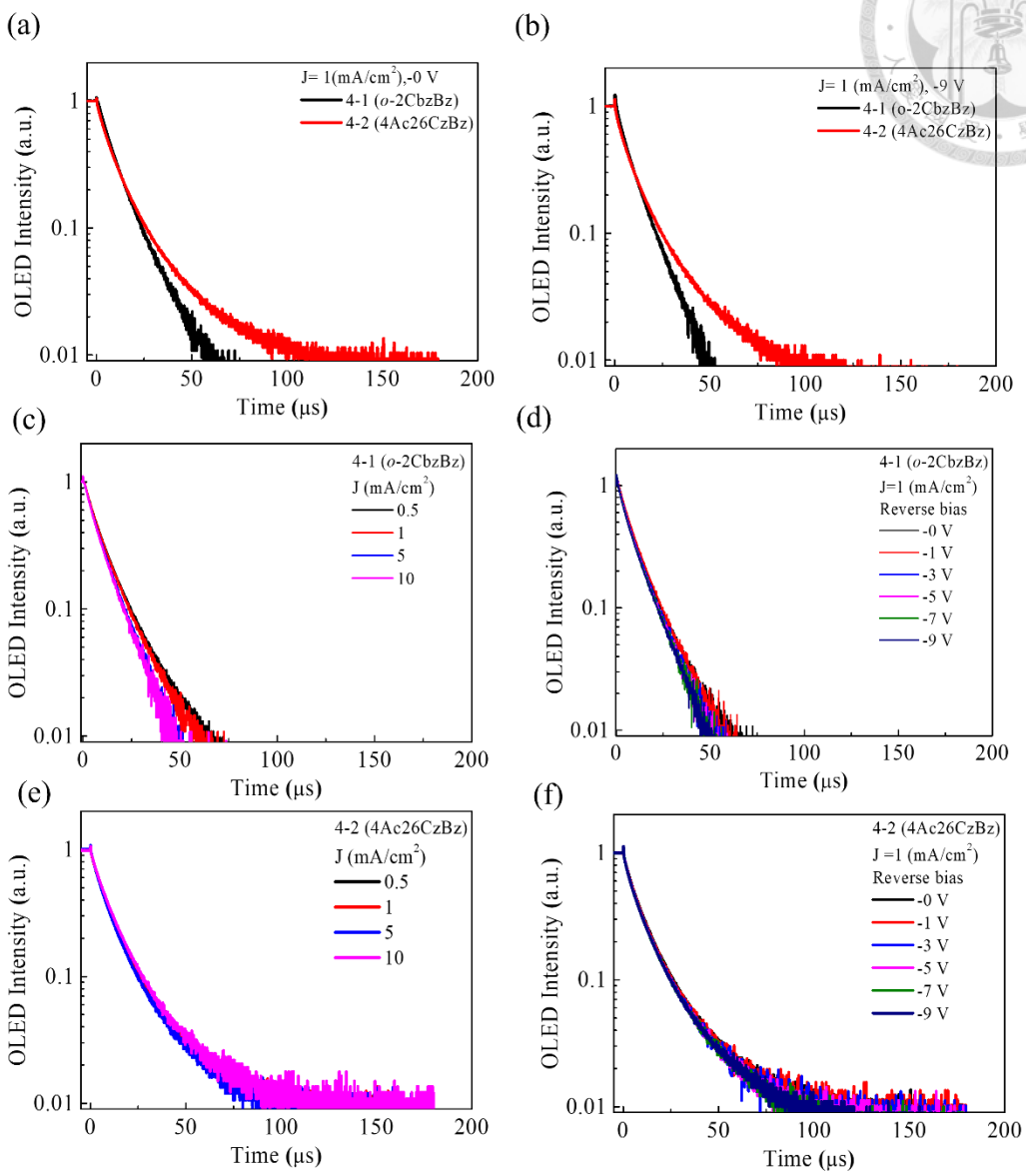

Fig. 4-13 TrEL of devices (a) 4-1, and 4-2 with J = 1 mA/cm^2, (b) 4-1, and 4-2 with J = 1 mA/cm^2, and switched to -9 V after t > 0, (c) 4-1 with different current densities, (d) 4-1 with different reverse bias after t > 0, (e) 4-2 with different current densities, and (f) 4-2 with different reverse bias after t > 0.

4.4 Optimization procedures of TADF OLED with

doi:10.6342/NTU202503850

4Ac26CzBz as host and 4TCzBN as the dopant

In sections 4-4, we demonstrated the optimization procedures with 4TCzBN as the emitters by selecting the host materials, dopant concentrations, and HTL thicknesses for achieving highest maximum EQE.

4.4.1 Optimization of dopant concentration

Table 4-5 showed 4TCzBN-doped device structures with concentrations ranging from 30%, 40%, to 50%. Fig. 4-14 (a) shows the energy diagram of the 4TCzBN-doped device.

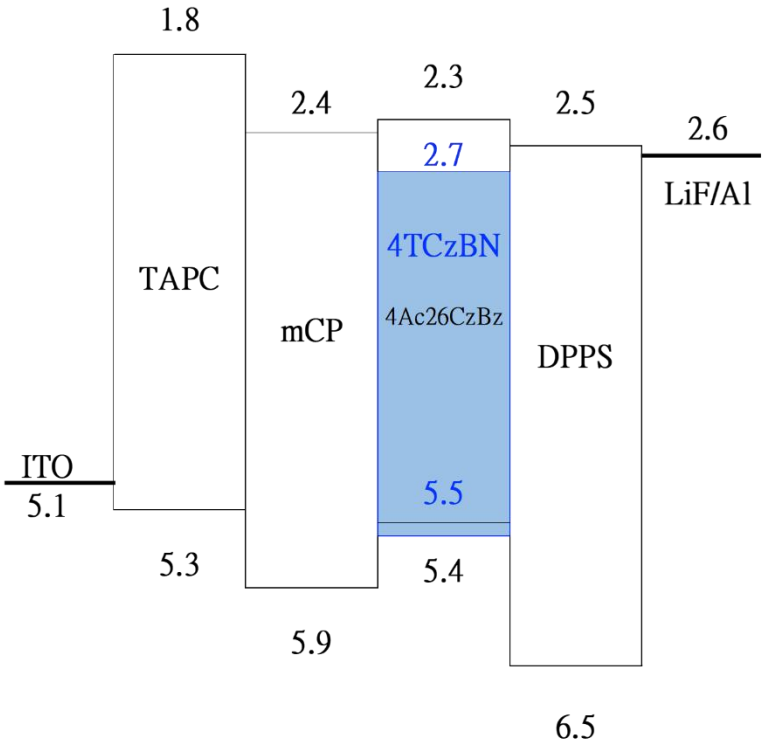

Fig. 4-14 Energy diagram of TADF-OLEDs with 4Ac26CzBz doped with 4TCzBN as the EML.

Table 4-5 Device structures of TADF OLED with 4Ac26CzBz and 4TCzBN as host

doi:10.6342/NTU202503850

and dopant at different dopant concentrations.

Device	HTL	EBL	EML	ETL	EIL/cathode
	TAPC	*m*CP	4Ac26CzBz: X% 4TCzBN (30 nm)	DPPS	LiF/Al
4-3	50	10	30%	50	0.8/120
4-4			40%		
4-5			50%		

unit: nm

Table 4-6 OLED performances of devices 4-3, 4-4, and 4-5.

Device	**Voltage[a] (V)**	**Max. Luminance (cd/m^2)**	**CE[b] (cd/A)**	**PE[b] (lm/W)**	**EQE[b] (%)**	**CIE[c] (x,y)**
4-3 (30%)	6.8/ 2.9	4756	59.6/56.6/52.3	62.5/46.8/35.4	35.3/33.9/31.4	(0.142,0.238)
4-4 (40%)	6.4/ 2.9	4756	59.9/56.8/47.2	62.8/47.6/27.1	35.8/34.4/28.6	(0.143,0.249)
4-5 (50%)	6.6/ 2.9	6660	58.5/57.1/50.7	61.4/47.8/32.2	33.5/33.1/29.6	(0.146,0.256)

[a]at J = 10 mA/cm^2/L= 1 cd/m^2; [b]CE/PE/EQE measured at maximum/100 cd/m^2/1000 cd/m^2; [c]measured at maximum current efficiency.

doi:10.6342/NTU202503850

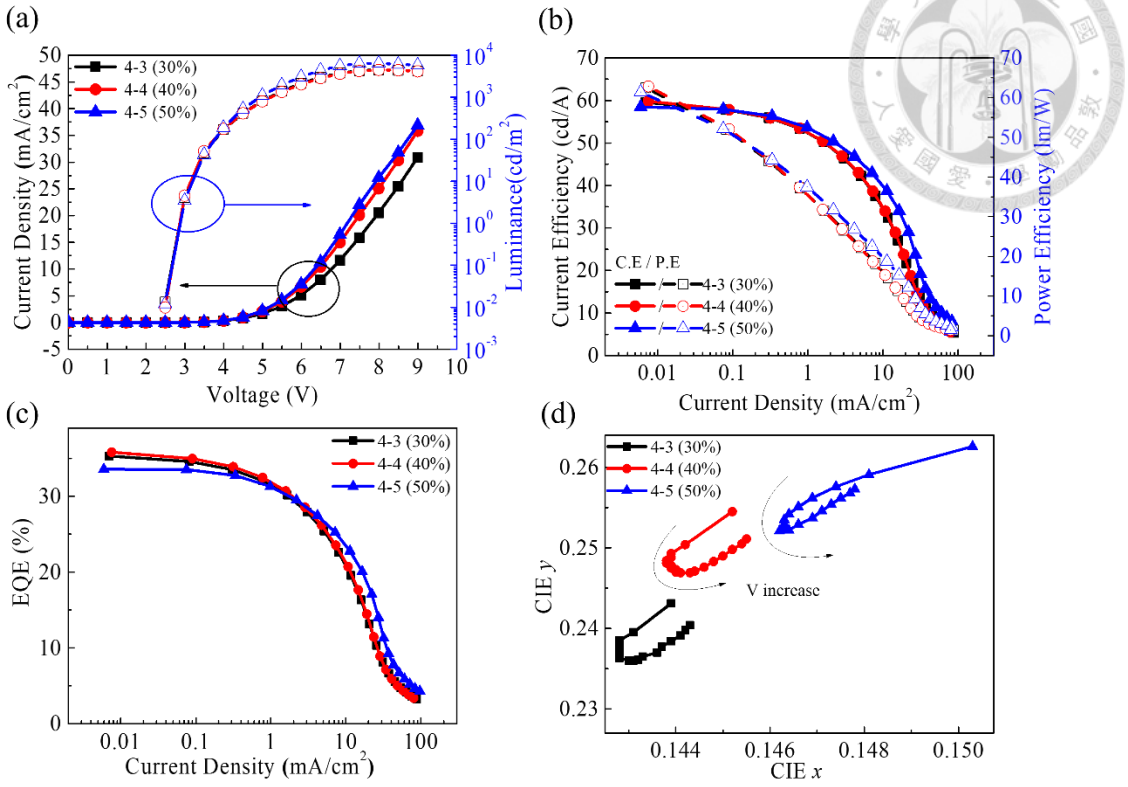

Fig. 4-15 (a) J-L-V curves, (b) current efficiency and power efficiency versus J, (c) EQE versus J, and (d) CIE coordinates at different voltages.

4TCzBN-doped device performances were shown in Fig. 4-14 and summarized in Table 4-6. Fig. 4-15 (a) showed the J-V and L-V characteristics of 4Ac26CzBz- based OLED with different 4TCzBN concentrations, i.e., 30%, 40%. 50%. Under the same driving voltage, device 4-5 exhibited higher current density and luminance than other two devices. OLED doped with 40% 4TCzBN (device 4-4) exhibited a maximum current efficiency, maximum power efficiency, and maximum EQE of 59.9 cd/A, 62.8 lm/W, and 35.8%, as shown in Fig. 4-15 (b) and (c). Fig. 4-15 (d) showed CIE coordinates, where device 4-3 exhibited a lowest CIE-y value. Fig. 4-16 presented the EL spectra of devices 4-3, 4-4, and 4-5. All OLEDs showed 4TCzBN emission, indicating successful energy transfer from host to dopant.

doi:10.6342/NTU202503850

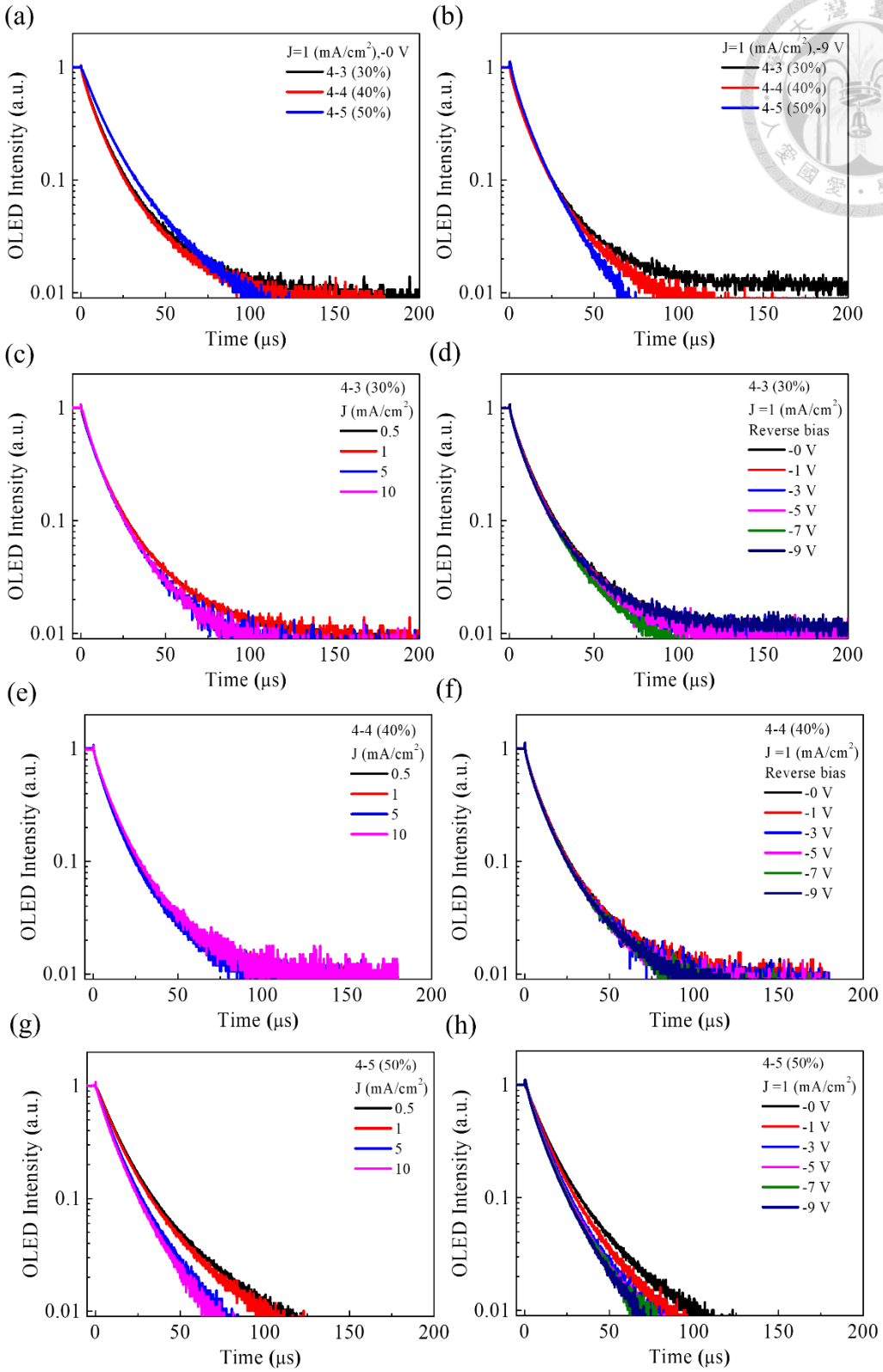

Fig. 4-17 showed the TrEL decay curves of devices 4-3, 4-4, and 4-5 in a 400 μs window, which exhibited long-delayed emission attributed to their TADF characteristics.

doi:10.6342/NTU202503850

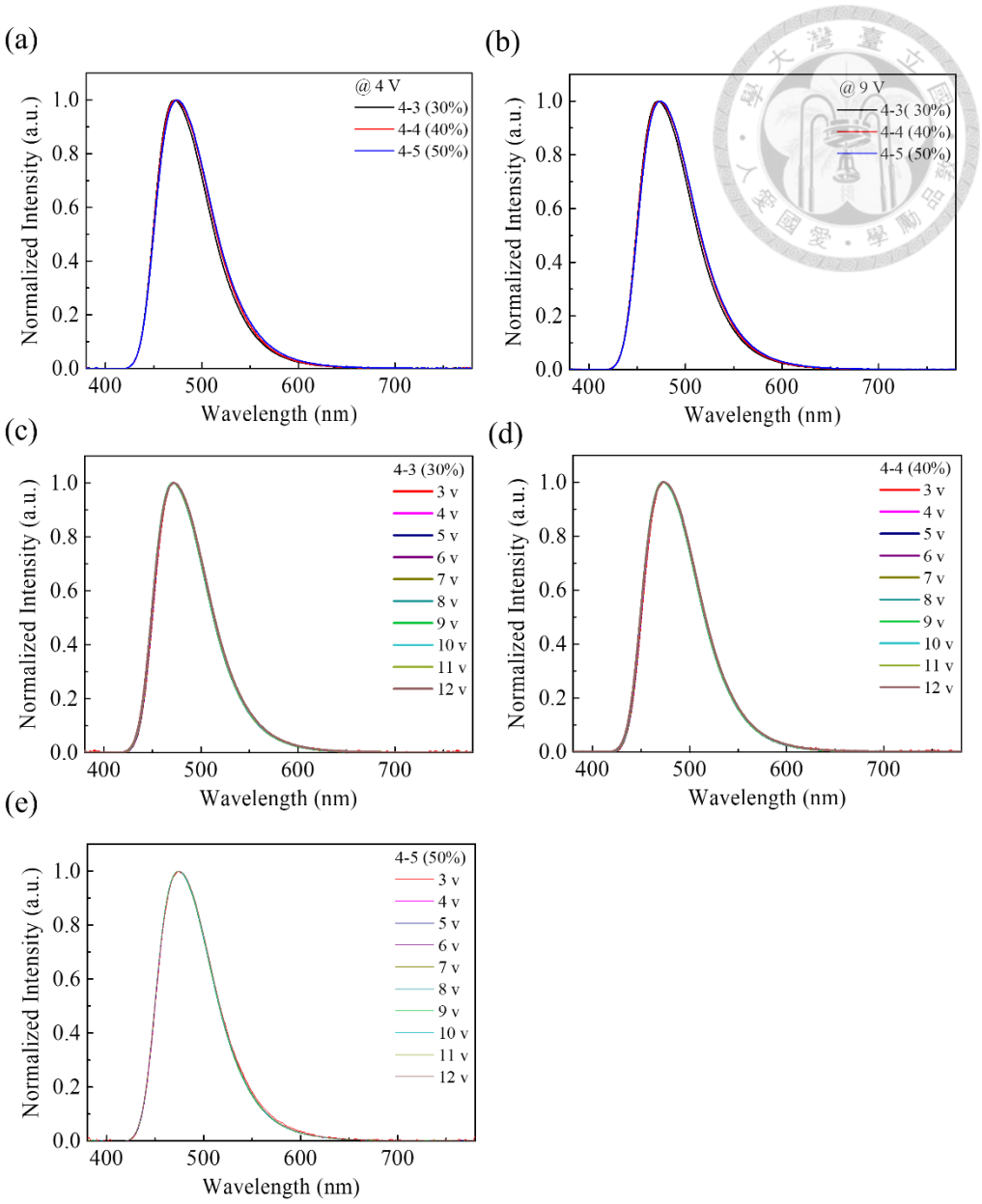

Fig. 4-16 EL spectra of devices (a) 4-3, 4-4 and 4-5 with 4 V (b) 4-3, 4-4 and 4-5 with 9 V, (c) 4-3, (d) 4-4, and (e) 4-5 with different voltages.

doi:10.6342/NTU202503850

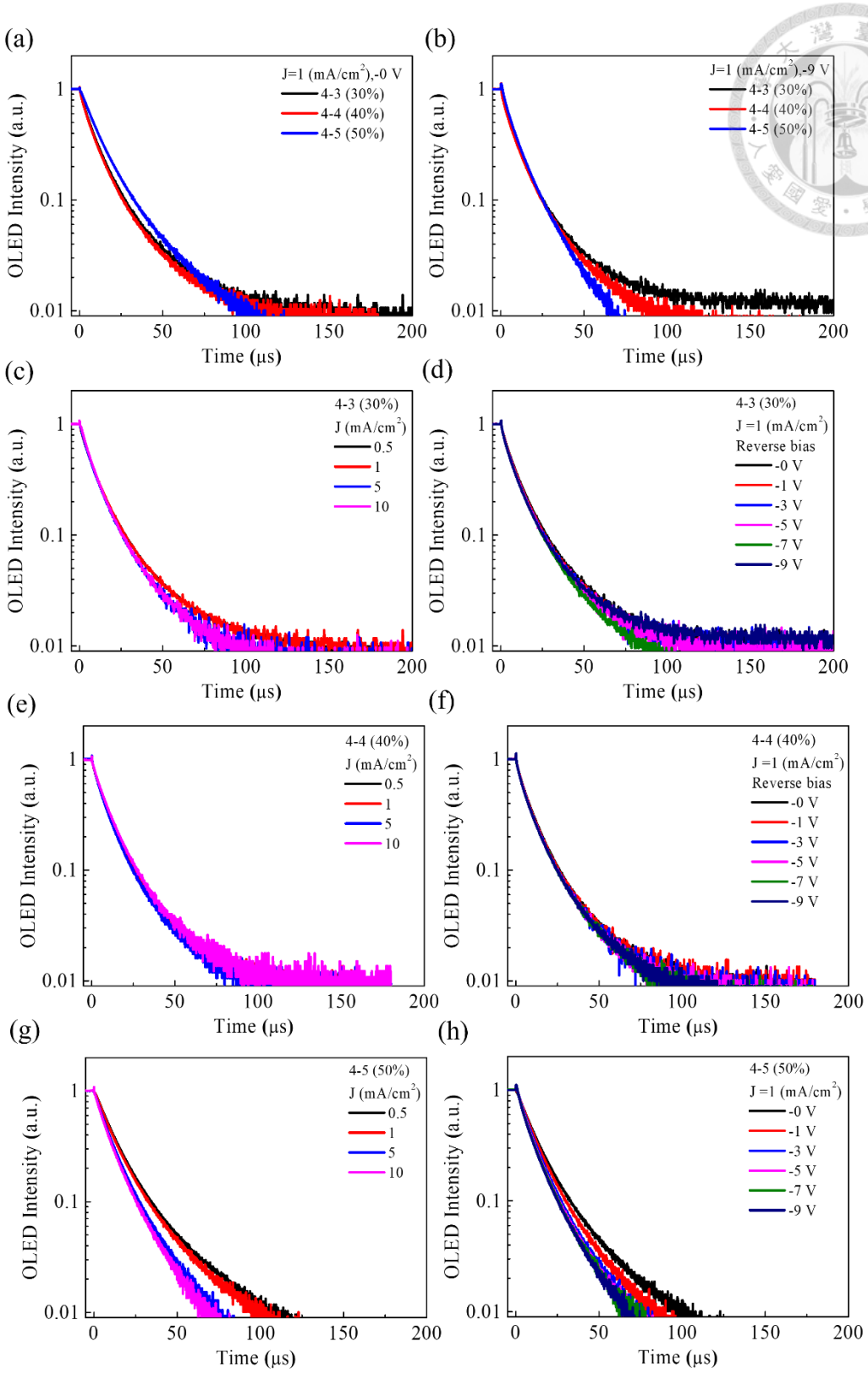

Fig. 4-17 TrEL of devices (a) 4-3, 4-4 and 4-5 with J = 1 mA/cm^2, (b) 4-3, 4-4 and 4-5 with J = 1 mA/cm^2, and switched to -9 V after t > 0, (c) 4-3 with different current densities, (d) 4-3 with different reverse bias after t > 0, (e) 4-4 with different current

doi:10.6342/NTU202503850

densities, (f) 4-4 with different reverse bias after t > 0, (g) 4-5 with different current densities, and (h) 4-5 with different reverse biases after t > 0.

4.4.1 Optimization of ETL thickness

In this session, we fixed the different dopant concentrations and adjusted thickness of the ETL from 50, 55, to 60 nm for obtaining the highest maximum EQE.

Table 4-7 Device structures of OLEDs with different ETL thickness

Device	HTL	EBL	EML	ETL	EIL/cathode
	TAPC	*m*CP	4Ac26CzBz: 40% 4TCzBN	DPPS	LiF/Al
4-6	50	10	30	50	0.8/120
4-4				55	
4-7				60	

unit: nm

Table 4-8 OLED performances of devices 4-6, 4-4, and 4-7.

Device	**Voltage[a] (V)**	**Max. Luminance (cd/m^2)**	**CE[b] (cd/A)**	**PE[b] (lm/W)**	**EQE[b] (%)**	**CIE[c] (x,y)**
4-6(50 nm)	5.7/2.9	7051	53.1/52.9/52.9	55.7/53.3/52.2	30.6/30.7/30.6	(0.145, 0.220)
4-4(55 nm)	6.4/6.4	4756	59.8/56.8/47.2	62.8/47.6/27.1	35.8/34.4/28.6	(0.145, 0.254)
4-7(60 nm)	7.4/7.4	4639	58.9/58.4/58.2	61.8/56.4//55.3	33.3/33.13/33.1	(0.154, 0.253)

[a]at J = 10 mA/cm^2/L= 1 cd/m^2; [b]CE/PE/EQE measured at maximum/100 cd/m^2/1000 cd/m^2; [c]measured at maximum current efficiency.

doi:10.6342/NTU202503850

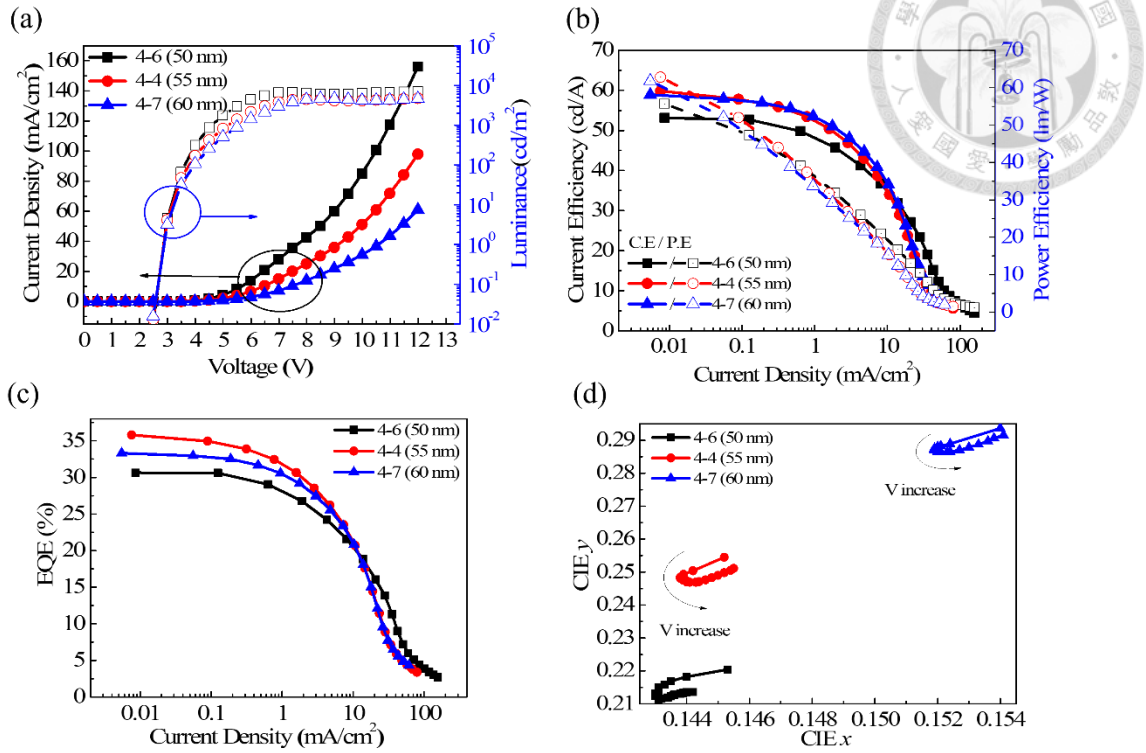

Fig. 4-18 (a) J-L-V curves, (b) current efficiency and power efficiency versus J, (c) EQE versus J, (d) CIE coordinates at different voltages.

Table 4-8 showed device performances of tuning ETL. Fig. 4-18 (a) showed J-L-V curves, and device 4-6 exhibited the highest current density because of the thinnest ETL. Fig. (b), and (c) was current efficiency, power efficiency, and EQE under different current density respectively. Device 4-4 showed a maximum current efficiency, maximum power efficiency, and maximum EQE of 59.8 cd/A, 62.8 lm/W, and 35.8.%. Fig. 4-18 (d) was CIE coordinates, and the CIE-y value would be larger when the thickness of ETL increased. Fig. 4-19 showed the EL spectra of devices 4-6, 4-4, and 4-7. All of them showed emission spectra of 4TCzBN. Fig. 4-20 s showed the TrEL

doi:10.6342/NTU202503850

decay curves of devices 4-6, 4-4, and 4-7 in 400 μs window, which exhibited long-delayed emission attributed to their TADF characteristics.

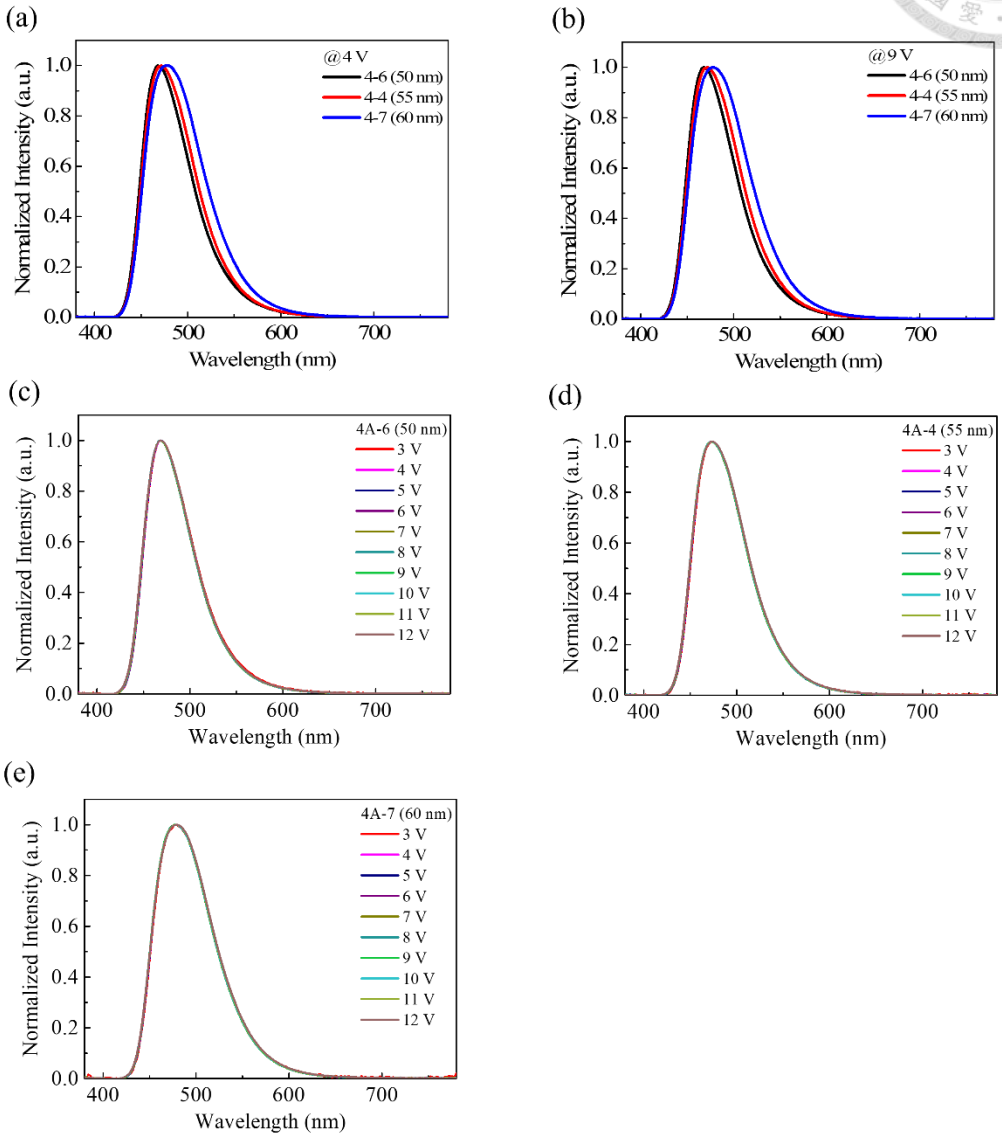

Fig. 4-19 EL spectra of devices (a) 4-6, 4-4 and 4-7 with 4 V (b) 4-6, 4-4 and 4-7 with 9 V (c) 4-6, (d) 4-4, and (e) 4-7 with different voltages.

doi:10.6342/NTU202503850

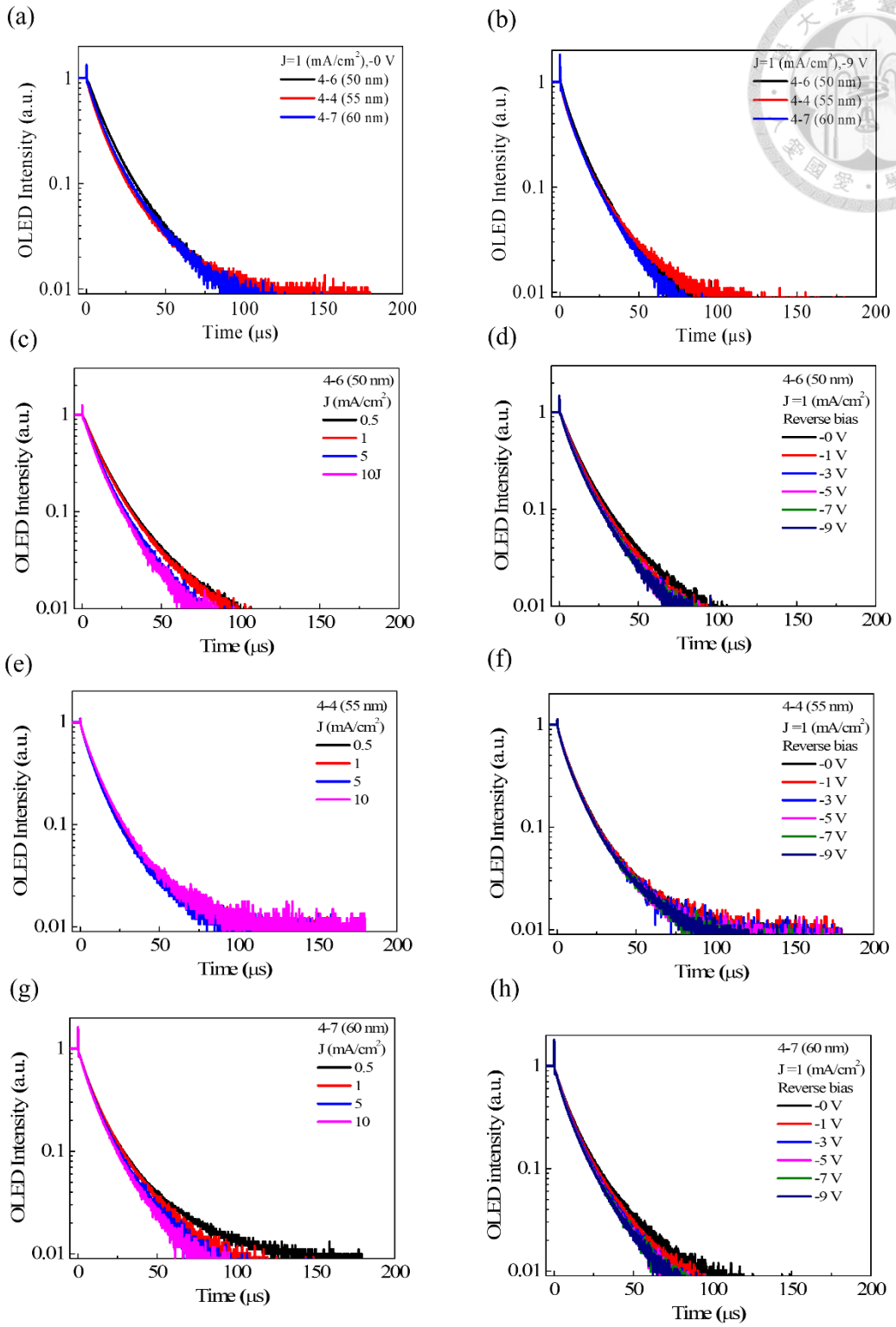

Fig. 4-20 TrEL of devices (a) 4-6, 4-4 and 4-7 with J = 1 mA/cm^2, (b) 4-6, 4-4 and 4-7 with J = 1 mA/cm^2, and switched to -9 V after t > 0, (c) 4-6 with different current densities, (d) 4-6 with different reverse bias after t > 0, (e) 4-4 with different current densities, (f) 4-4 with different reverse bias after t > 0, (g) 4-7 with different current

doi:10.6342/NTU202503850

densities, and (h) 4-7 with different reverse biases after t > 0.

4.4.2 Optimization of EML thickness

Here, we fixed dopant concentration at 40%, thickness of the ETL at 55 nm, and tuned the thickness of EML from 25, 30, to 35 nm. The detailed device structures were shown in Table 4-9, and the device performances were summarized in Table 4-10.

Table 4-9 Device structures of OLEDs with adjusting the thickness of EML.

Device	HTL	EBL	EML	ETL	EIL/cathode
	TAPC	*m*CP	4Ac26CzBz: 40% 4TCzBN	DPPS	LiF/Al
4-8	50	10	25	55	0.8/120
4-4			30		
4-9			35		

unit: nm

Table 4-10 OLED performances of devices 4-8, 4-4, and 4-9.

Device	**Voltage[a] (V)**	**Max. Luminance (cd/m^2)**	**CE[b] (cd/A)**	**PE[b] (lm/W)**	**EQE[b] (%)**	**CIE[c] (x,y)**
4-8 (25 nm)	6.2/6.3	7051	56.9/55.1/48.5	59.7/46.1/31.6	31.9/31.2/27.8	(0.145, 0.233)
4-4 (30 nm)	6.4/6.4	4756	59.8/56.8/47.2	62.8/47.6/27.1	35.8/34.4/28.6	(0.145, 0.254)
4-9 (35 nm)	6.8/6.7	4639	56.9/55.3/49.3	59.7/44.8/29.6	32.8/32.1/28.7	(0.149, 0.264)

[a]at J = 10 mA/cm^2/L= 1 cd/m^2; [b]CE/PE/EQE measured at maximum/100 cd/m^2/1000 cd/m^2; [c]measured at maximum current efficiency.

doi:10.6342/NTU202503850

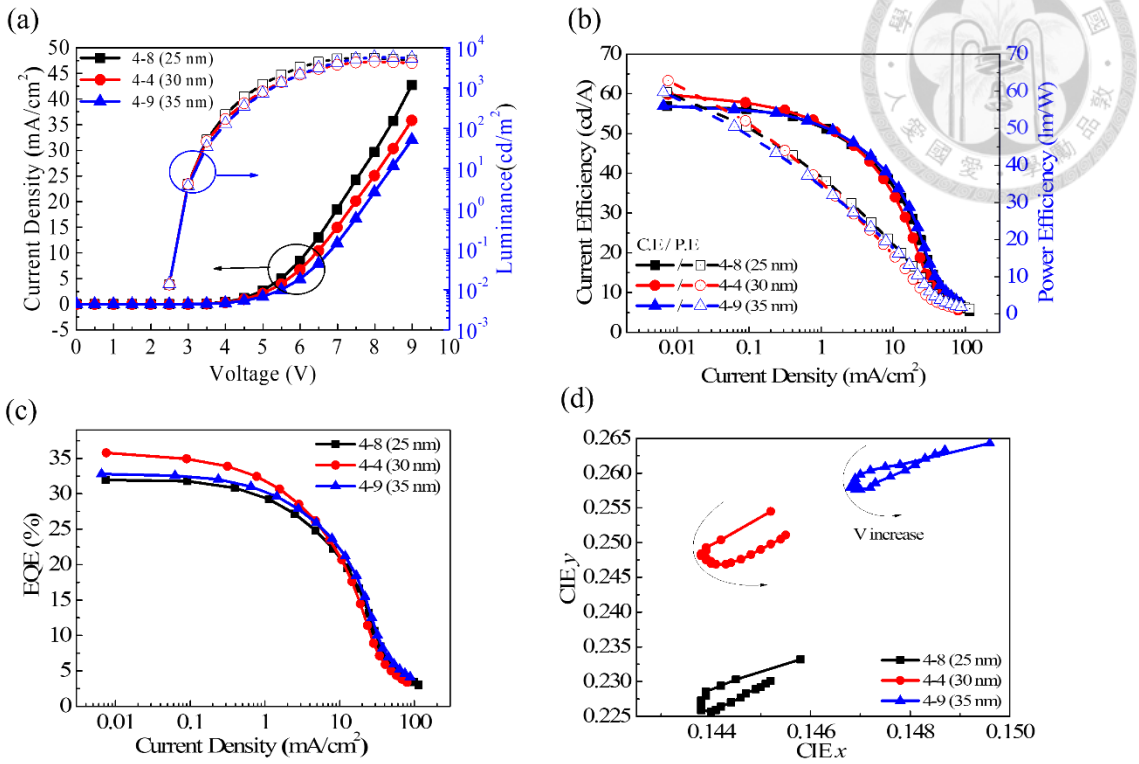

Fig. 4-21 (a) J-L-V curves, (b) current efficiency and power efficiency versus J, (c) EQE versus J, and (d) CIE coordinates at different voltages.

Table 4-10 was device performances. Fig. 4-21 (a) was J-L-V curves, the current density was lower as the EML is thicker. Fig. 4-21 (b), and (c) was current efficiency, power efficiency, and EQE under different current density. Device 4-4 showed the maximum current efficiency, maximum power efficiency, and maximum EQE of 59.8 cd/A, 62.8 lm/W, and 35.8%. Fig. 4-21 (d) was CIE coordinates. It can be observed that y-value of the CIE coordinates for devices 4-8 was lowest because the EML was relatively thinnest. Fig. 4-22 showed the EL spectra of devices 4-8, 4-4, and 4-9, resulting from 4TCzBN emission. Fig. 4-23 showed the TrEL decay curves of devices

doi:10.6342/NTU202503850

4-8, 4-4, and 4-9 in a 400 μs window, which exhibited long-delayed emission attributed to their TADF characteristics.

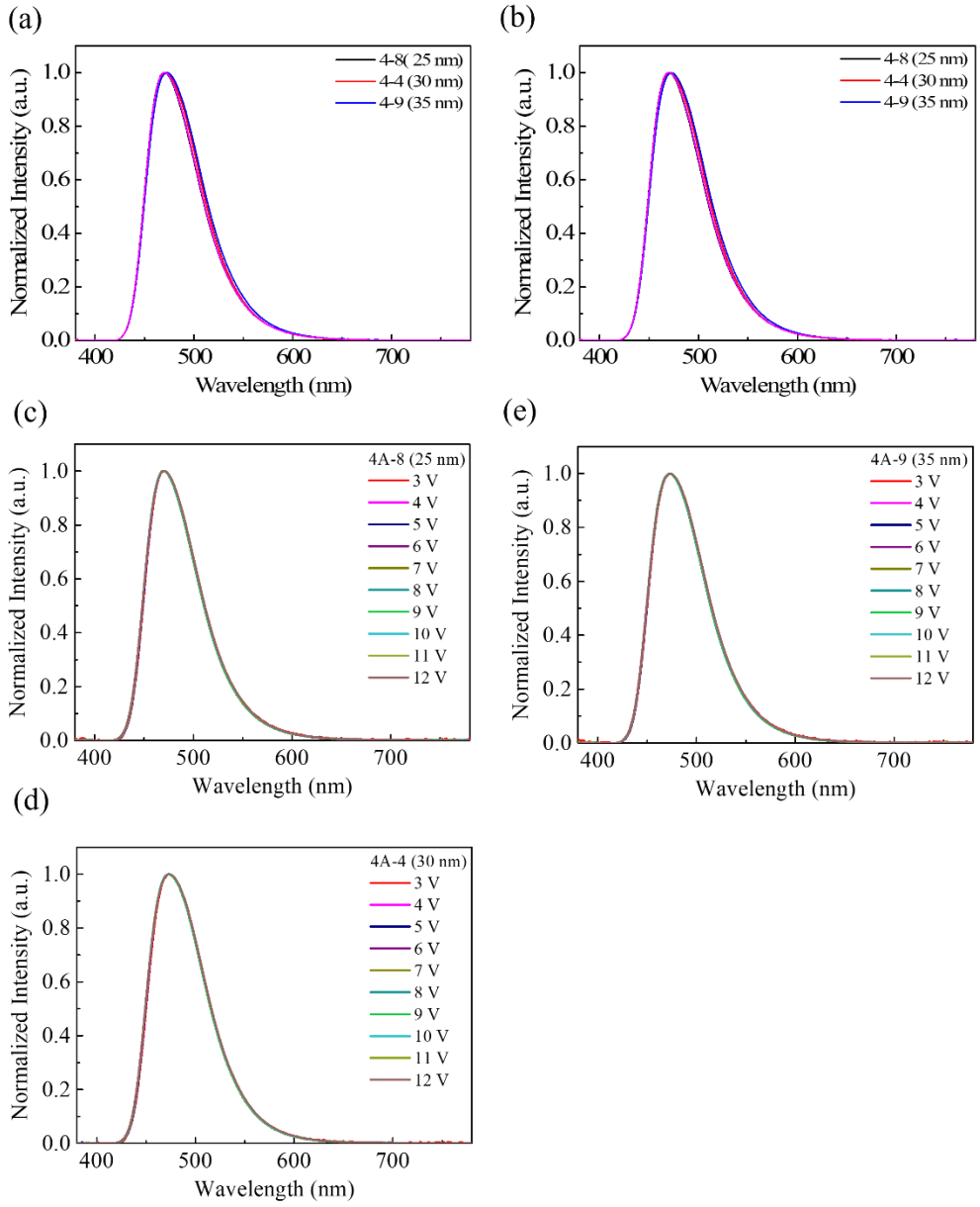

Fig. 4-22 EL spectra of devices (a) 4-8, 4-4 and 4-9 with 4 V (b) 4-8, 4-4 and 4-9 with 9 V (c) 4-8, (d) 4-4, and (e) 4-9 with different voltages.

doi:10.6342/NTU202503850

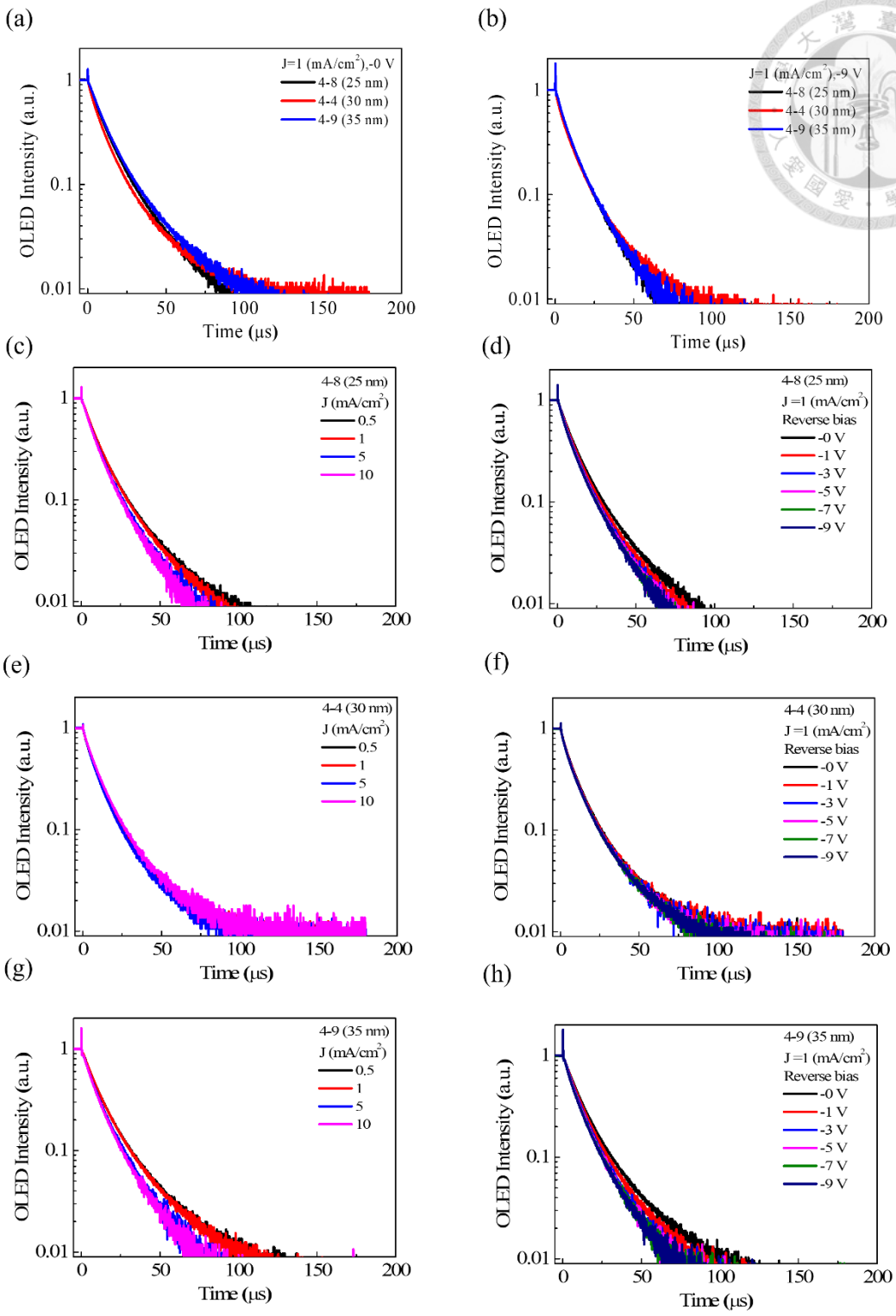

Fig. 4-23 TrEL of devices (a) 4-8, 4-4 and 4-9 with J = 1 mA/cm^2, (b) 4-8, 4-4 and 4-9 with J = 1 mA/cm^2, and switched to -9 V after t > 0, (c) 4-8 with different current densities, (d) 4-8 with different reverse bias after t > 0, (e) 4-4 with different current densities, (f) 4-4 with different reverse bias after t > 0, (g) 4-9 with different current

doi:10.6342/NTU202503850

densities, and (h) 4-9 with different reverse biases after J > 0.

4.5 Sky-blue Phosphorescent OLED with FIrpic emitter

In this session, we tested three different hosts doped with sky-blue phosphorescent emitter as the EML of the OLED. The energy diagram of the phosphorescent (Ph-) OLEDs was shown in Fig. 4-24.with three hosts, i.e. *o*-2CbzBz, 9,9',9''-(2-(1-phenyl-1H-benzo[d]imidazol-2-yl)benzene-1,3,5-triyl)tris(9H-carbazole) *o*-3CbzBz and 4Ac26CzBz, doped with Bis[2-(4,6-difluorophenyl)pyridinato-C^2,N](picolinato)iridium(III) FIrpic emitter. Table 4-11 presented the device structures, and their performances were summarized in

doi:10.6342/NTU202503850

Table 4-12.

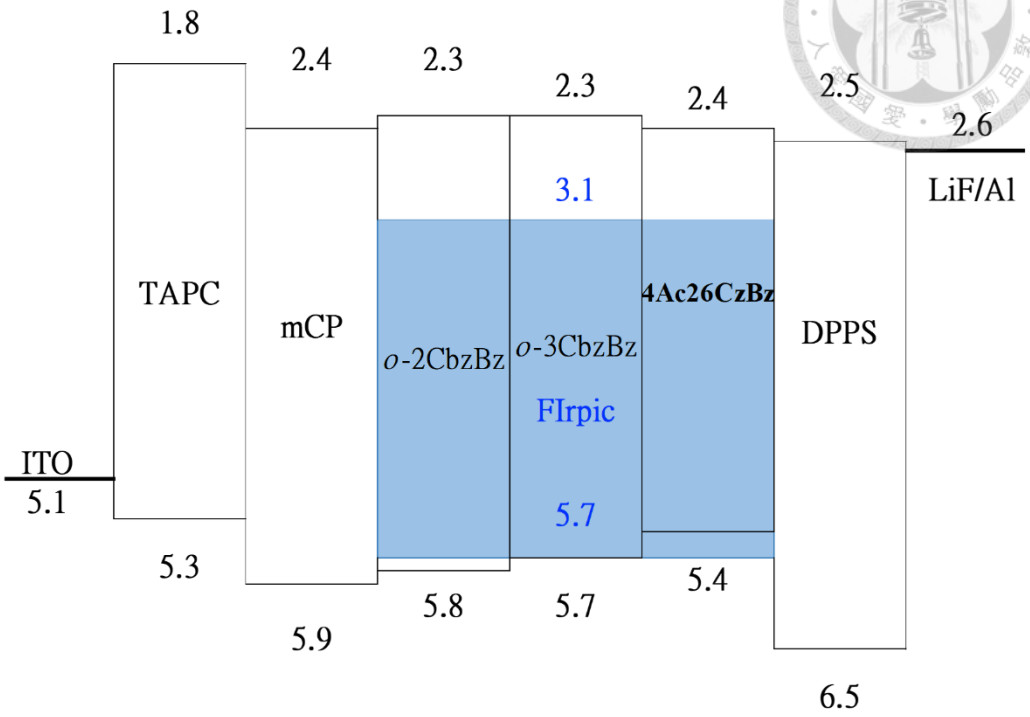

Fig. 4-24 Energy diagram of Ph-OLEDs, where 4Ac26CzBz, *o*-2Cbzbz, and *o*-3CbzBz with FIrpic as the emitter.

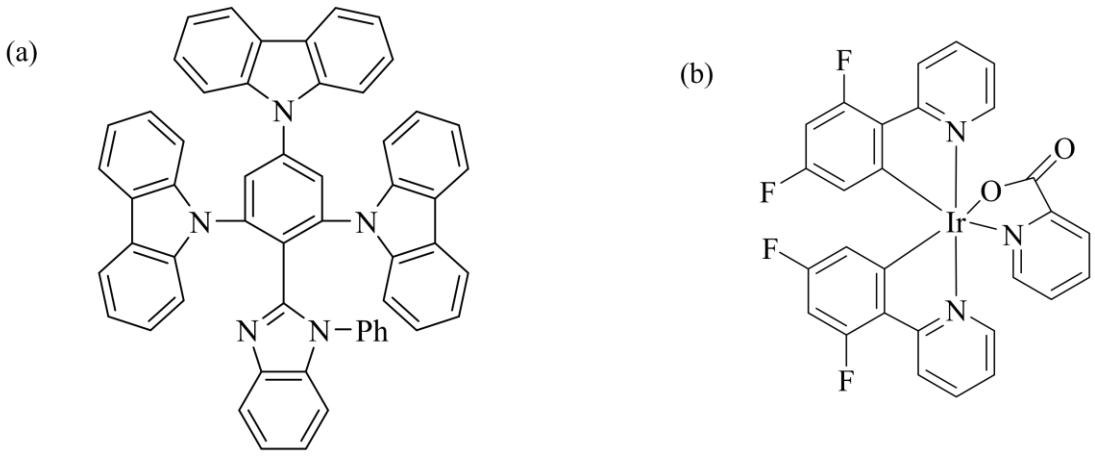

Fig. 4-25 Molecular structures of (a) *o*-3CbzBz and (b) FIrpic.

Table 4-11 Device structures of Ph-OLED with 4Ac26CzBz, *o*-2CbzBz, and *o*-

doi:10.6342/NTU202503850

3CbzBz hosts with FIrpic as an emitter.

Device	HTL	EBL	EML	ETL	EIL/cathode
	TAPC	*m*CP	9% FIrpic (30 nm)	DPPS	LiF/Al
4-10	50	10	4Ac26CzBz	55	0.8/120
4-11			*o*-2CbzBz		
4-12			*o*-3CbzBz		

unit: nm

Table 4-12 OLED performances of devices 4-10, 4-11, and 4-12.

Device	**Voltage[a] (V)**	**Max. Luminance (cd/m^2)**	**CE[b] (cd/A)**	**PE[b] (lm/W)**	**EQE[b] (%)**	**CIE[c] (x,y)**
4-10 (4Ac26CzBz)	6.3/2.8	8637	60.6/59.9/57.7	63.2/38.1/27.6	27.7/27.6/26.5	(0.159,0.391)
4-11 (*o*-2CbzBz)	7.2/3.1	18207	64.7/64.7/61.8	50.9/46.5/34.9	28.6/28.5/27.4	(0.152, 0.300)
4-12 (*o*-3CbzBz)	6.7/3.2	13730	56.4/56.4/54.3	56.0/43.4/32.5	25.9/25.9/25.2	(0.152, 0.386)

[a]at J = 10 mA/cm^2/L= 1 cd/m^2; [b]CE/PE/EQE measured at maximum/100 cd/m^2/1000 cd/m^2; [c]measured at maximum. current efficiency.

doi:10.6342/NTU202503850

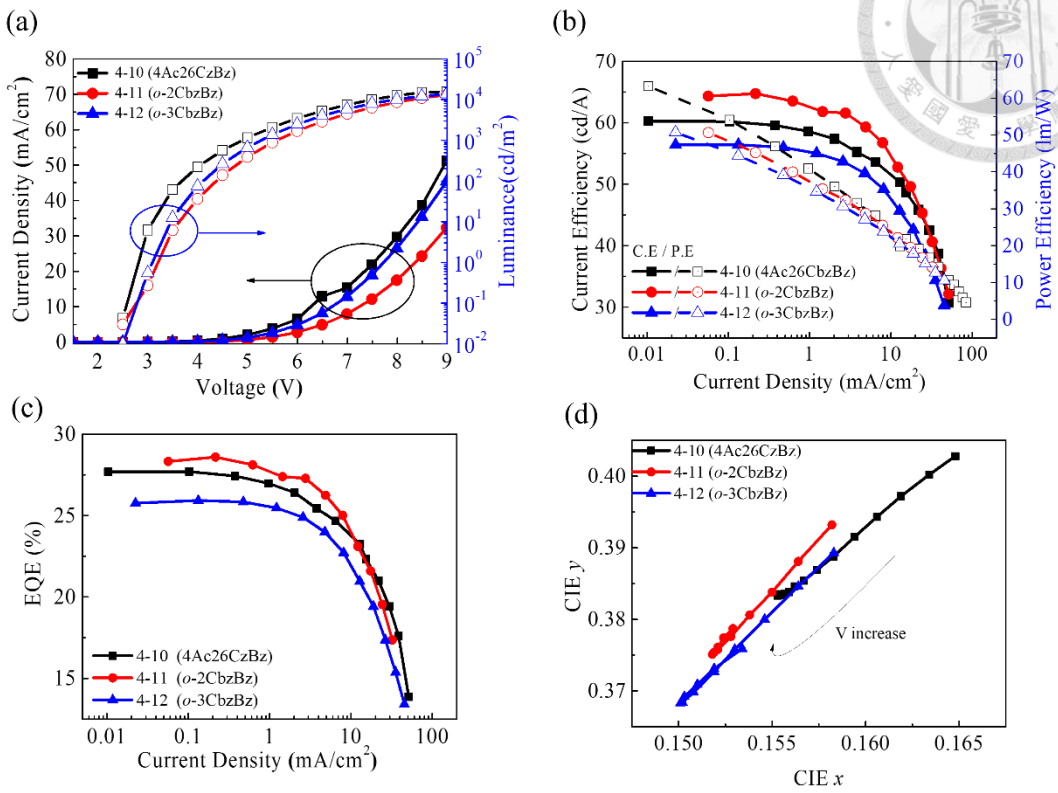

Fig. 4-26 (a) J-L-V curves, (b) current efficiency and power efficiency versus J, (c) EQE versus J, and (d) CIE coordinates at different voltages.

Table 4-11 showed device performances. Fig. 4-26 (a) displayed the J-L-V curves of the devices. Fig. 4-26 (b), and (c) showed current efficiency, power efficiency, and EQE under different current density. Fig. 4-26 (d) illustrated the CIE coordinates as a function of voltage. By incorporating acridine, which exhibited strong electron-donating capability to tune the HOMO level of 4Ac26CzBz thereby facilitating hole transport in the OLED, the HOMO value was reduced to 5.4 eV, compared to *o*-2CbzBz (5.8 eV). We expect that this modification can reduce the driving voltage of the OLED. At a current density of J = 10 mA/cm², the driving voltages of devices 4-10 was 6.3 V, which was lower than devices 4-11 and 4-12. Under a 9% FIrpic doping concentration, device 4-10 based on 4Ac26CzBz achieves a maximum power efficiency of 63.2 lm/W.

doi:10.6342/NTU202503850

Fig. 4-28 showed the TrEL decay curves of devices 4-10, 4-11, and 4-12 in 20 μs. window, which exhibited delayed emission.

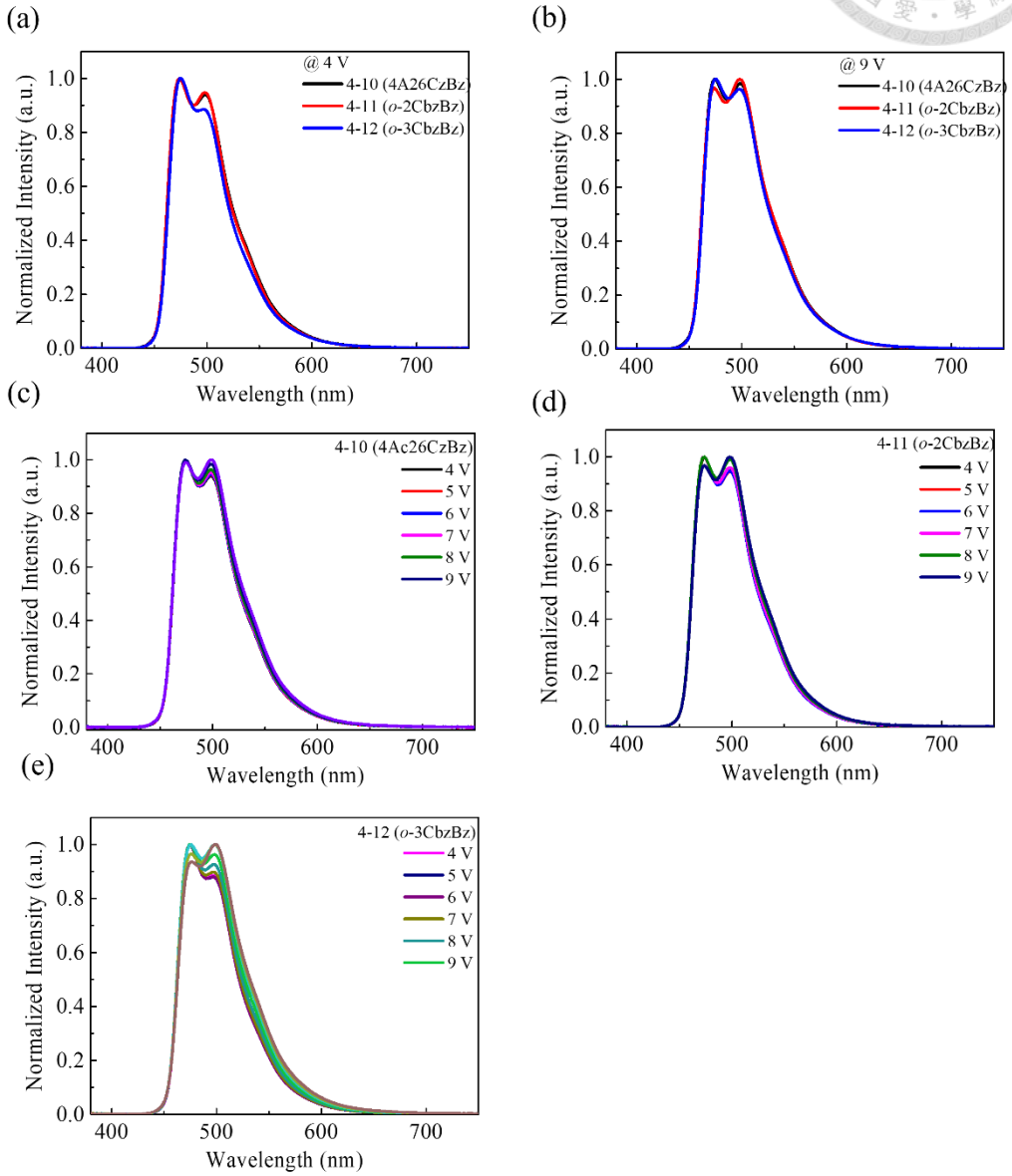

Fig. 4-27 EL spectra of devices (a) 4-10, 4-11 and 4-12 with 4 V (b) 4-10, 4-11 and 4-12 with 9 V (c) 4-10, (d) 4-11, and (e) 4-12 with different voltages.

doi:10.6342/NTU202503850

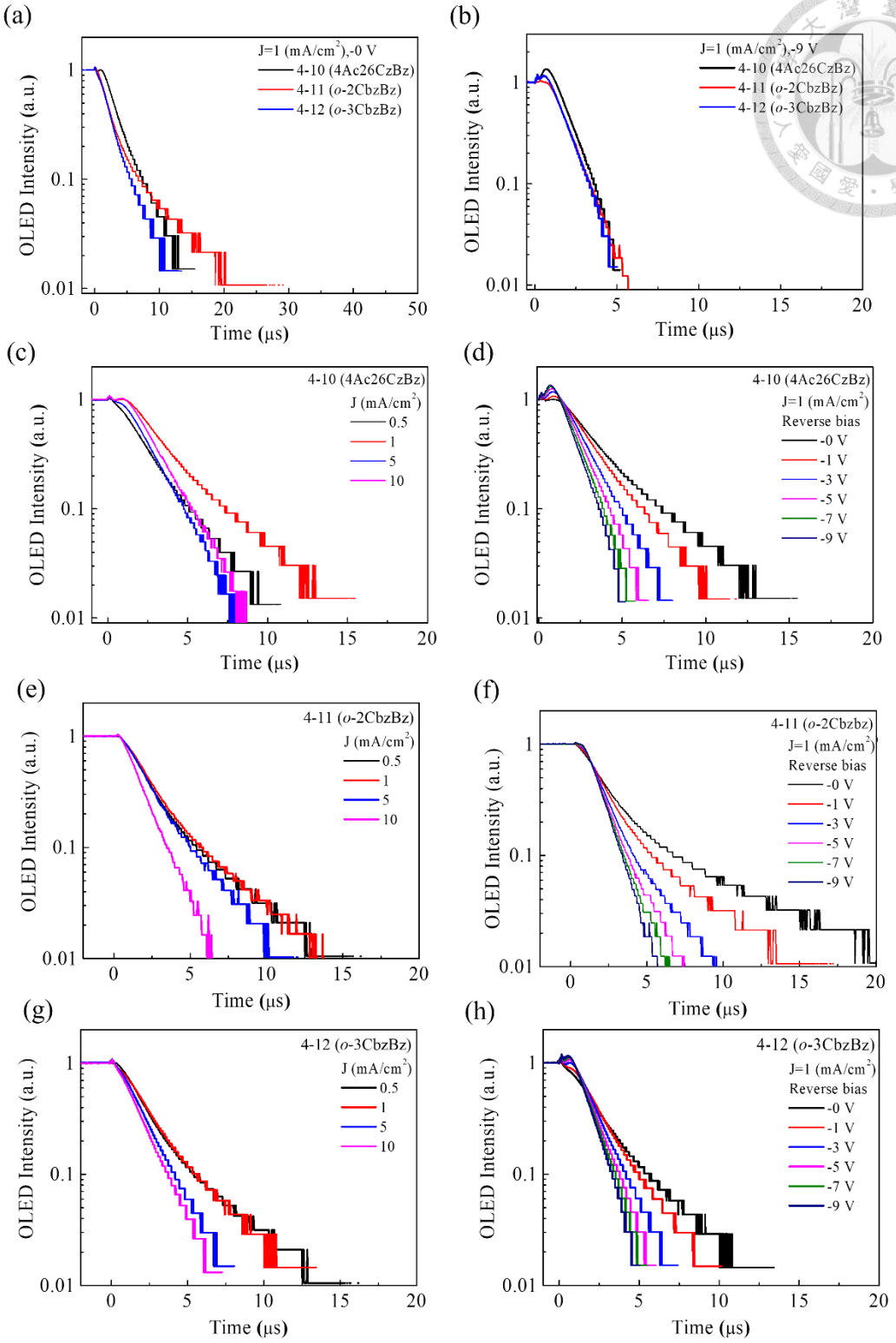

Fig. 4-28 TrEL of devices (a) 4-10, 4-11 and 4-12 with J = 1 mA/cm^2, (b) 4-10, 4-11 and 4-12 with J = 1 mA/cm^2, and switched to -9 V after t > 0, (c) 4-10 with different current densities, (d) 4-10 with different reverse bias after t > 0, (e) 4-11 with different current densities, (f) 4-11 with different reverse bias after t > 0, (g) 4-12 with different

doi:10.6342/NTU202503850

current densities, and (h) 4-12 with different reverse bias after t > 0.

4.5.1 FIrpic-based OLED with Different EBL Materials

Then, we changed four different EBL materials in Ph-OLED based on FIrpic: 4Ac26CzBz as the EML, which included 4,4',4"-Tris(carbazol-9-yl)triphenylamine (TCTA), mCP, and 4Ac26CzBz. Besides, an OLED with EBL was also fabricated. The energy diagram was shown in Fig. 4-29. The device structures were shown in Table 4-13, and the device performances were shown in Table 4-14.

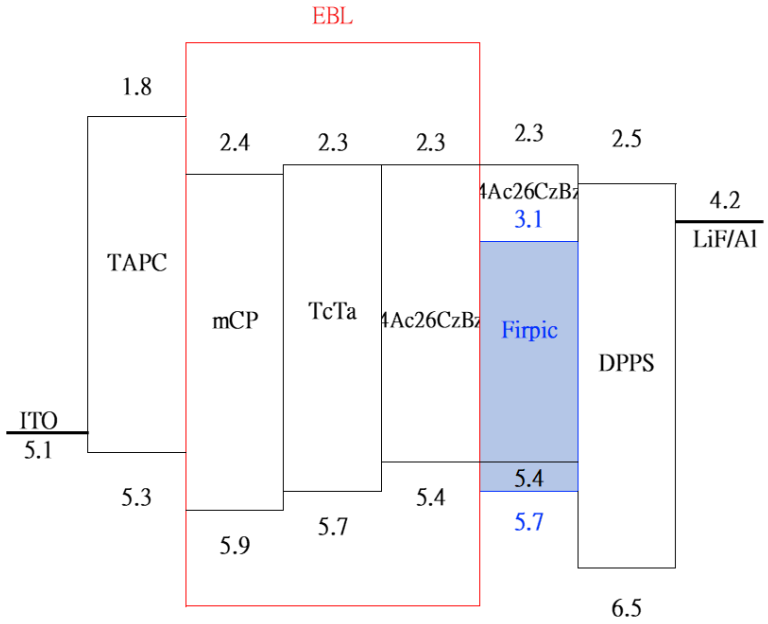

Fig. 4-29 Energy diagram of OLEDs with different EBLs.

Table 4-13 Device structures of OLEDs with different EBLs.

Device	HTL	EBL	EML	ETL	EIL/cathode

doi:10.6342/NTU202503850

	TAPC	X (10 nm)	4Ac26CzBz: 9%FIrpic	DPPS	LiF/Al
4-10	50	mCP	30	55	0.8/120
4-13		TcTa			
4-14		Non			
4-15		4Ac26CzBz			

unit: nm

Table 4-14 OLED performances of devices 4-10, 4-13, 4-14, and 4-15.

Device	Voltage[a] (V)	Max. Luminance (cd/m^2)	CE[b] (cd/A)	PE[b] (lm/W)	EQE[b] (%)	CIE[c] (x,y)
4A-10 (mCP)	6.3/2.8	8637	60.6/59.9/57.7	63.2/38.1/27.6	27.7/27.6/26.5	(0.159,0.391)
4A-13 (TcTa)	5.3/2.7	15380	59.9/59.7/58.8	53.8/53.7/44.2	27.0/26.9/26.7	(0.153,0.378)
4A-14 (non)	6.3/2.9	12840	58.8/59.2/57.3	52.9/46.9/36.5	28.9/28.8/28.1	(0.147,0.357)
4A-15 (4Ac26CzBz)	6.7/3.0	14880	55.4/56.9/56.3	49.8/43.1/33.4	25.7/25.4/25.4	(0.153,0.383)

[a]at J = 10 mA/cm^2/L= 1 cd/m^2; [b]CE/PE/EQE measured at maximum/100 cd/m^2/1000 cd/m^2; [c]measured at maximum current efficiency.

doi:10.6342/NTU202503850

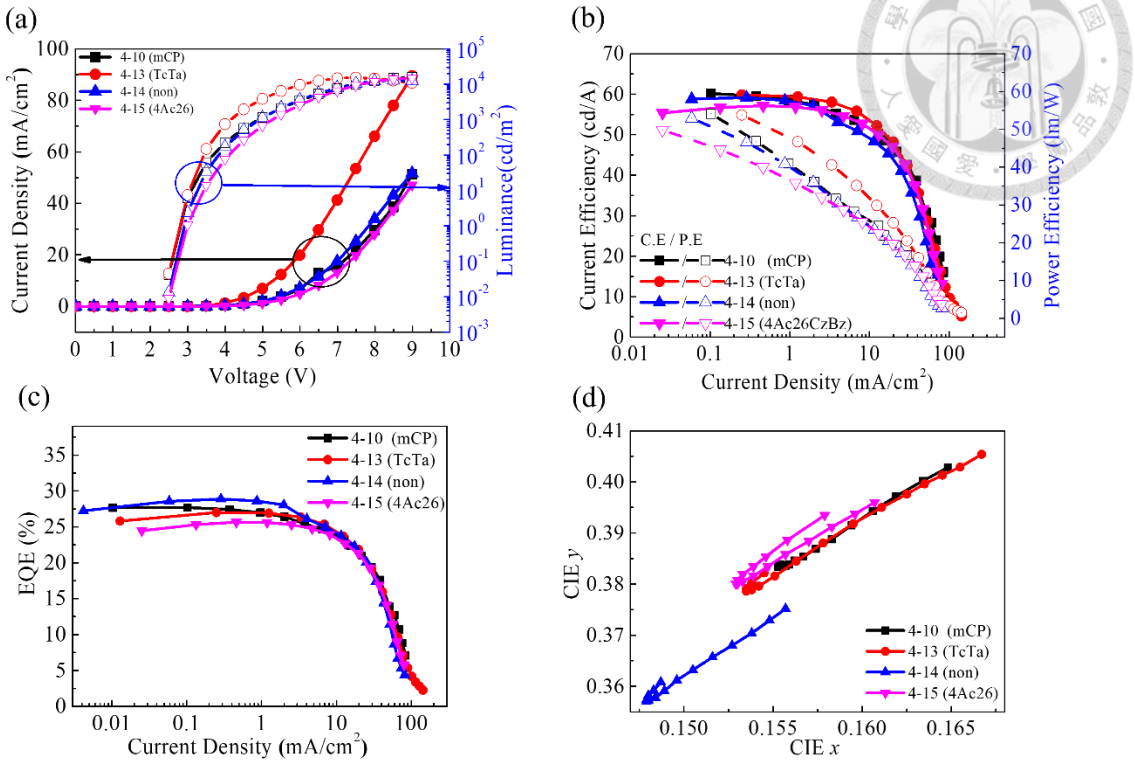

Fig. 4-30 (a) J-L-V curves, (b) current efficiency and power efficiency versus J, (c) EQE versus J, and (d) CIE coordinates at different voltages.

Table 4-14 presented the device performances. Fig. 4-30 (a) displayed the J-L-V curves. Fig. 4-30 (b) and (c) showed the current efficiency, power efficiency, and EQE at different current densities. Device 4-10 showed the maximum current efficiency and maximum power efficiency of 60.6 cd/A and 63.2 lm/W, respectively, while device 4-14 showed the maximum EQE of 28.9%. Fig. 4-30 (d) depicted the CIE coordinates. Device 4-14 had smaller CIE-y values compared to Devices 4-10, 4-13, and 4-15. Fig. 4-32 revealed the TrEL decay curves of devices 4-10, 4-13, 4-14, and 4-15 in 20 μs window, which exhibited delayed emission.

doi:10.6342/NTU202503850

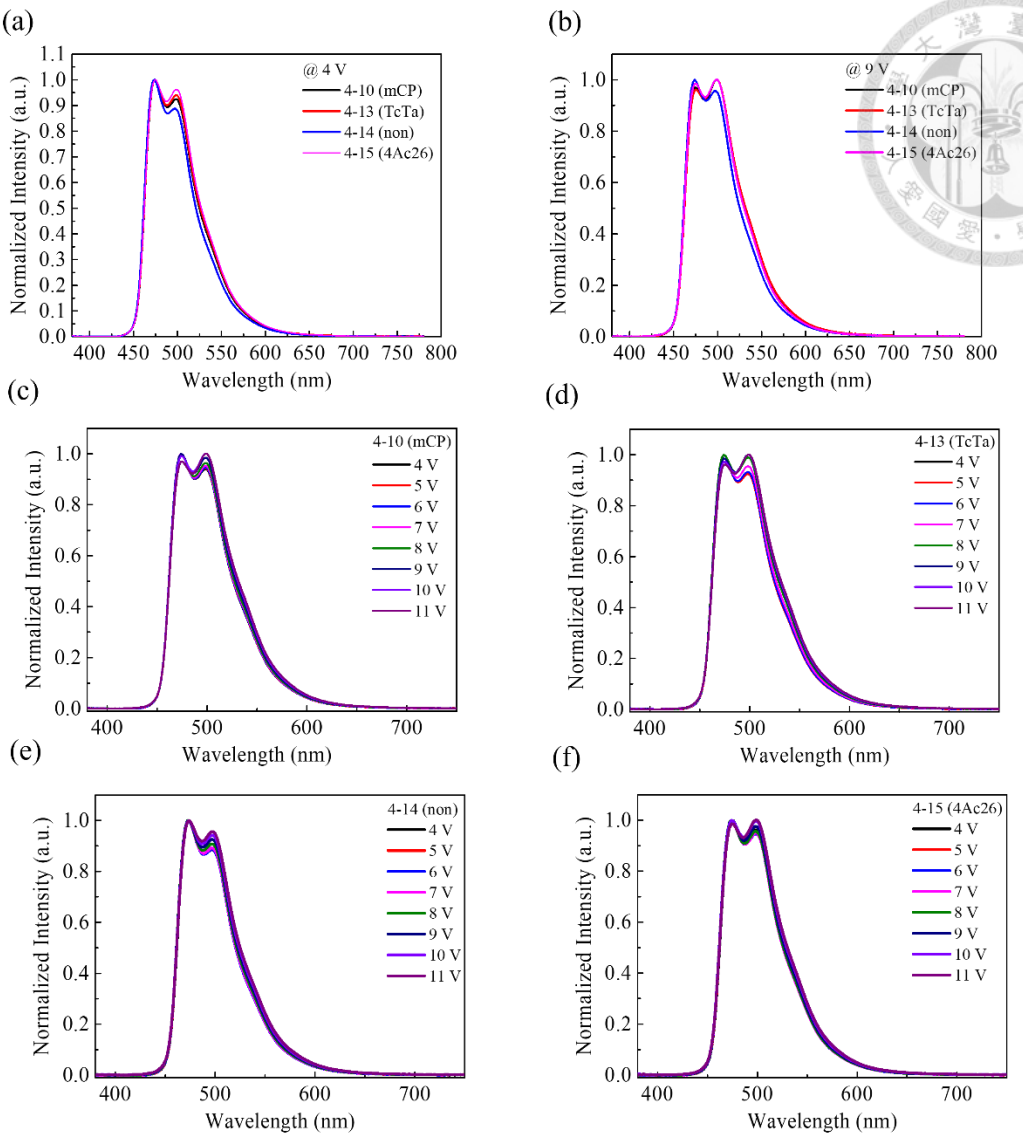

Fig. 4-31 EL spectra of devices (a) 4-10, 4-13, 4-14 and 4-15 with 4 V (b) 4-10, 4-13, 4-14 and 4-15 with 9 V (c) 4-10, (d)4-13, (e) 4-14, and (f) 4-15 with different voltages.

doi:10.6342/NTU202503850

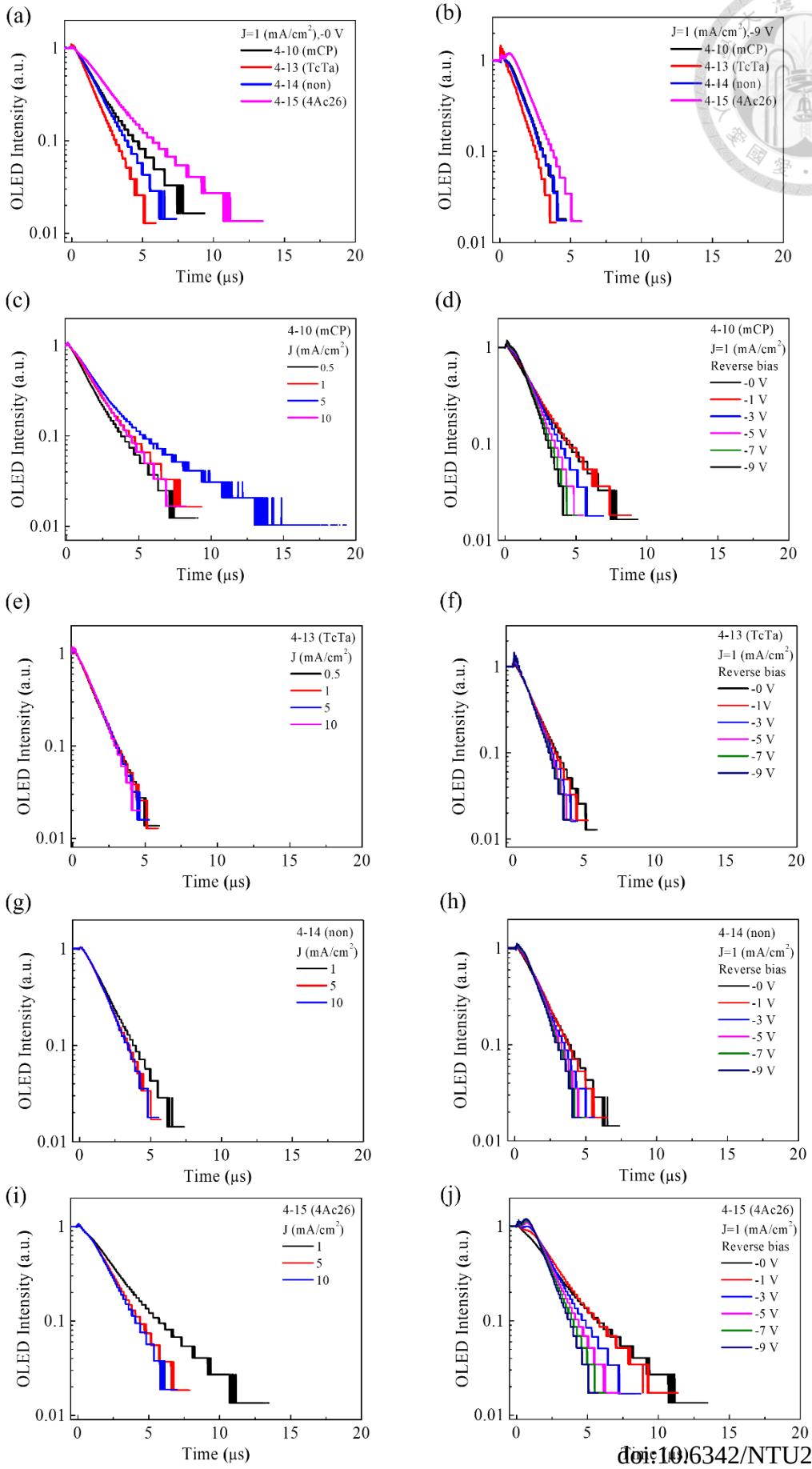

doi:10.6342/NTU202503850

Fig. 4-32 TrEL of devices (a) 4-10, 4-13, 4-14 and 4-15 with J = 1 mA/cm^2,(b) 4-10, 4-13, 4-14 and 4-15 with J = 1 mA/cm^2, and switched to -9 V after t > 0, (c) 4-10 with different current densities, (d) 4-10 with different reverse bias after t > 0, (e) 4-13 with different current densities, (f) 4-13 with different reverse bias after t > 0, (g) 4-14 with different current densities, (h) 4-14 with different reverse biases after t > 0, (i) 4-15 with different current densities, and (j) 4-15 with different reverse bias after t > 0.

4.6 References

[1] Zhang, D., Cai, M., Zhang, Y., Zhang, D., Duan, L., High-efficiency OLEDs based on TADF materials, *Mater. Horiz.* 3 (2016) 145–151.

[2] Li, Y.Z., Liang, H.C., Chen, C.H., Chiu, C.H., Huang, L.C., Lee, Y.T., Dzeng, Y.C., Chen, C., Lin, B.Y., Lee, J.H., Chiu, T.L., Leung, M.K., TADF-assisted charge-transfer materials for efficient OLEDs, *Chem. Eng. J.* 498 (2024) 155553.

[3] Chen, C.H., Lin, S.C., Lin, B.Y., Li, C.Y., Kong, Y.C., Chen, Y.S., Fang, S.C., Chiu, C.H., Lee, J.H., Wong, K.T., Lin, C.F., Hung, W.Y., Chiu, T.L., Blue TADF OLEDs with improved device performance, *Chem. Eng. J.* 442 (2022) 136292.

[4] Jesuraj, P.J., Jeganathan, K., Synthesis and characterization of organic semiconductors, *RSC Adv.* 5 (2015) 684–689.

doi:10.6342/NTU202503850

Chapter 5 Summary

In chapter 3, high-efficiency sky-blue TADF OLEDs were achieved by using acridine-carbazole-pyrimidine based emitters of 4Ac25CzPy and 4Ac35CzPy. The maximum external quantum efficiencies (EQEs) of 12.4% and 21.2% were obtained by using 4Ac25CzPy and 4Ac35CzPy as emitters doped in o-2CbzBz host, respectively. It was found that 4Ac35CzPy exhibited higher PLQY and device efficiency compared to 4Ac25CzPy, and both emitters showed clear TADF characteristics with long delayed emission.

In chapter 4, high-efficiency blue TADF OLEDs were achieved using a bipolar acridine-carbazole-benzimidazole based host material, 4Ac26CzBz, doped with 4TCzBN emitter. The maximum external quantum efficiency (EQE) reached 35.8% with a low lit-on voltage at luminance of 1 cd/m^2 was 2.9 V, which was attributed to the high PLQY (98.6%), bipolar carrier transport, and horizontal dipole orientation of 4Ac26CzBz.

doi:10.6342/NTU202503850

Appendix

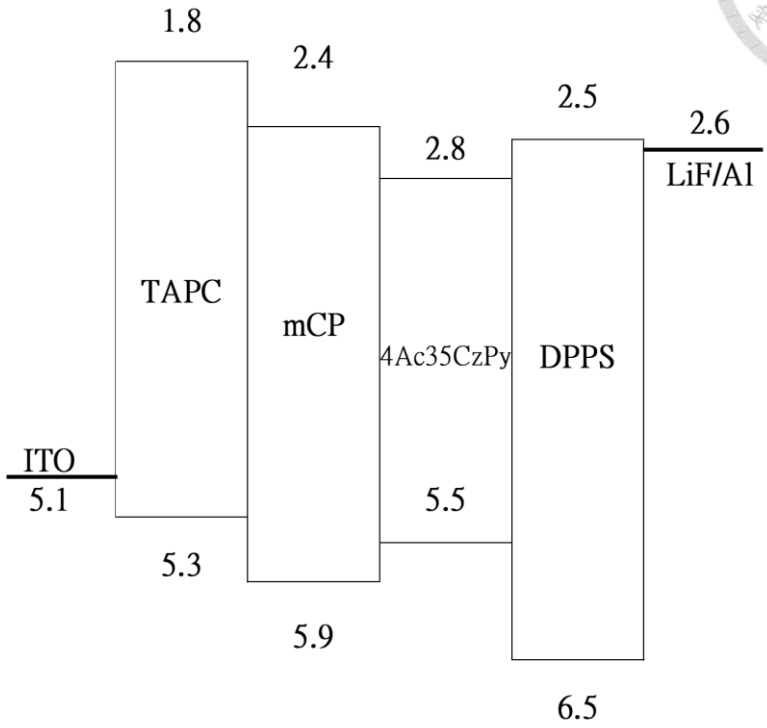

Fig. 0-1 Energy diagram of OLEDs with 4Ac35CzPy emitter.

Table 0-1 Device structure of TADF OLED with 4Ac35CzPy emitter.

Device	HTL	EBL	EML	ETL	EIL/cathode
	TAPC	mCP	4Ac35CzPy	DPPS	LiF/Al
	50	10	30	55	0.8/120

unit: nm

Table 0-2 OLEDs performances of device.

Device	**Voltage[a] (V)**	**Max. Luminance (cd/m^2)**	**CE[b] (cd/A)**	**PE[b] (lm/W)**	**EQE[b] (%)**	**CIE[c] (x,y)**
4Ac35CzPy	7.9/4.9	1252	24.7	15.8	6.6	(0.267,0.543)

[a]at J = 10 mA/cm^2/L= 1 cd/m^2; [b]CE/PE/EQE measured at maximum/100 cd/m^2/1000 cd/m^2; [c]measured at maximum current efficiency.

doi:10.6342/NTU202503850

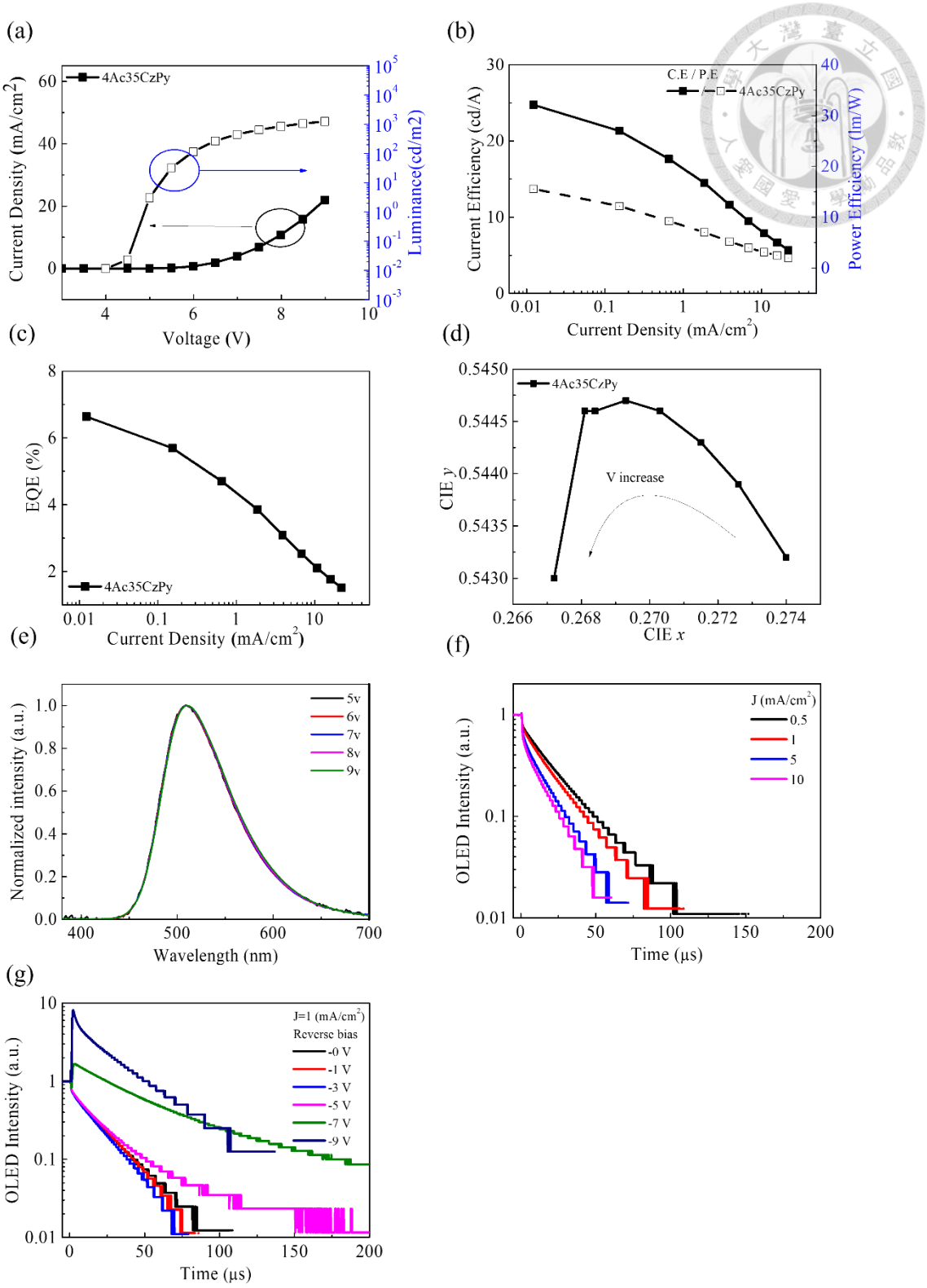

Fig. 0-2 (a) J-L-V curves, (b) current efficiency and power efficiency versus J, (c) EQE versus J, and (d) CIE coordinates at different voltages. (e) EL spectra of devices 4Ac35CzPy with different voltages. (f) TrEL of devices 4Ac35CzPy with different current densities, and (g) 4Ac35CzPy with different reverse bias after $t > 0$.

doi:10.6342/NTU202503850

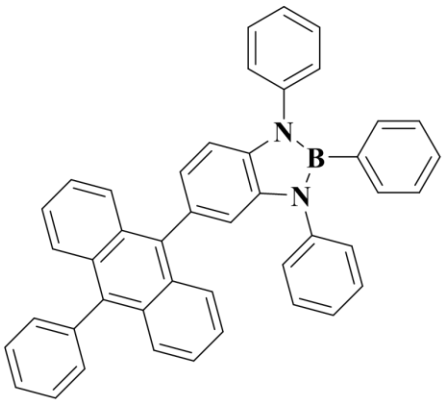

mAn

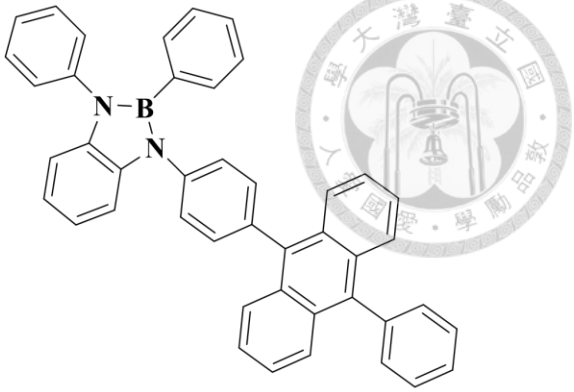

NAn

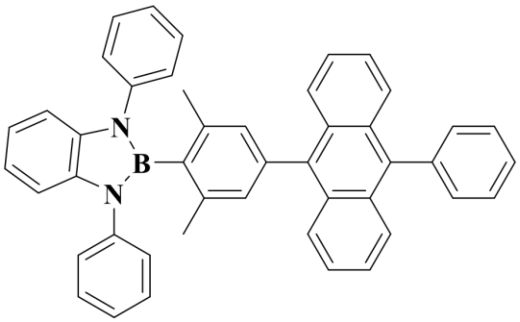

dmBA

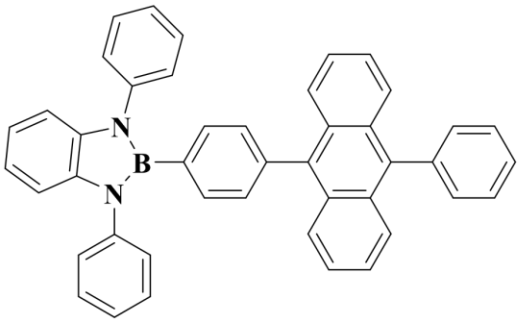

BdpA

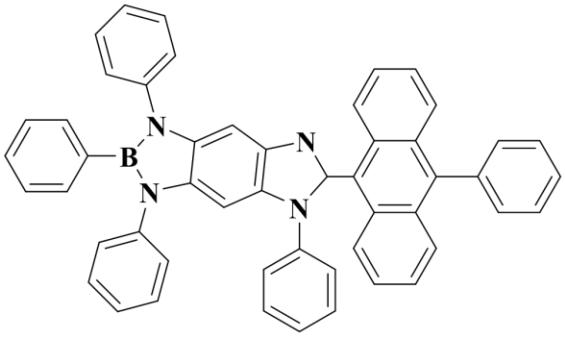

pABIZ

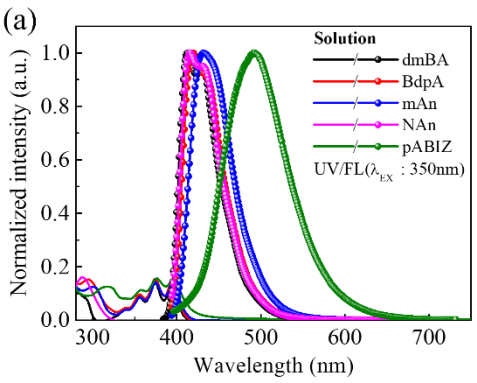

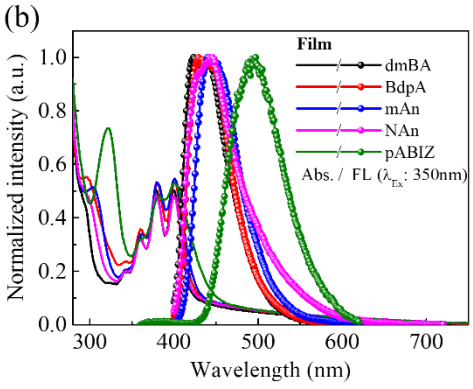

doi:10.6342/NTU202503850

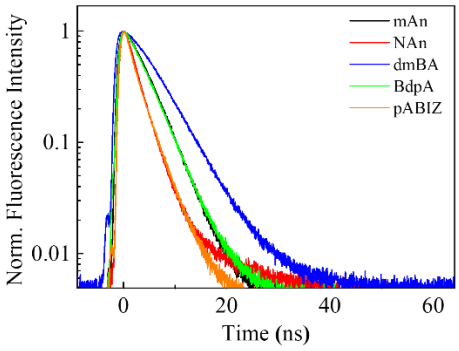

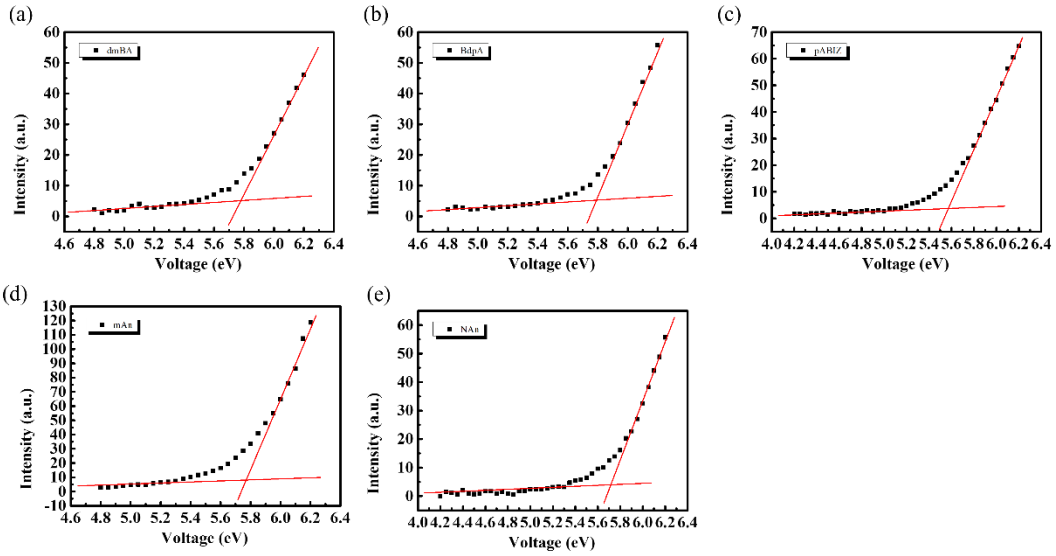

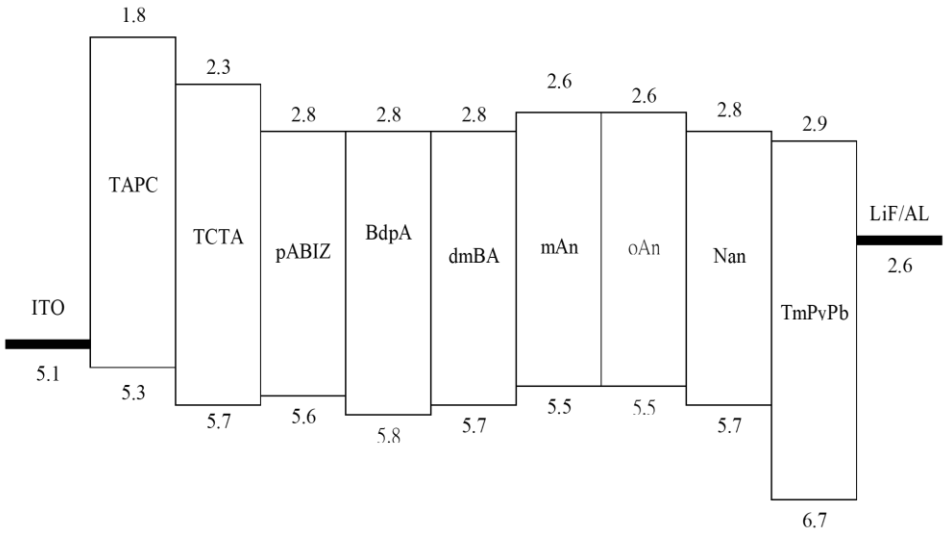

doi:10.6342/NTU202503850

Device	HTL	EBL	EML	ETL	EIL/cathode
	TAPC	*m*CP	EML	DPPS	LiF/Al
BdpA dmBA mAn Nan pABIZ	50	10	17.5	45	1/100
unit: nm					

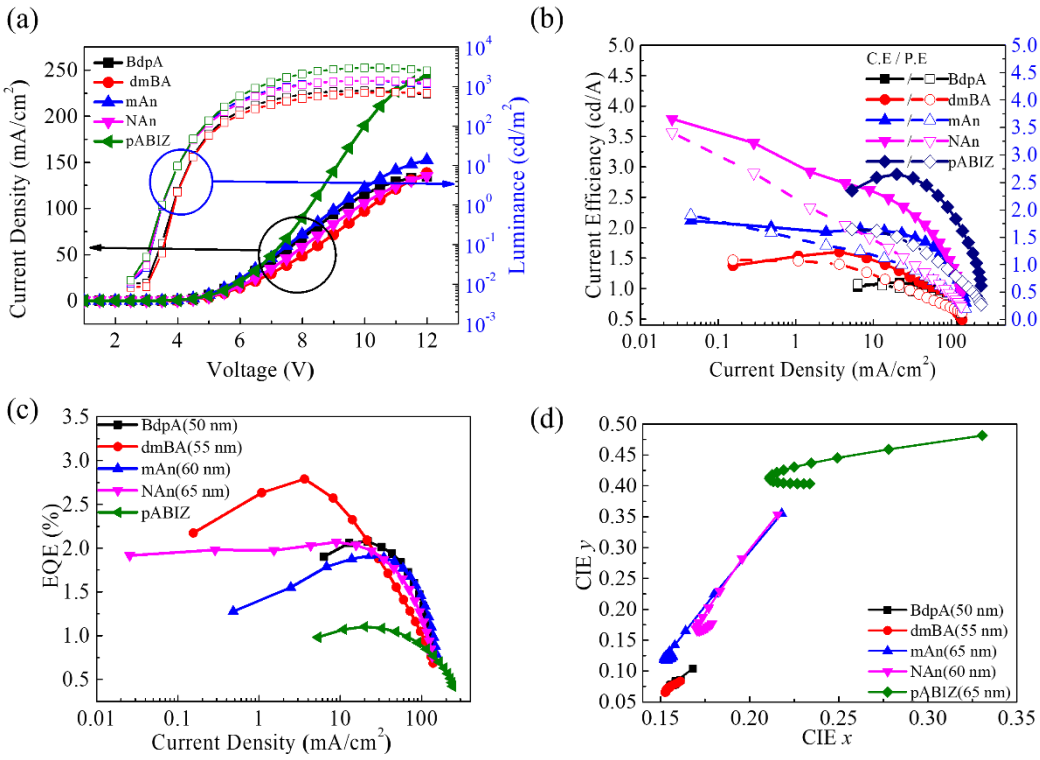

doi:10.6342/NTU202503850

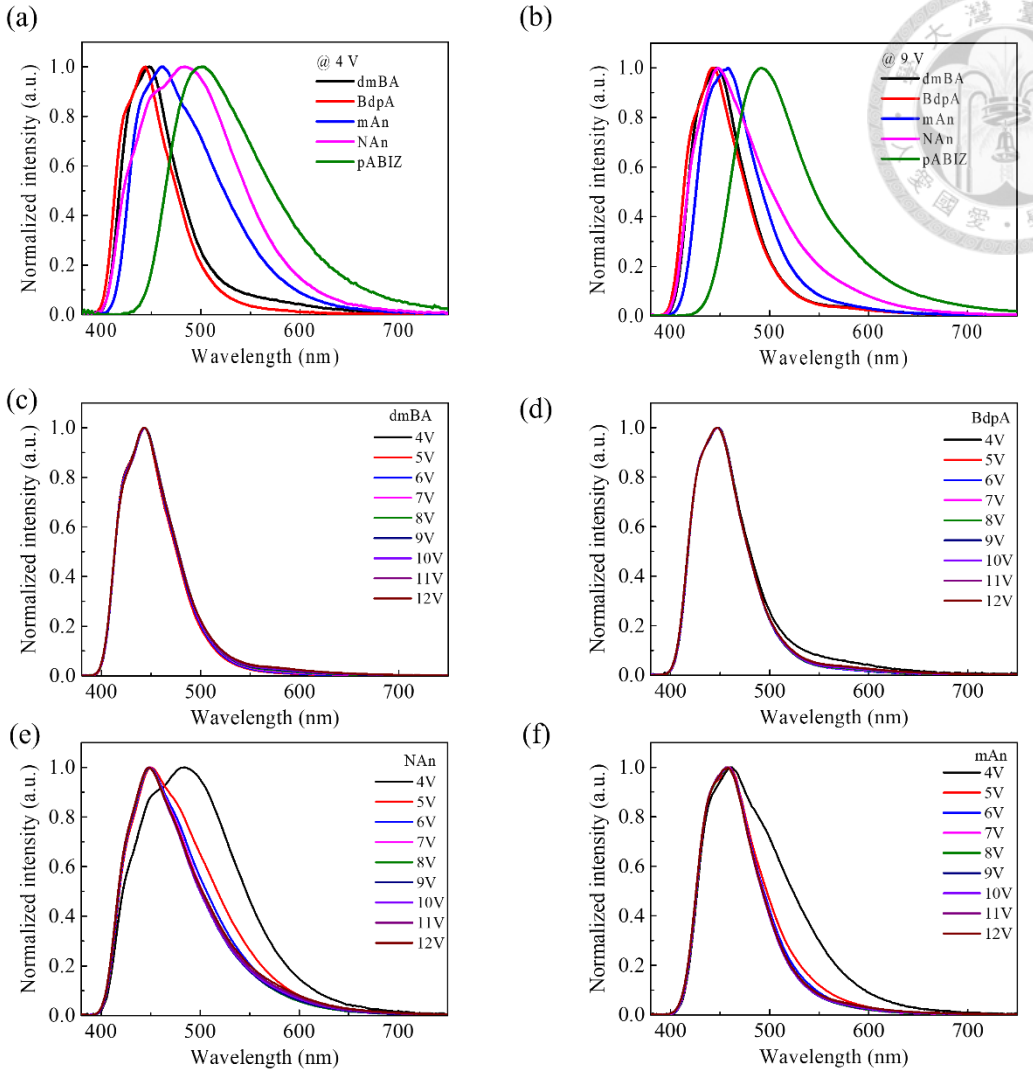

doi:10.6342/NTU202503850

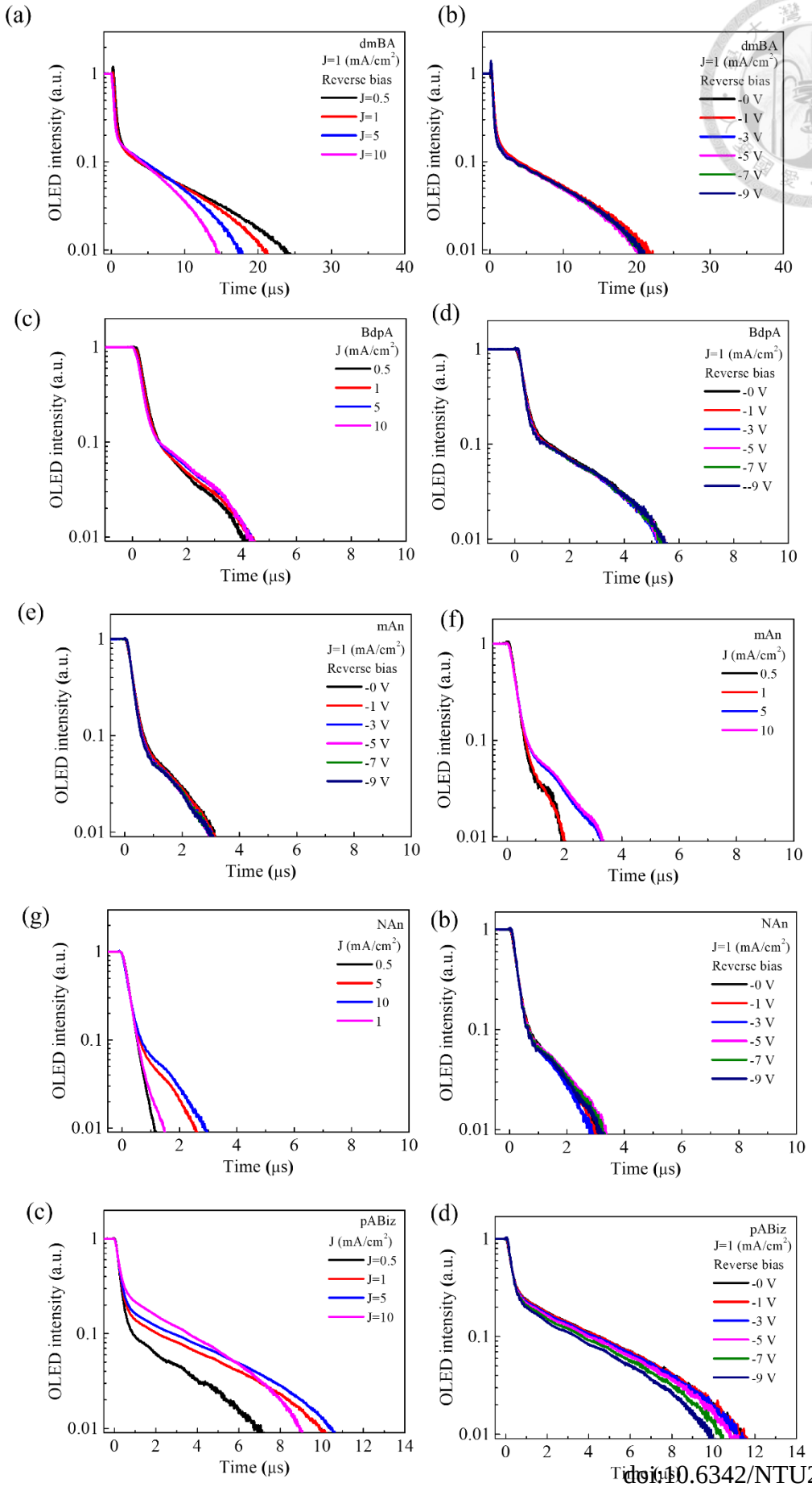

doi:10.6342/NTU202503850

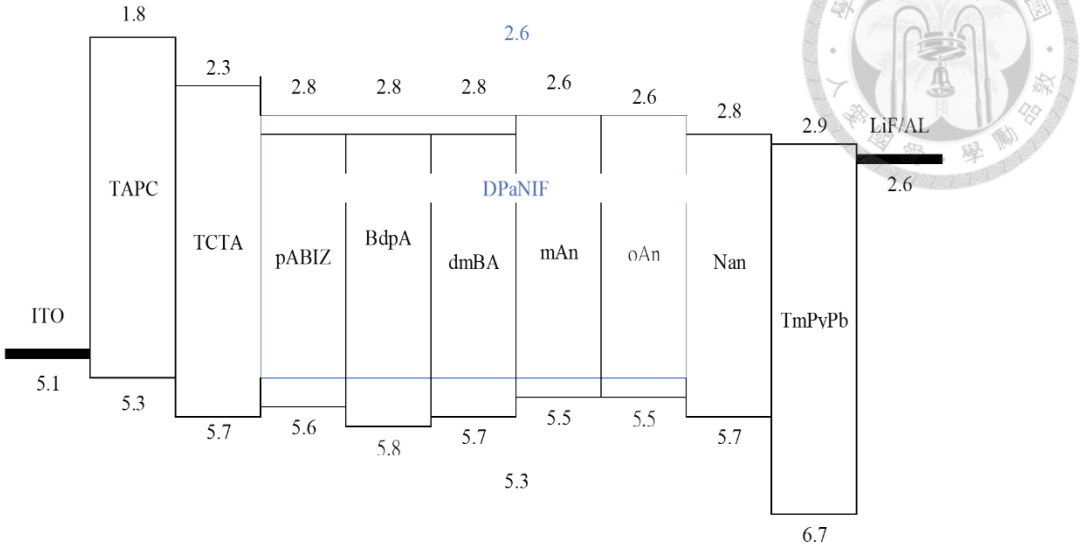

Device	HTL	EBL	EML	ETL	EIL/cathode
	TAPC	*m*CP	HOST:3%DPaNIF	TmPyPb	LiF/Al
BdpA	50	10	27.5	35	0.8/120
dmBA					
NAn			22.5		
mAn					

unit: nm

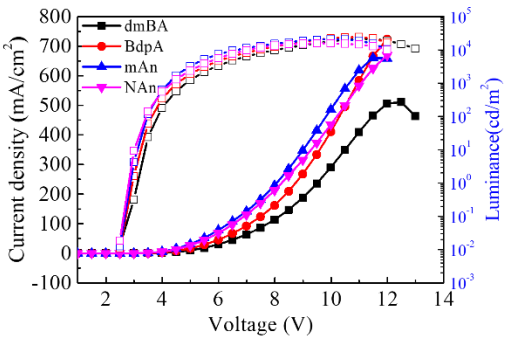

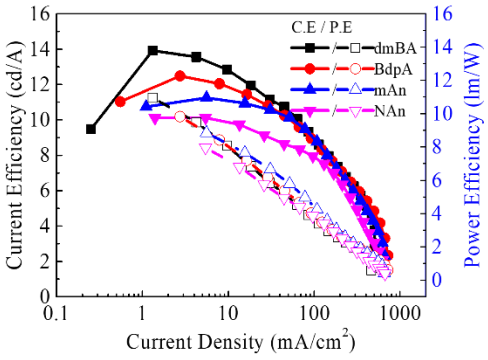

(c)

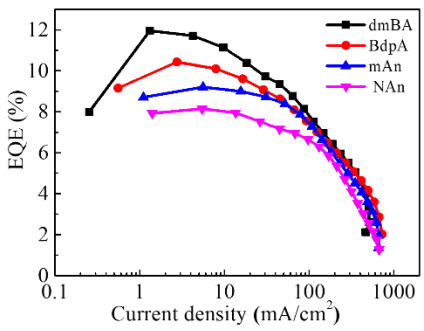

(d)

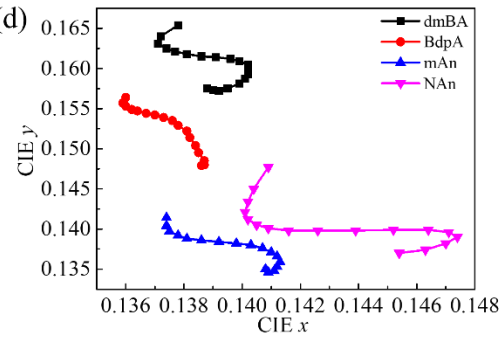

doi:10.6342/NTU202503850

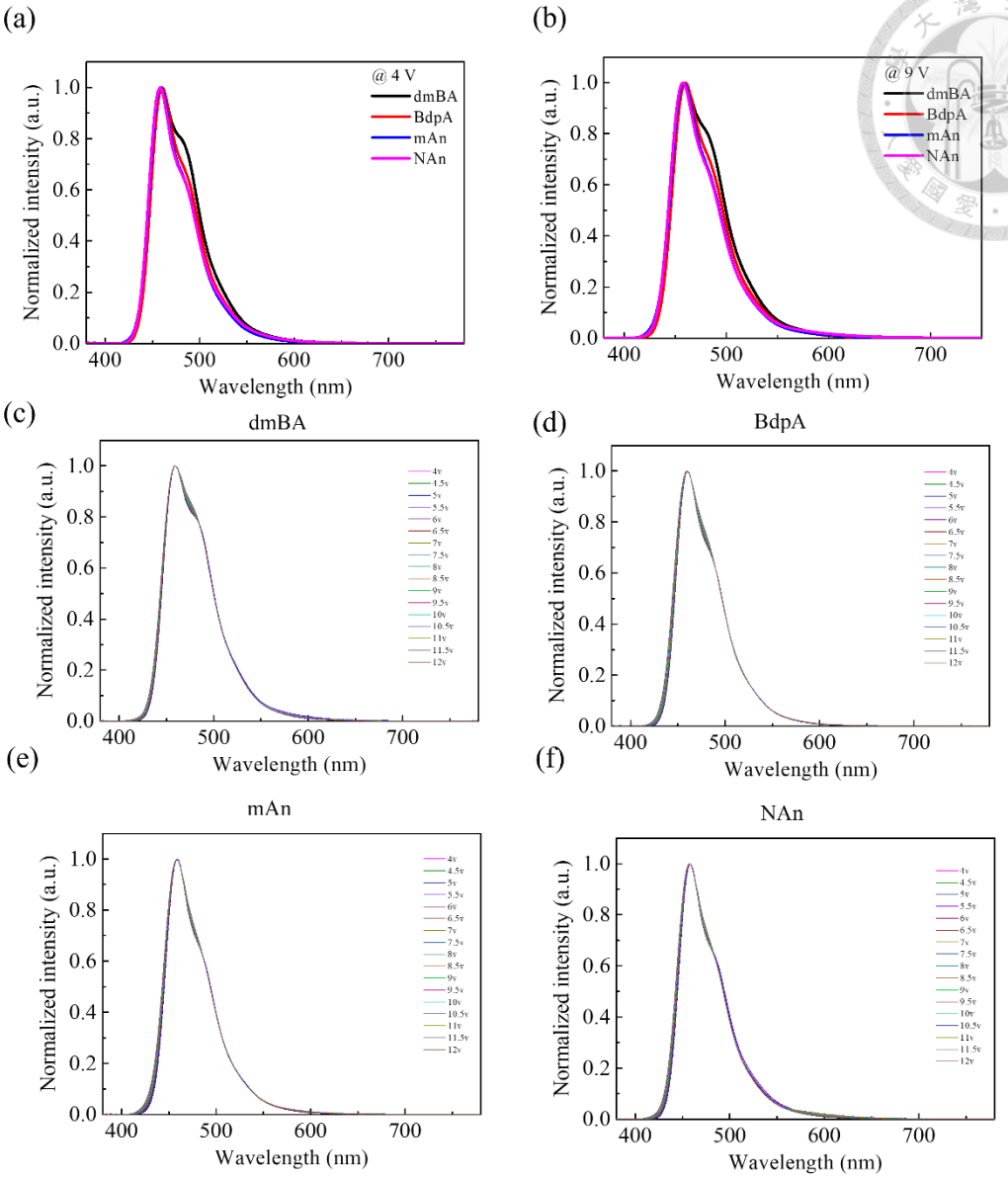

doi:10.6342/NTU202503850

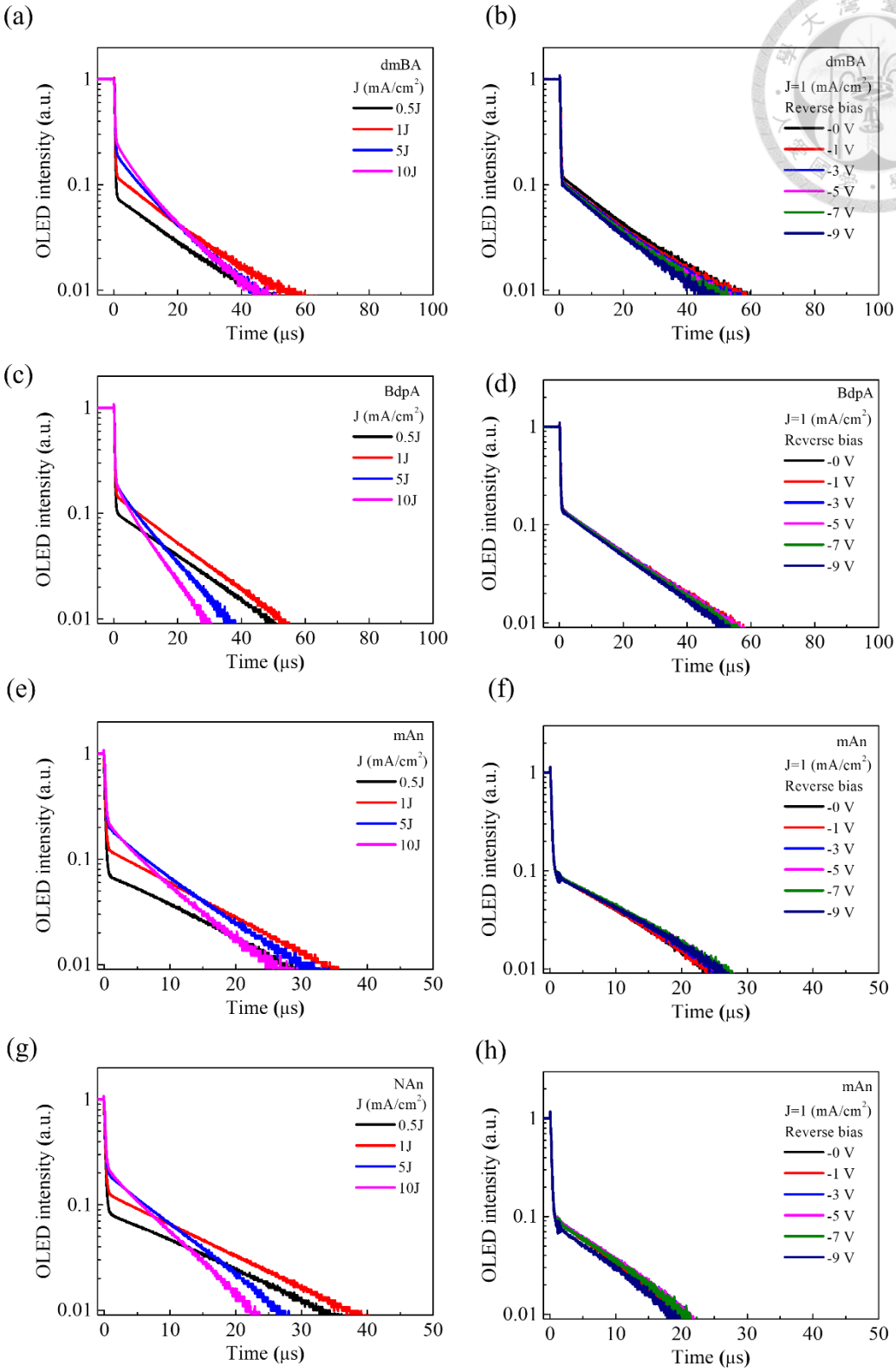

doi:10.6342/NTU202503850

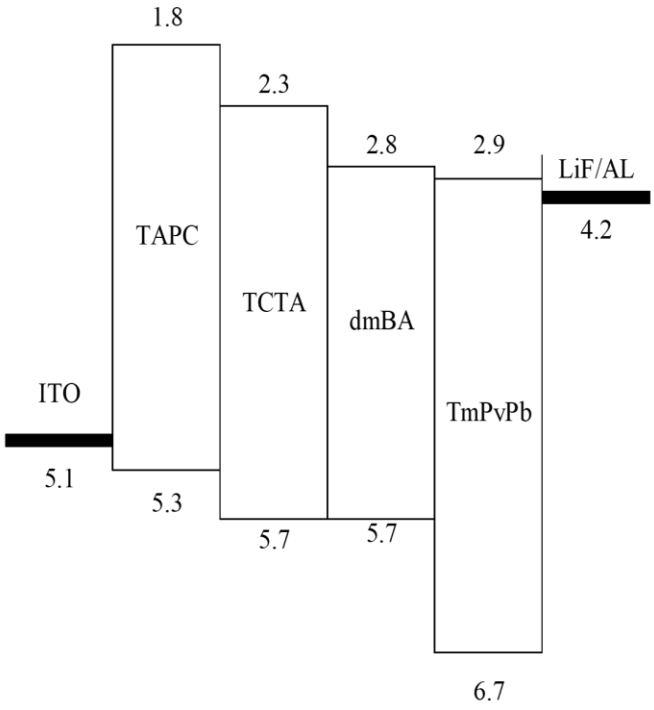

Device	HTL	EBL	EML	ETL	EIL/cathode
	TAPC	*m*CP	dmBA: x%DPaNIF	DPPS	LiF/Al
1%					
3%	40	10	17.5	45	1/100
5%					

unit: nm

doi:10.6342/NTU202503850

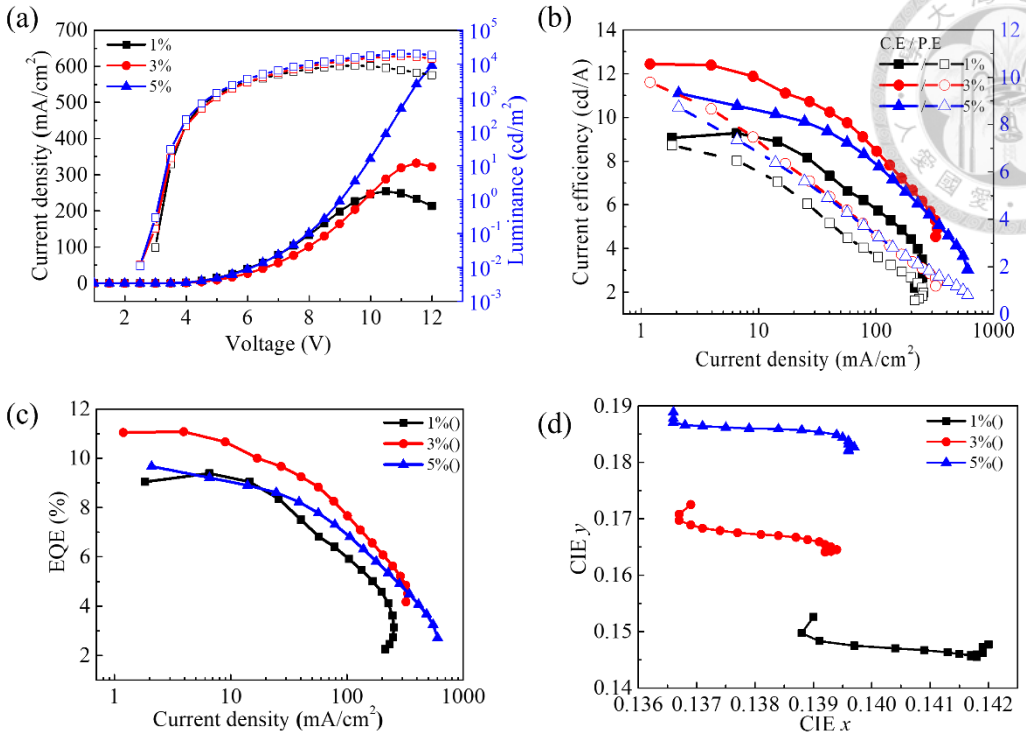

doi:10.6342/NTU202503850

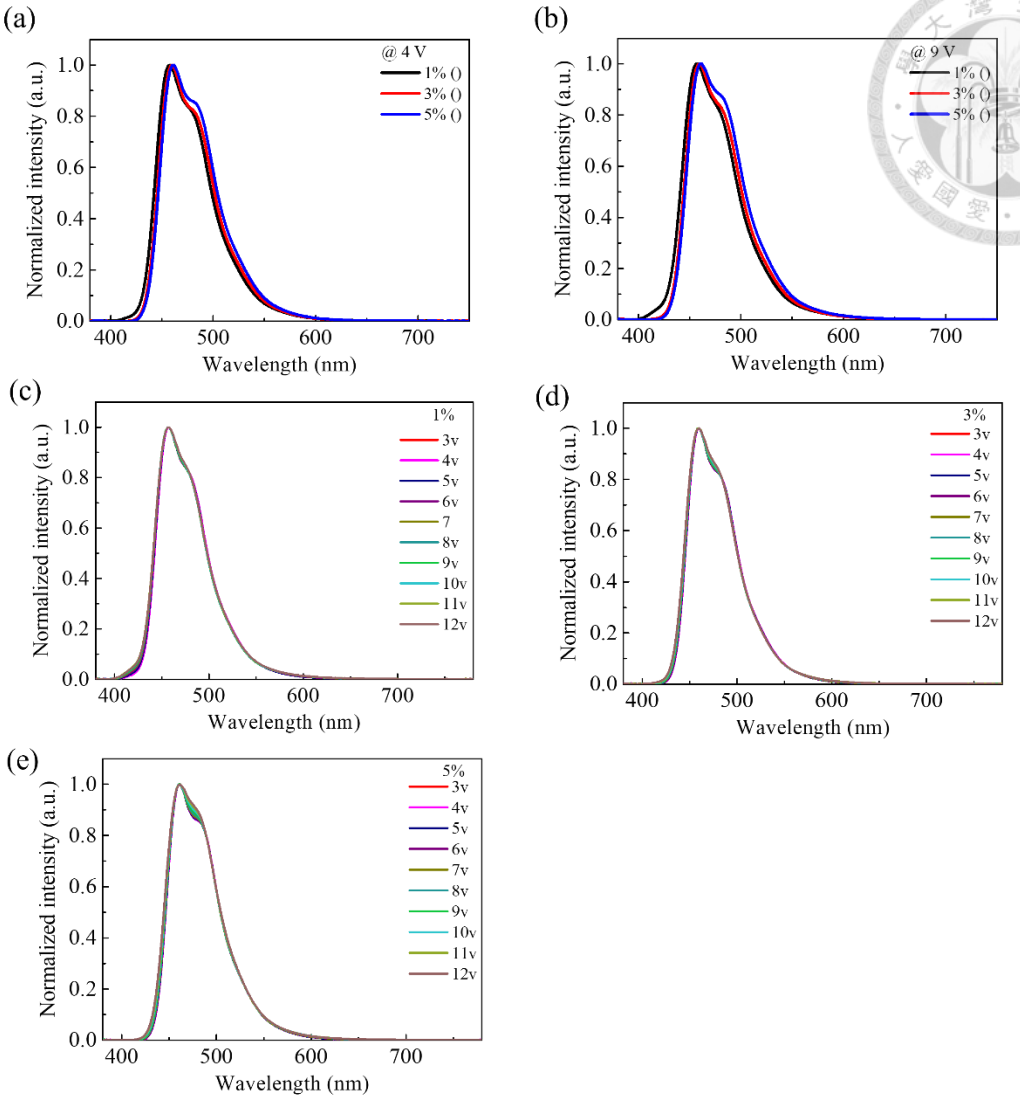

doi:10.6342/NTU202503850

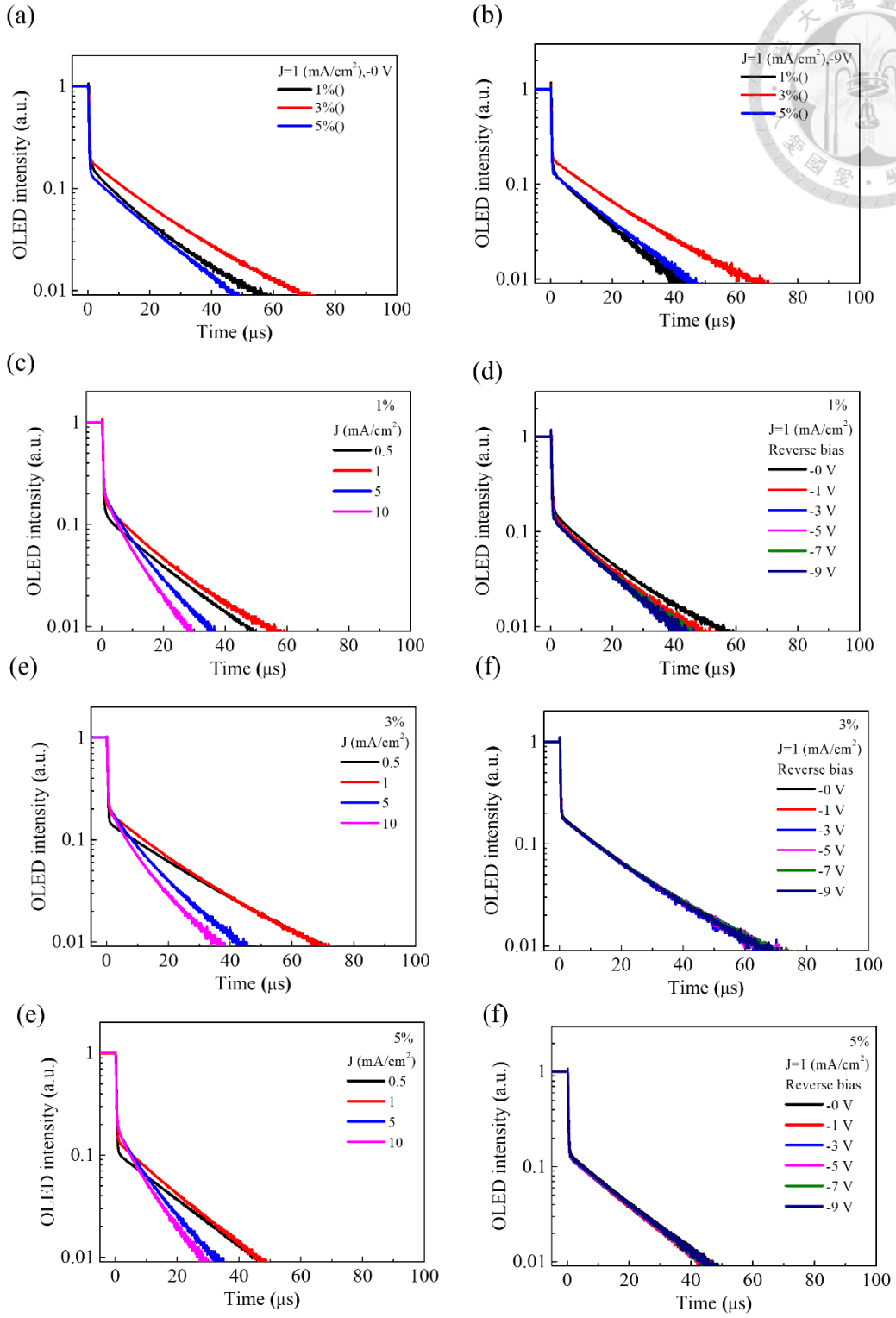

doi:10.6342/NTU202503850

Device	HTL	EBL	EML	ETL	EIL/cathode
	TAPC	*m*CP	dmBA: 3%DPaNIF	DPPS	LiF/Al
	40	10	17.5	30 35 40 35	1/100

unit: nm

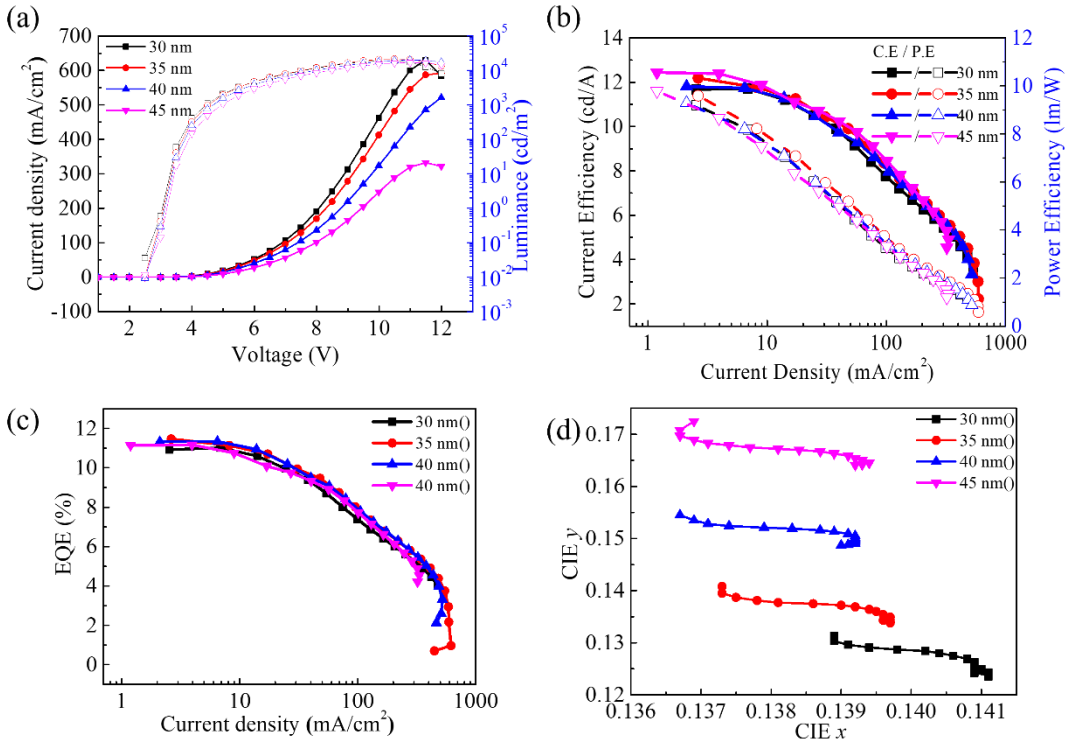

doi:10.6342/NTU202503850

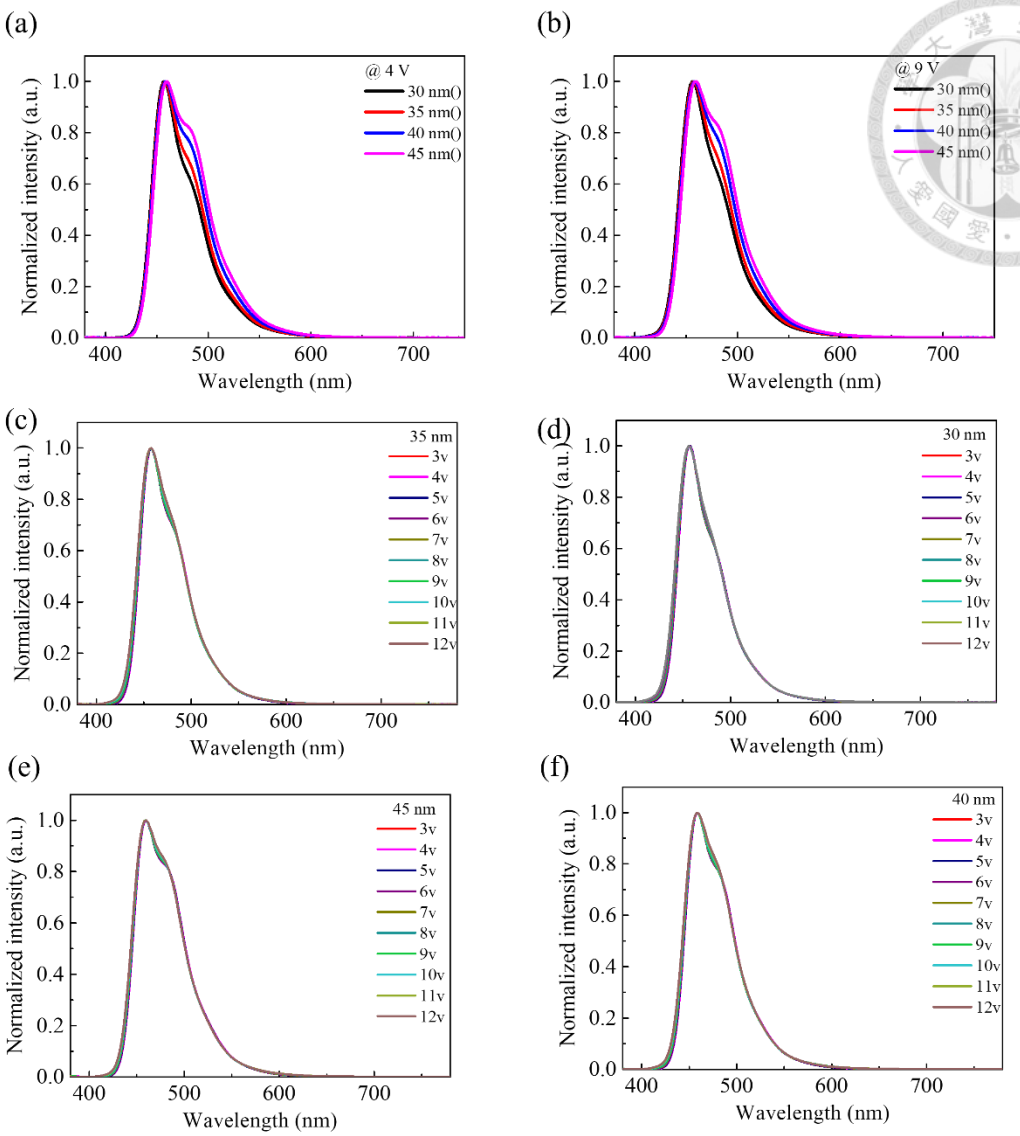

doi:10.6342/NTU202503850

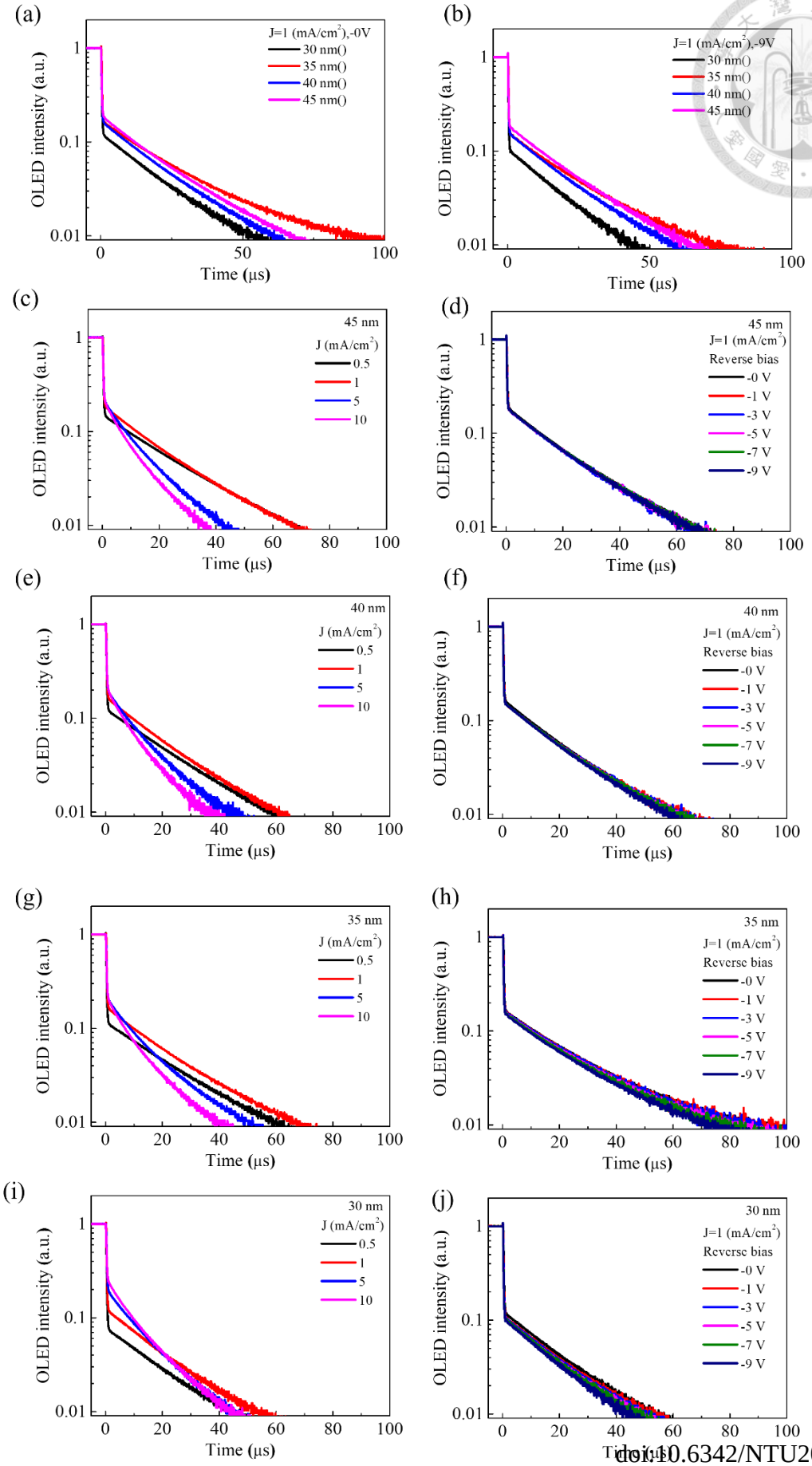

doi:10.6342/NTU202503850

Device	HTL	EBL	EML	ETL	EIL/cathode
	TAPC	*m*CP	dmBA: 3%DPaNIF	DPPS	LiF/Al
	40	10	17.5 22.5 27.5	35	1/100

unit: nm

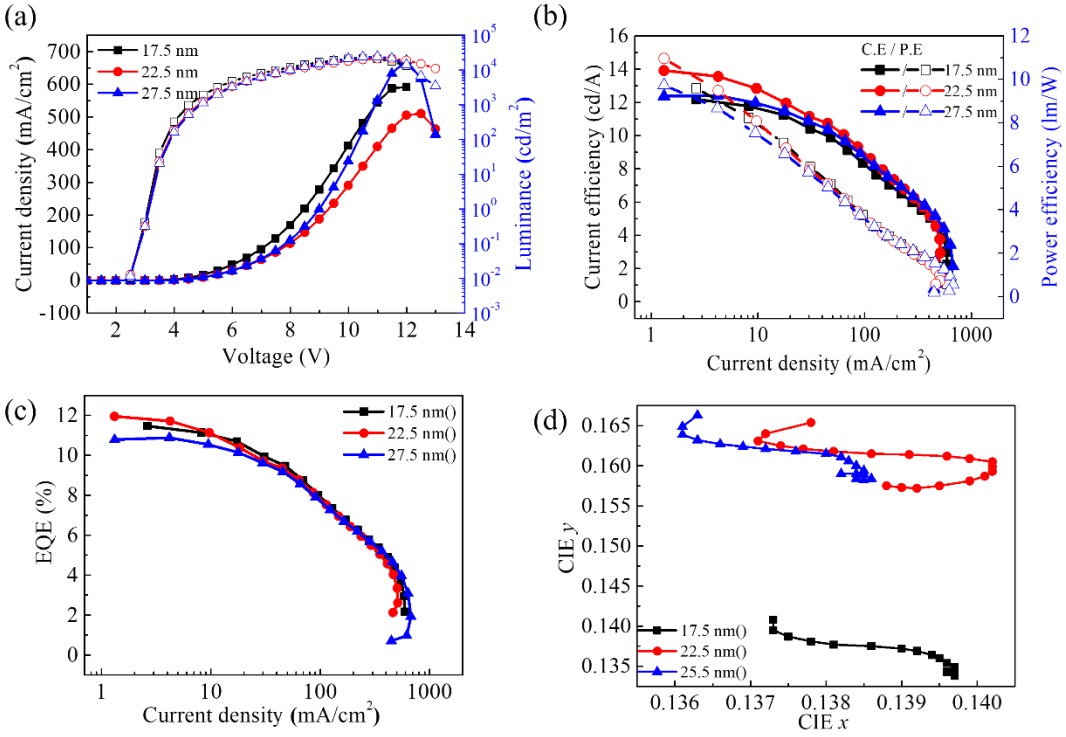

doi:10.6342/NTU202503850

(a)

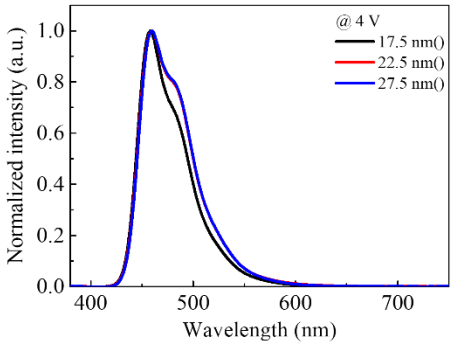

(b)

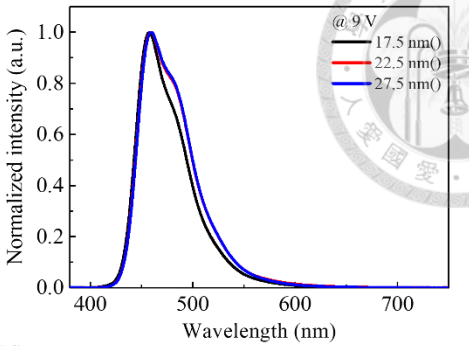

(c)

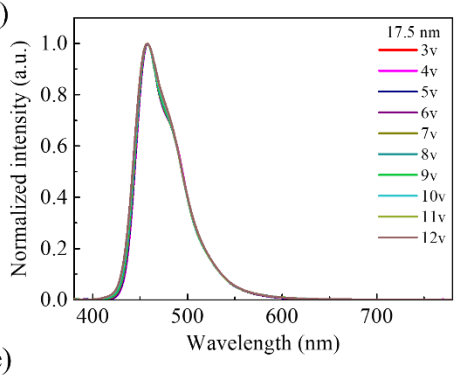

(d)

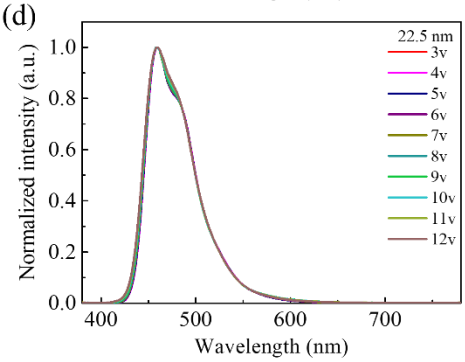

(e)

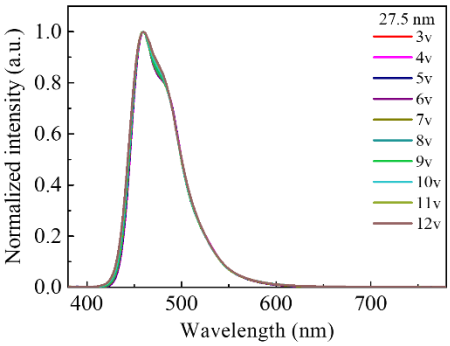

doi:10.6342/NTU202503850

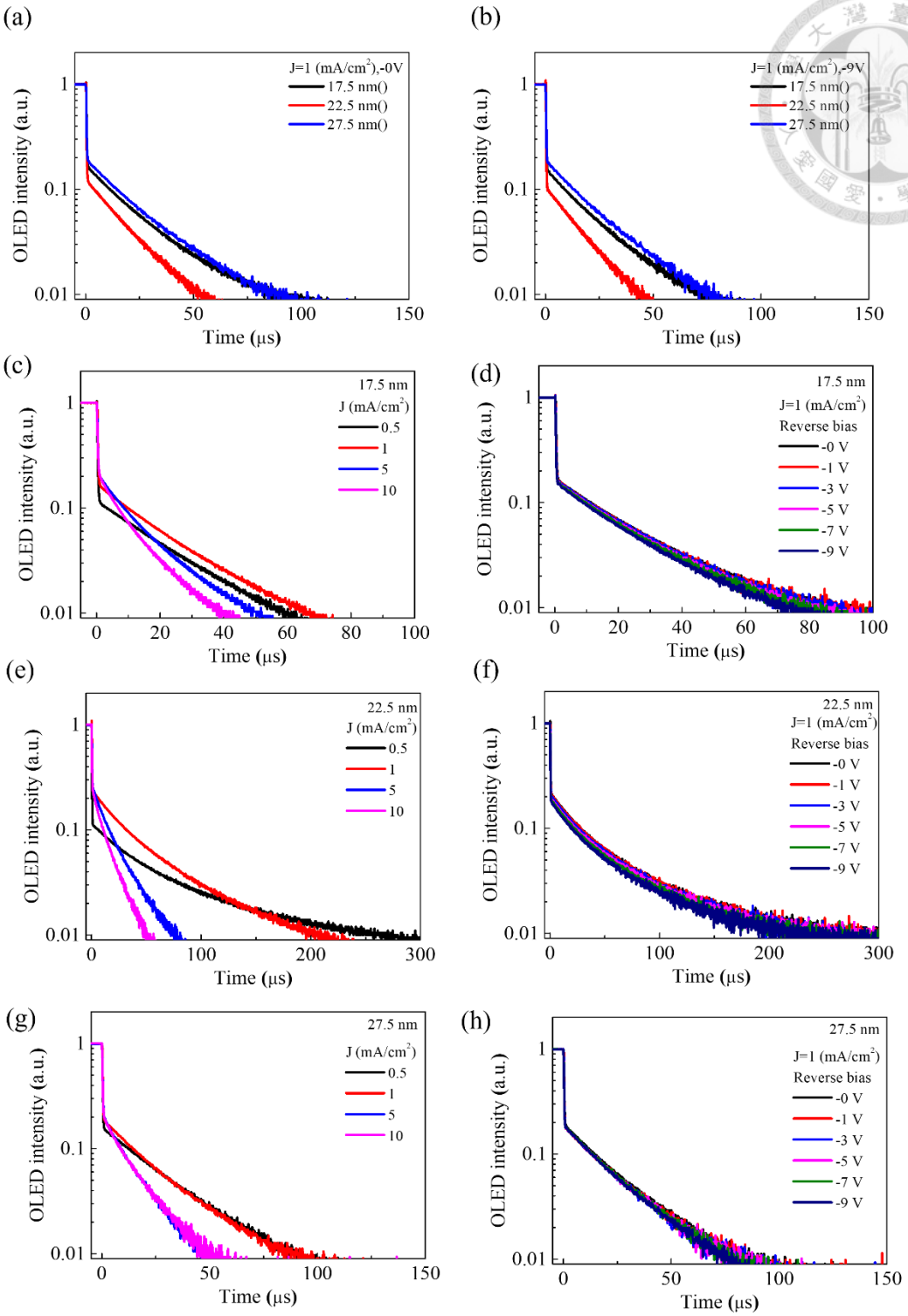

doi:10.6342/NTU202503850

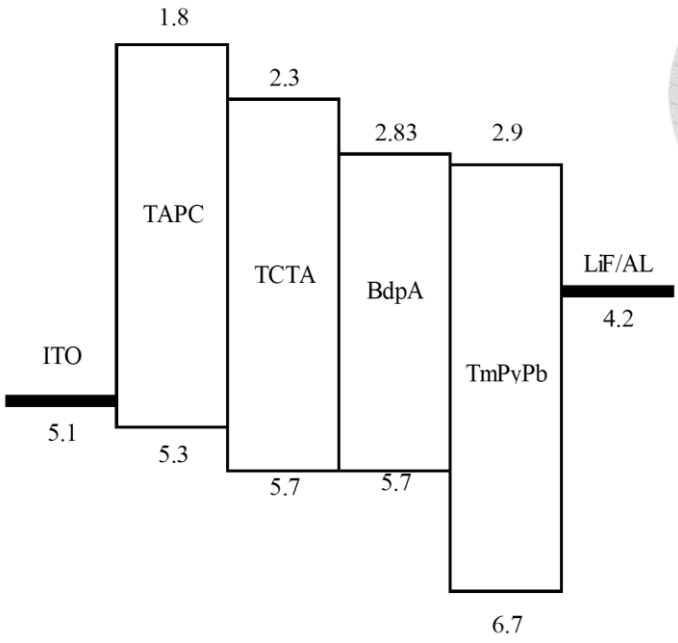

Device	HTL	EBL	EML	ETL	EIL/cathode
	TAPC	*m*CP	BdpA: X%DPaNIF	DPPS	LiF/Al
3%					
5%	40	10	22.5	35	1/100
7%					

unit: nm

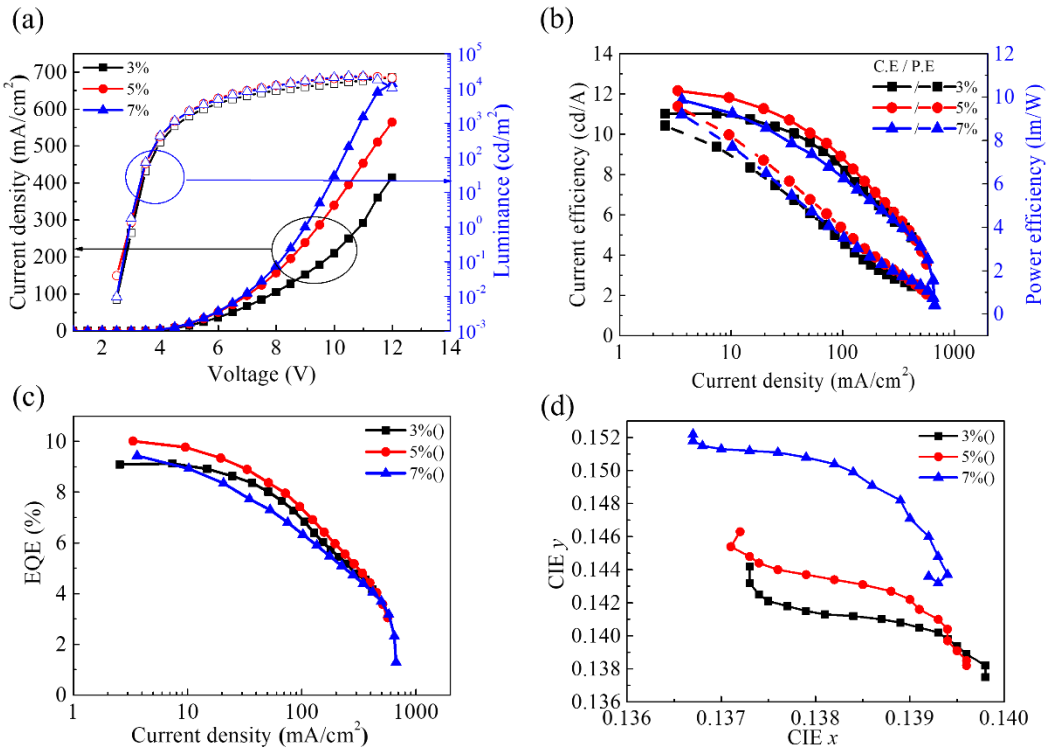

doi:10.6342/NTU202503850

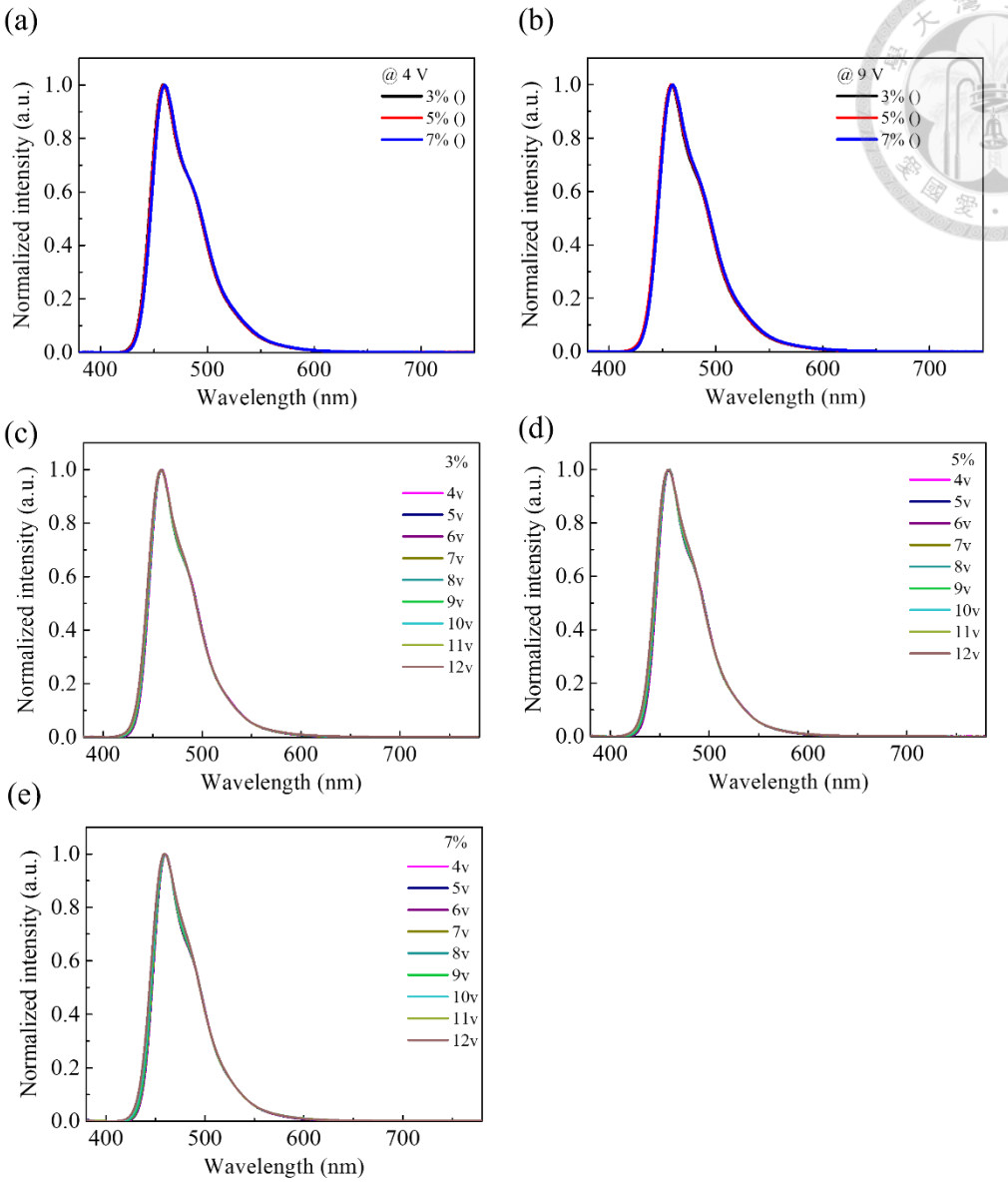

doi:10.6342/NTU202503850

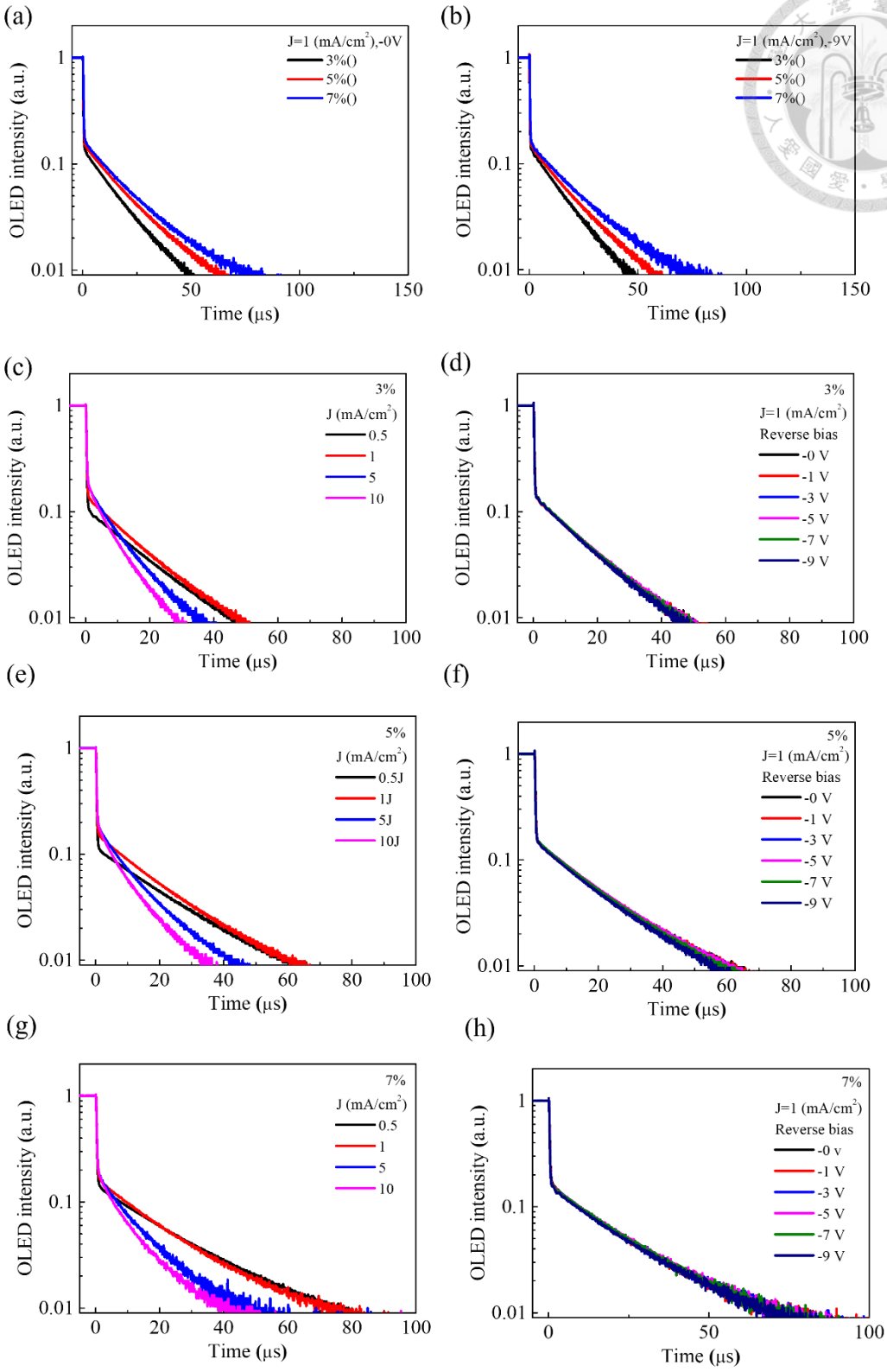

doi:10.6342/NTU202503850

Device	HTL	EBL	EML	ETL	EIL/cathode
	TAPC	*m*CP	BdpA: 5%DPaNIF	DPPS	LiF/Al
30 35 40	40	10	22.5	Device	1/100

unit: nm

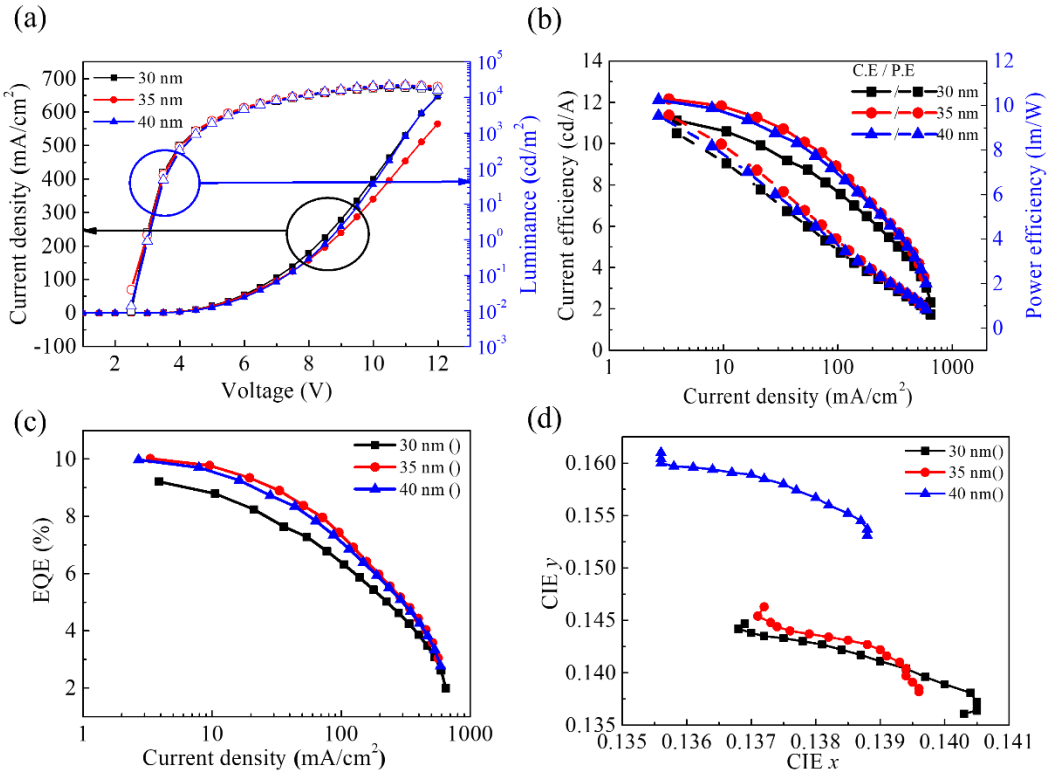

doi:10.6342/NTU202503850

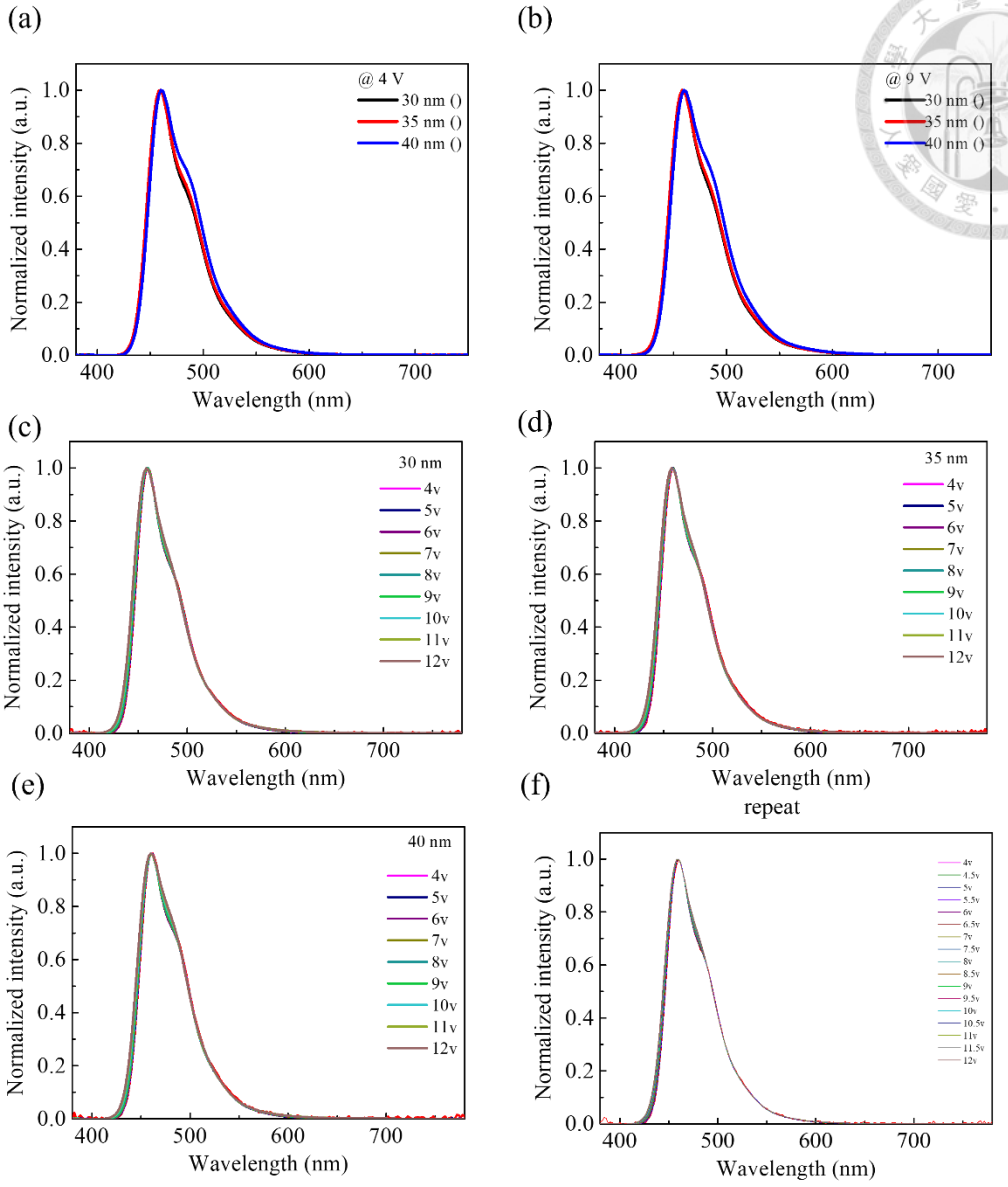

doi:10.6342/NTU202503850

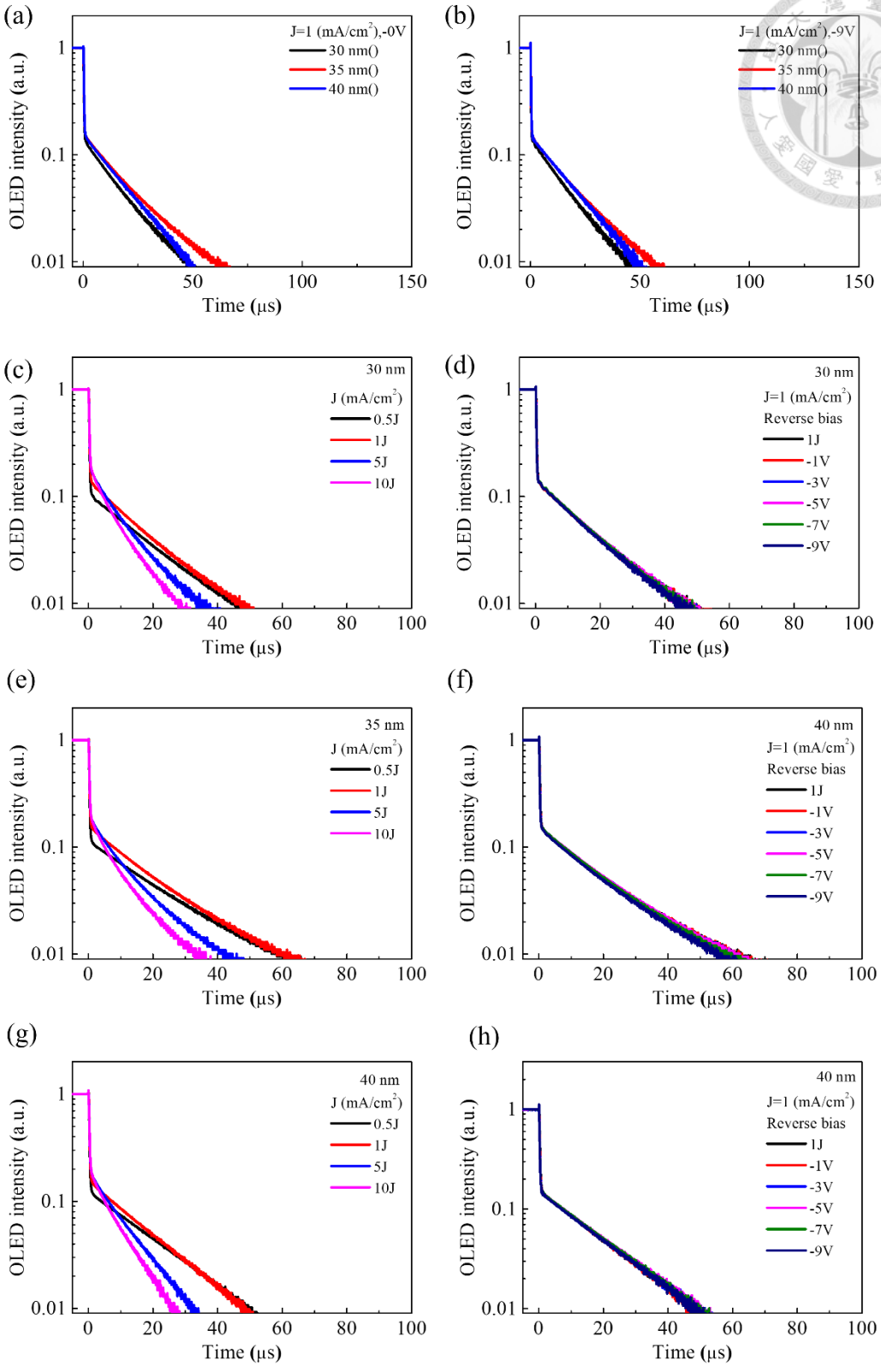

doi:10.6342/NTU202503850

Device	HTL	EBL	EML	ETL	EIL/cathode
	TAPC	*m*CP	BdpA: 5%DPaNIF	DPPS	LiF/Al
17.5 22.5 27.5 32.5	40	10	Device	35	1/100

unit: nm

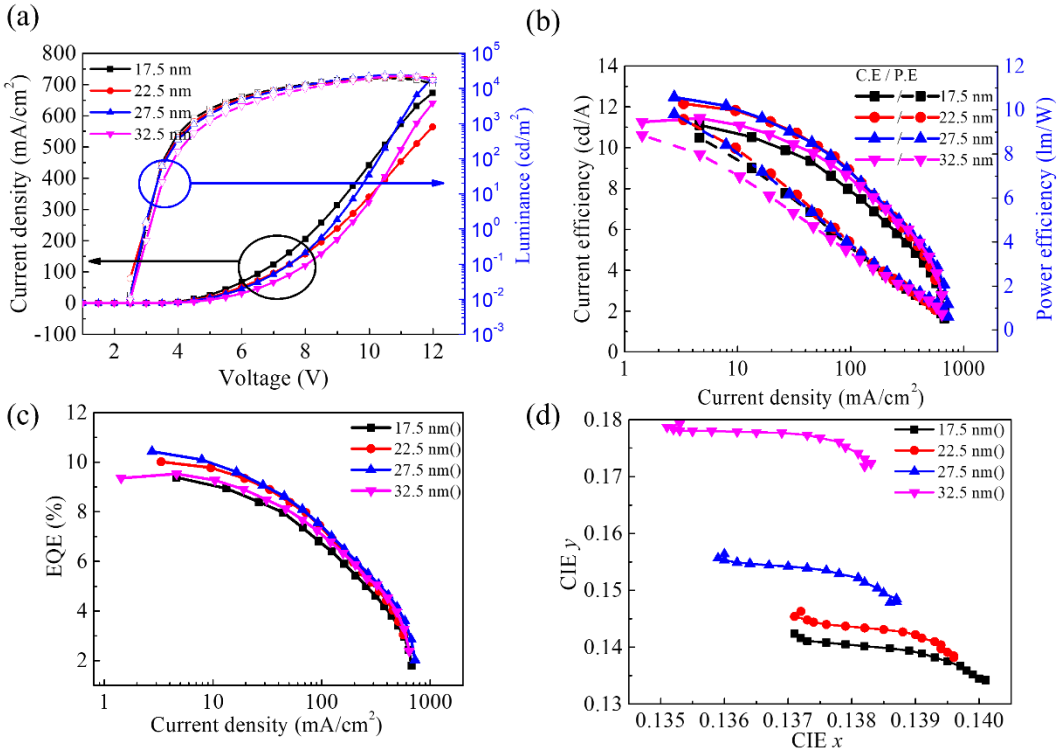

doi:10.6342/NTU202503850

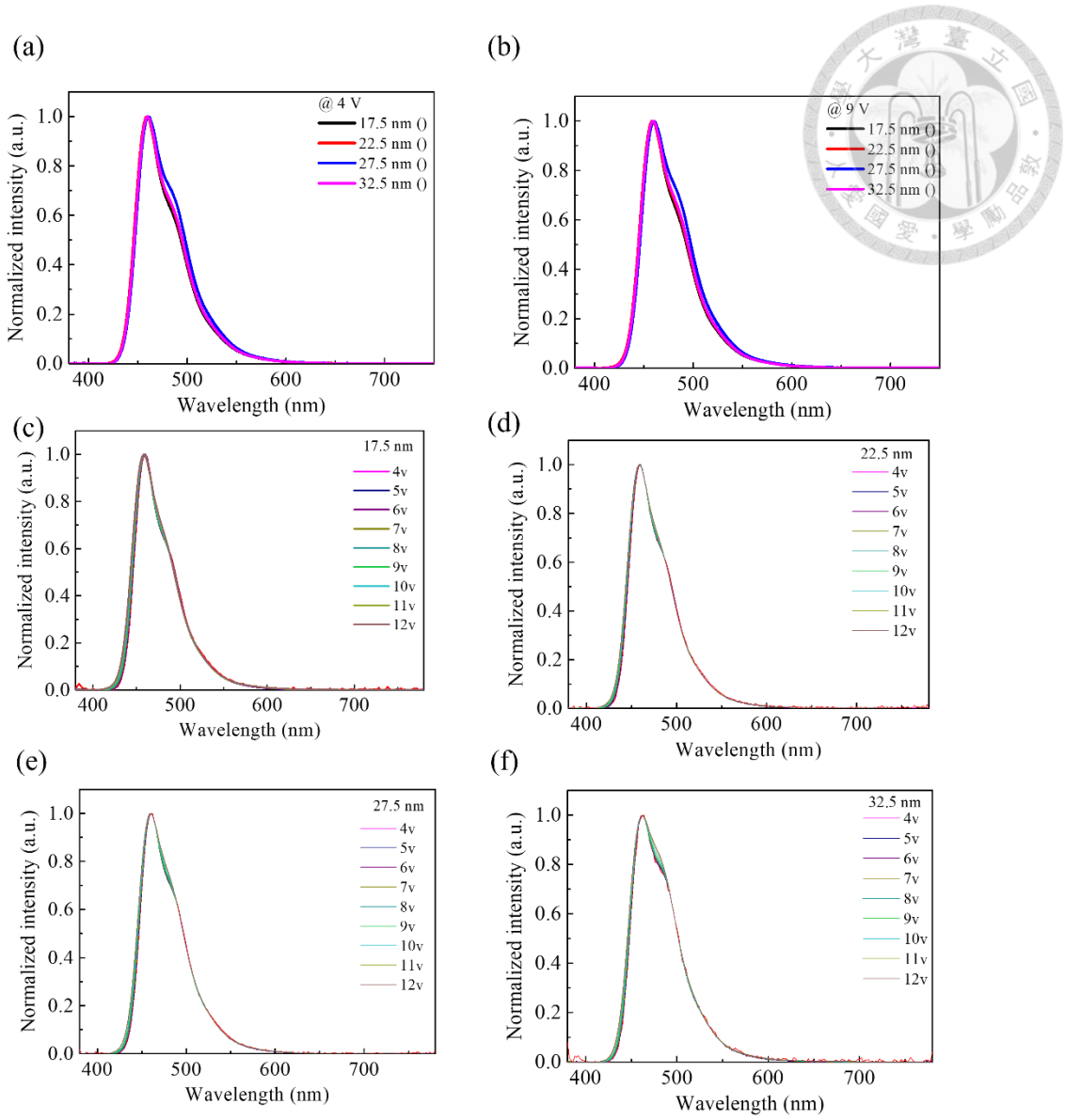

doi:10.6342/NTU202503850

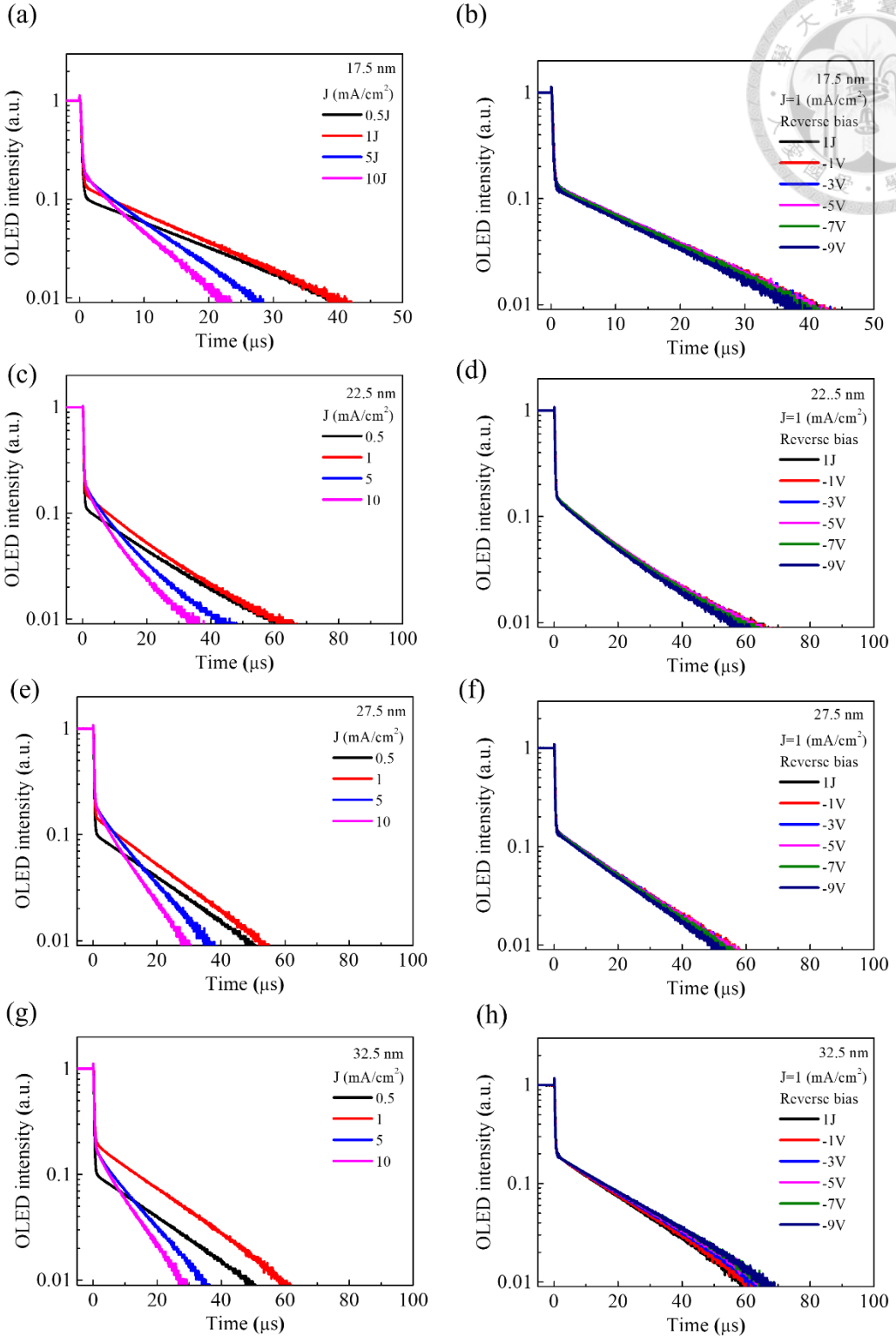

doi:10.6342/NTU202503850

Device	HTL	EBL	EML1	EML2	ETL	EIL/cathode
	TAPC	TCTA	DMPPP: 5%WBD732	dmBA: 3%WBD732	TmPyPb	LiF/Al
	40	10	5	22.5	35	1/100
				17.5	45	
				22.5		

unit: nm

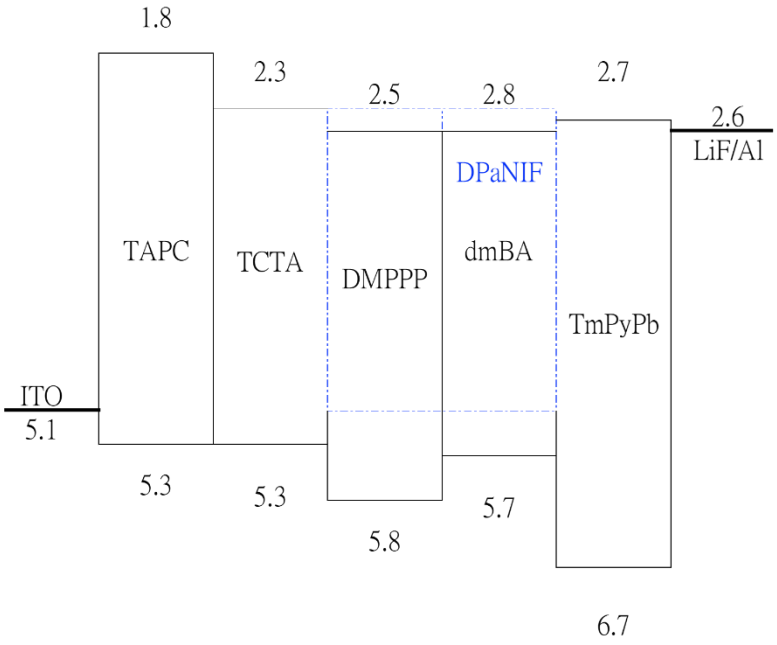

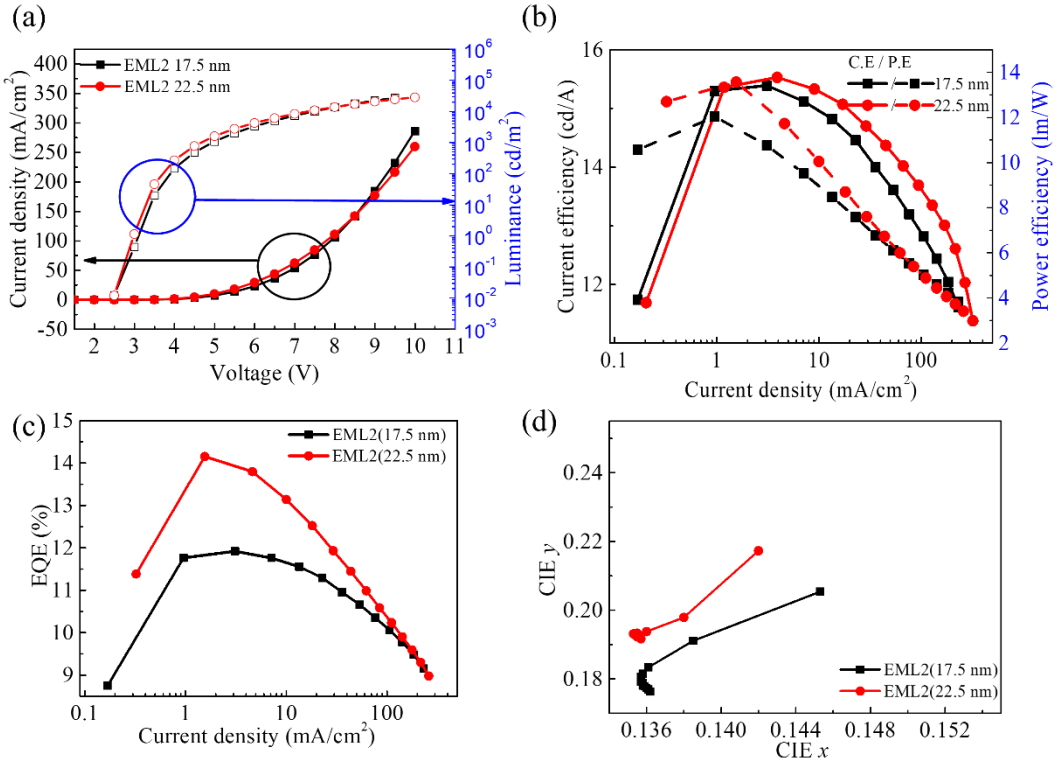

doi:10.6342/NTU202503850

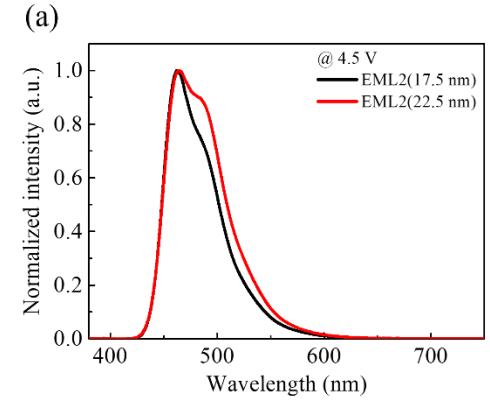

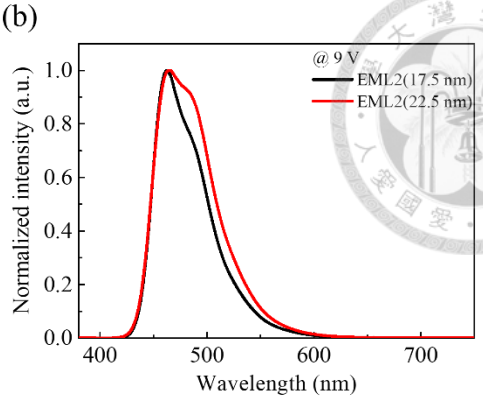

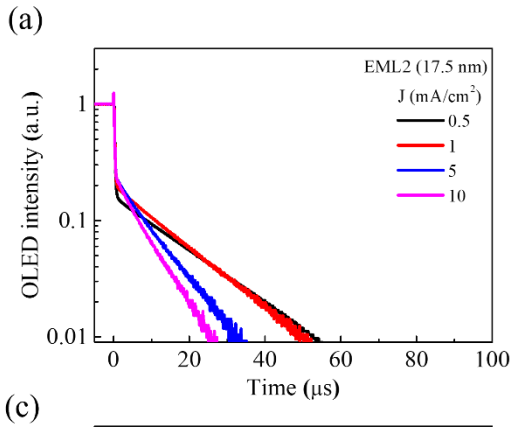

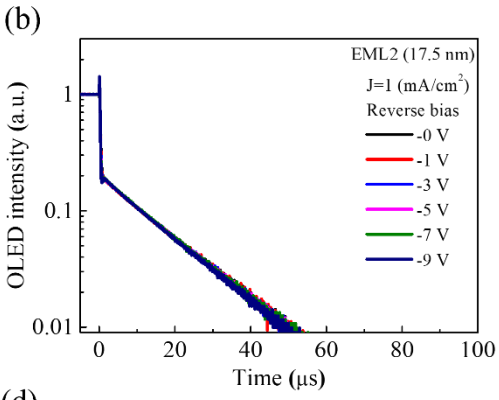

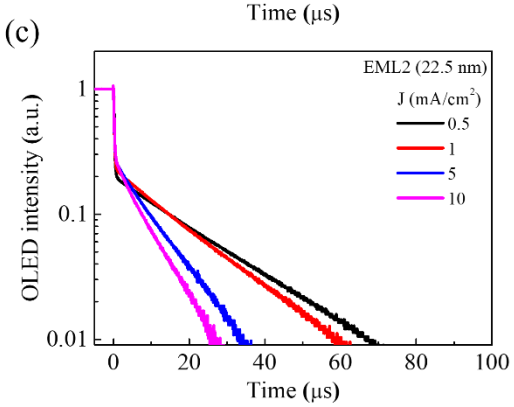

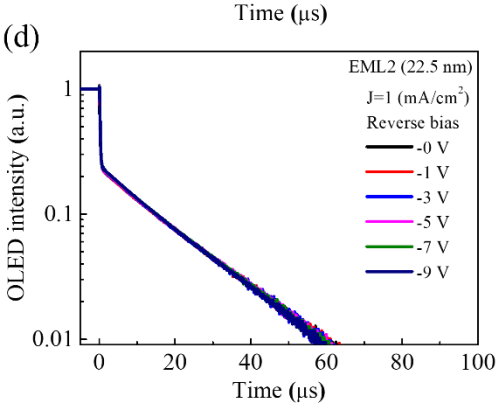

doi:10.6342/NTU202503850

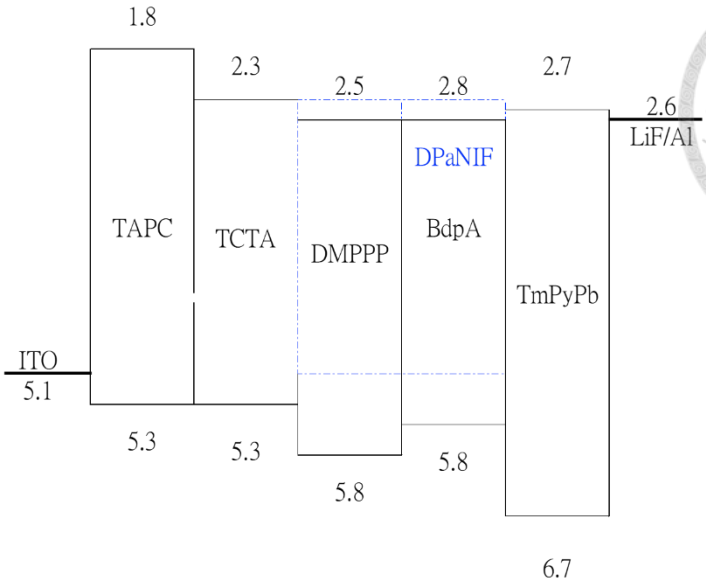

Device	HTL	EBL	EML1	EML2	ETL	EIL/cathode
	TAPC	TCTA	DMPPP: 5%WBD732	BdpA: 3%WBD732	DPPS	LiF/Al
A	40	10	5	25.5	35	1/100
B				22.5		
C			7	20.5		

unit: nm

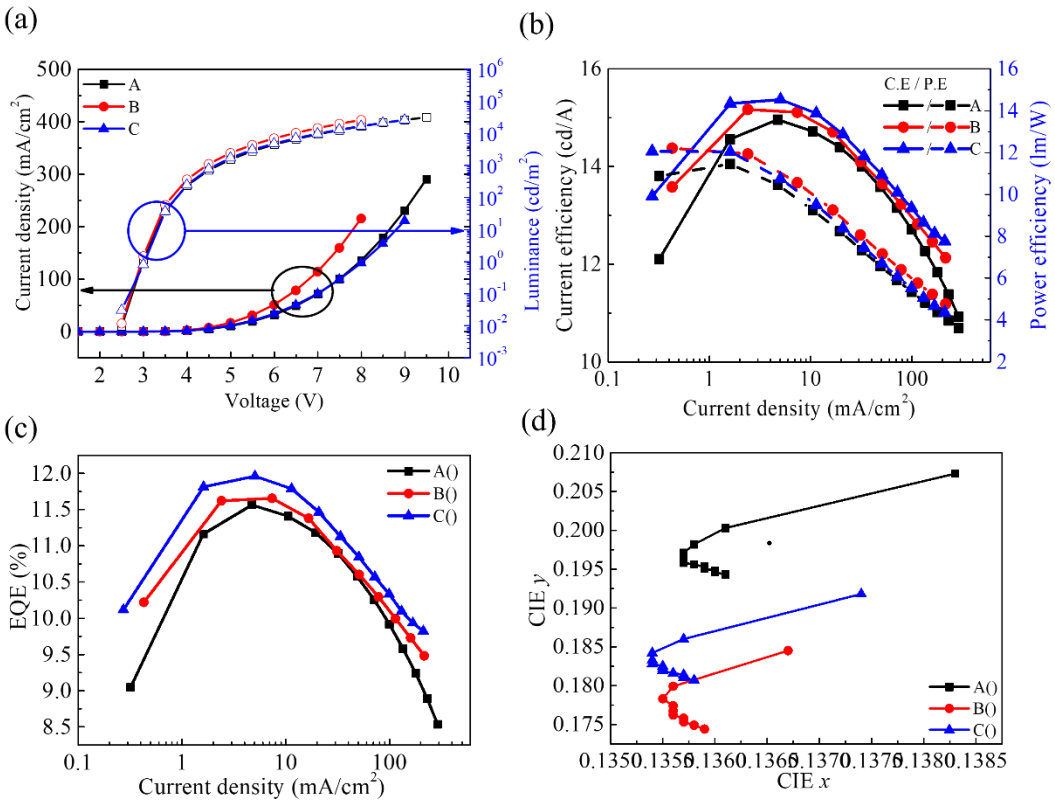

doi:10.6342/NTU202503850

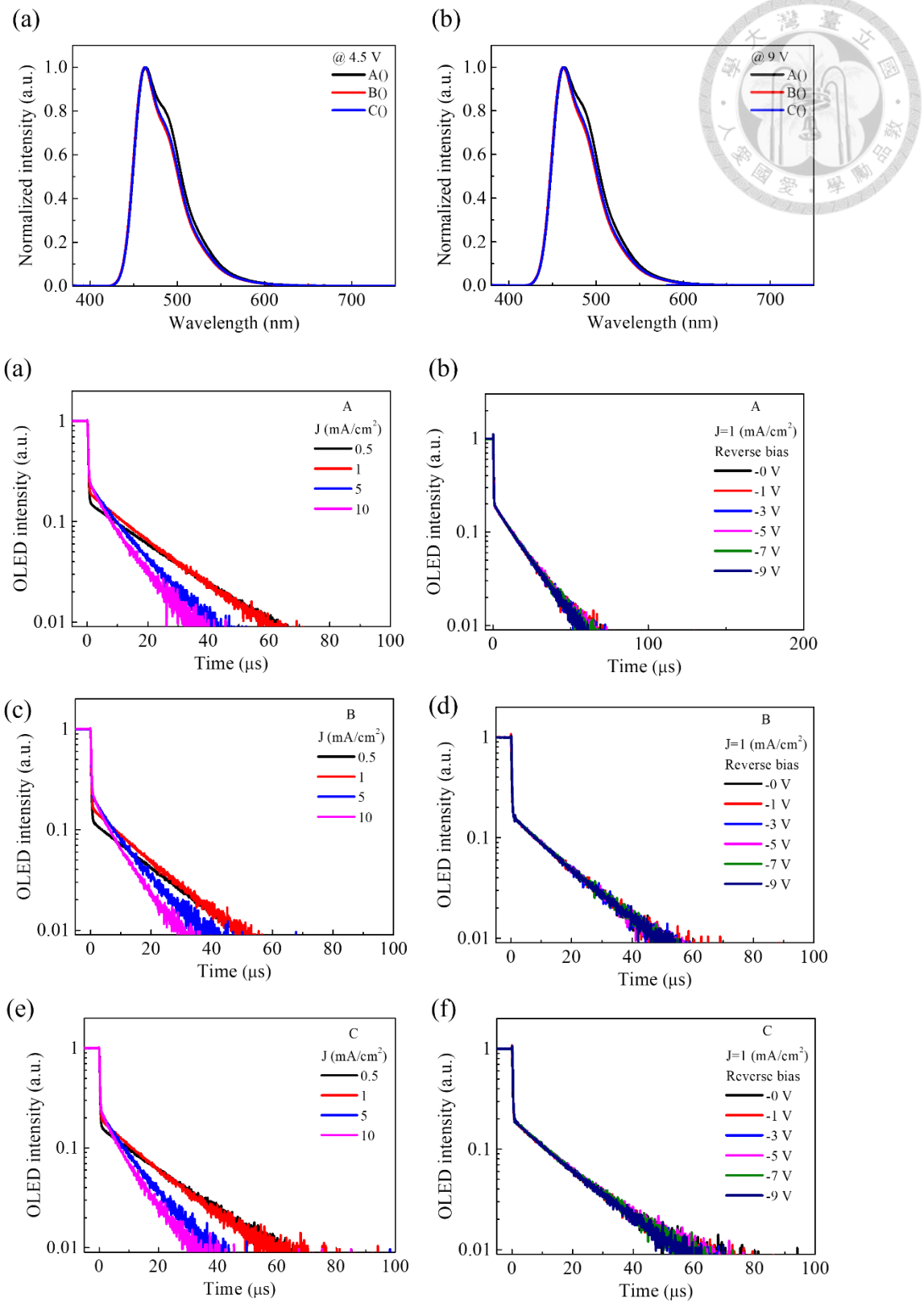

doi:10.6342/NTU202503850

Device	HTL	EBL	EML1	EML2	ETL	EIL/cathode
	TAPC	TCTA	DMPPP: 5%WBD732	BdpA: 3%WBD732	DPPS	LiF/Al
20.5	40	10	7	Device	35	1/100
22.5						
25.5						
27.5						

unit: nm

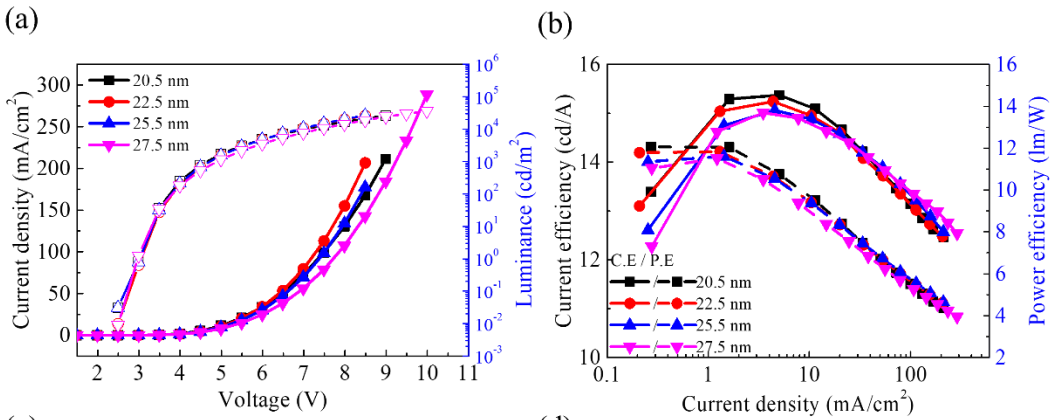

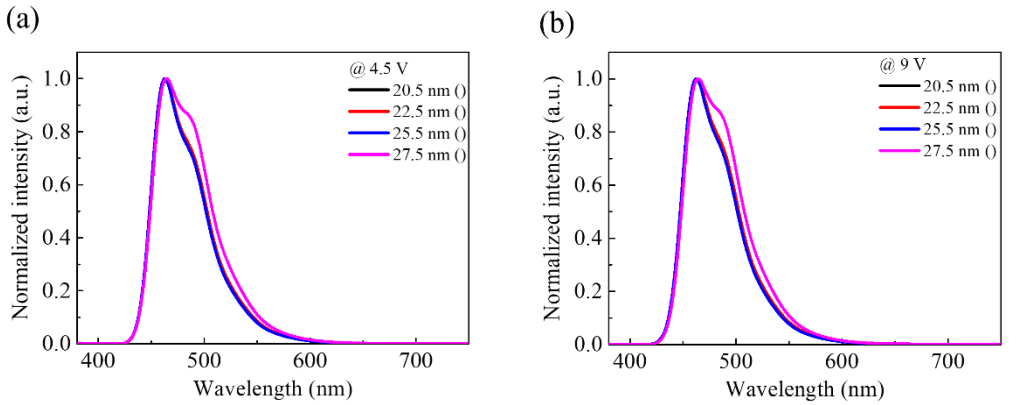

doi:10.6342/NTU202503850

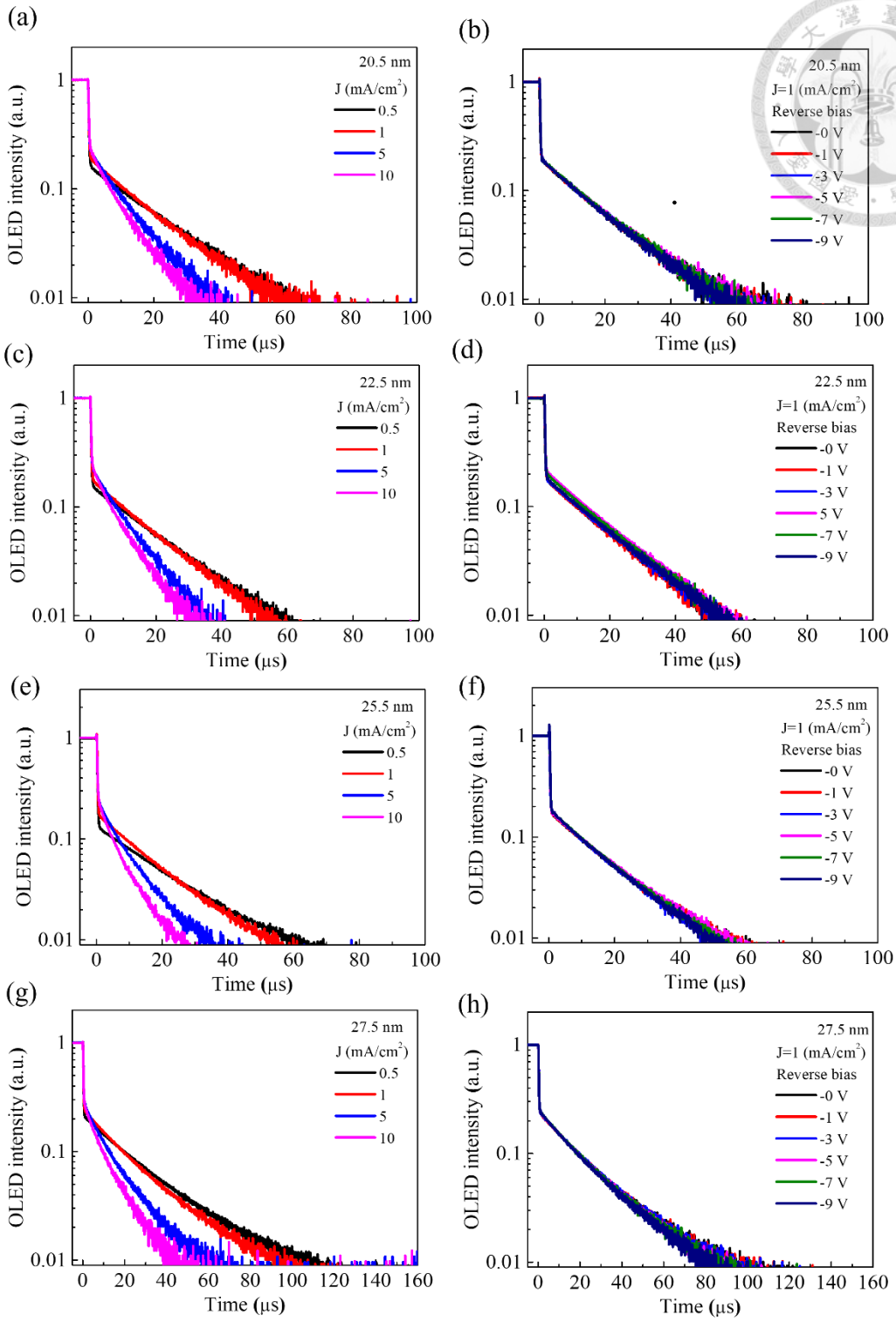

doi:10.6342/NTU202503850